From Powder to Catalyst Body: A Study of the Acidity and Porosity in Zeolite-based Extrudates

Abhijit Randev Wickramasinghe

January 28, 2019

Supervisors:

Nikolaos Nikolopoulos, MSc

Dr. Gareth T. Whiting

Prof. dr. Pieter C. A. Bruijnincx

Utrecht University

Abstract

The use of zeolite powders as heterogeneous catalysts has been studied quite extensively, due to their tunable acidic and shape selective properties in catalysis. However, industrial applications utilise so called "shaped catalyst bodies" such as extrudates, due to their enhanced mechanical stability and ease of manipulation. Traditionally, it was assumed that no interaction occurs between the zeolite and the binder holding the catalyst body together, but recent studies have shown binders can affect the physio-chemical properties of the zeolite and influence catalytic reactions, imparting changes in selectivity. Despite these implications, there is a lack of systematic research, both in academia and industry, in the topic. The first part of this project aims to resolve this knowledge gap and elucidate the origin of these binder effects as well as how they influence catalytic activity. The effect of de-alumination through steaming on the acidic properties of zeolite extrudates was studied using a combination of textural and spectroscopic characterisation techniques. Results showed the zeolite was more resistant to de-alumination in extrudate form compared to the powder, most likely due to the "re-alumination" effect, where Al atoms migrate back into the zeolite framework via extra-porous aluminium species. Catalytic testing in the methanol-to-olefins (MTO) reaction showed that steamed extrudates had the highest selectivity towards propylene and lower formation of coke. The results obtained here can be adapted towards the pre-treatment of upgraded shaped catalyst bodies to tune their behaviour under industrial reactor conditions.

In addition to the acidity, the second part studies the accessibility and interconnectivity (porosity) of zeolite extrudates, where modification of these aspects leads to greater access of acid sites and reactant diffusion. Such aspects are known to affect the activity and product selectivity of various reactions. Inherently hierarchical, further macro-pores were introduced in extrudates through the use of a pore-generating agent (porogen). This method is currently employed for industrial purposes, but

their effect on catalytic aspects has not been studied yet. In order to obtain further insight into these effects, fluorescent microscopy was used in conjunction with traditional bulk techniques to visualise the accessibility of the catalyst body and link it to catalytic performance in the MTO reaction. Fluorescent nano-probes of varying sizes, mimicking reagent molecules, were used to image extrudate inter-connectivity, eventually correlating to the movement of catalytic reaction molecules and the formation of molecular transport boundaries. Results showed that 30 wt% loading of porogen during synthesis of the shaped body, exhibits the highest accessibility of all nano-probes , as well as a higher yield of all MTO products. Despite the formation of large coke molecules at the near-edge region of the catalyst, higher mass transport properties meant larger C_5 olefin products were still able to leave the catalyst. The use of fluorescent probes and microscopy proved to be very useful tool towards better understanding zeolite accessibility and can be adapted for further use, not only in catalysis but any porous material.

Contents

1 Introduction

Currently, coal, natural gas and crude oil make up the majority of the earth's energy sources and also constitute the main feed-stock for the production of various chemicals and materials.[1] An increase in population and energy demands will eventually result in a depletion of the current fossil fuel reserves, meaning suitable alternatives need to be found in order to keep modern society functioning. While energy sources such as solar, wind, hydro-power and other renewable sources have the potential to fulfil our energy demands, the production of valuable chemicals and fuels requires a sustainable carbon source.[2]

In 1977 researchers at Mobil Oil discovered a new route to convert coal, natural gas or bio-mass to useful chemicals, namely; the methanol-to-hydrocarbons (MTH) process.[3] While not producing the world-wide industry as hoped, extensive interest in this reaction has risen from both academic and industrial sources. As with most chemical reactions, the MTH process requires a catalyst to function effectively.

A catalyst increases the rate of reaction through lowering of the activation energy while not being consumed in the process. A catalytic reaction can be considered a cyclic process, where reactants attach themselves to the catalyst surface, react and form products, after which these products desorb from the surface to make room for further reactions. If a catalyst and the reactants are in the same phase it is known as homogeneous catalysis, while heterogeneous catalysis occurs with a solid catalyst, and gas phase reactants. In the case of MTH, the most common catalysts used are zeolite type materials.[4]

1.1 Zeolites

Zeolites are porous crystalline framework materials, composed of tetrahedrally coordinated atoms (Si, Al, etc.) linked by oxygen ions. Zeolite structures are made up of rigid interconnecting tunnels and cages, the building blocks of which are 3, 4, 5 and 6 membered rings. These units are arranged to form larger rings that result in porosity. The pores and channels are mostly uniform, allowing for shape selective properties in catalysis. It can be viewed as a silica framework made from SiO_2 tetrahedra, where some of the silicon atoms are replaced with aluminium and oxygen atoms acting as a bridge between them. Due to differences in charge between Si (+4) and Al (+3) the resulting structure is slightly negatively charged. This charge is compensated by extra framework cations such as H^+ (Figure 1.1b) resulting in OH groups which act as Brønsted acid sites (BAS).[5]

Additionally, structural Lewis acid sites (LAS) can be generated from the dehydration of the zeolite at high temperatures, causing dehydroxylation of the Al(OH)Si groups (Figure 1.1c). Extra-framework Lewis acid sites (Figure 1.1c) can also be created by dislodging Al from the framework (dealumination) using different treatment techniques.[6] Substituting framework atoms with various transition metals (Sn, Ti etc.) can also alter the Lewis acidity.[7] Decreasing the Si/Al ratio, leads to an increased number of framework Brønsted acid sites, due to increased aluminium and hence the number of counter-ions.

Several different zeolites, with varying morphologies and properties exist.[9] The International Zeolite Association (IZA) has developed a structure code (LTA, FAU, MFI etc.) to classify the different framework types while not indicating the chemical composition.[5] One of these zeolites; ZSM-5 (Zeolite Socony Mobil 5), was discovered almost 40 years ago and was soon found to be an excellent material in the conversion of small olefins and alcohols to hydrocarbons, as well as in catalytic cracking applications.[5] The unique MFI framework topology, which consists of a channel system of sinusoidal and straight 10 membered pores running perpendicular to each

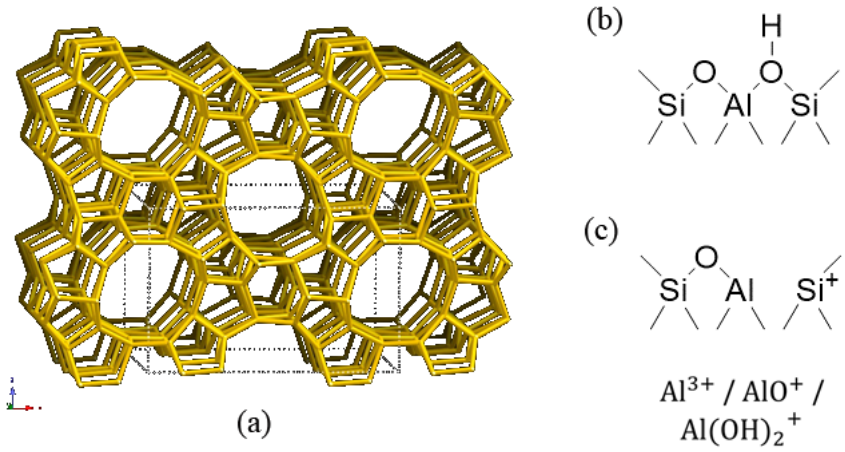

Figure 1.1: (a) MFI framework topology of ZSM-5, made of sinusiodal and straight channel pores running perpendicular to each other. Reproduced from 2017 Structure Commission of the International Zeolite Association,[8] (b) Framework Brønsted acid sites and (c) framework and extra-framework Lewis acid sites in zeolites.

other (Figure 1.1a), gives ZSM-5 excellent shape selective properties.[10] Stability under high temperatures and micro-pores similar to molecular dimensions as well as the ability to vary acid site properties makes zeolites excellent catalysts and are currently utilised in several industrial applications.[11]

1.2 Acidity

As described in the earlier section, framework Brønsted acid sites are proportional to the number of Al atoms in the framework and Lewis acid sites are formed (at the expense of Brønsted sites) through the removal of framework aluminium.[6] While dislodging Al from the framework lowers the BAS density, the next-nearest-neighbour phenomenon means the remaining Brønsted sites are usually more acidic, possibly due to an interaction between extra-framework Al (Al_{EF}) hydro-cations and framework Si(OH)Al groups, although the exact nature of these Al_{EF} species is not known.[6,12] The ability to tune the Si/Al (proportional to SiO_2/Al_2O_3) ratio and thus the nature of the acid sites is what gives zeolites the ability to catalyse a large

range of chemical reactions. Along with the shape selective properties, the acidity of the catalyst has a large influence on the performance of a given chemical reaction. Therefore, a significant amount of research has been carried out towards modifying zeolite acidity to suit the required demands of product selectivity, conversion etc. However, the complexities associated with the scale up of these catalyst materials is often overlooked.[13]

Regardless, zeolites have found major use as catalytic cracking materials in numerous petrochemical processes. Currently, steam cracking of hydrocarbons has been the major source of light olefins and di-olefins for various uses. However, said processes are very energy intensive, with a high amount of CO_2 emissions in addition to having limited control over selectivity. Therefore, catalytic cracking over zeolite catalysts is being pursued as an alternative to overcome these deficiencies.[14] Lu *et al.* investigated the effects of the Si/Al ratio on the performance of ZSM-5 catalysts for light olefin formation through catalytic cracking of iso-butane. Parent ZSM-5 along with metal modified (Fe and Cr) zeolite systems with different SiO_2/Al_2O_3 ratio's (25, 30, 50, 80 and 150) were tested. Characterisation data indicated that the acid site density decreased with increased SiO_2/Al_2O_3 ratio (SAR). They concluded that when the SAR is less than 50, ZSM-5, Fe-ZSM-5 and Cr-ZSM-5 with the same SAR gave similar iso-butane conversions while at SAR above 50, the conversions are different, where Fe-ZSM-5 and Cr-ZSM-5 with high SiO_2/Al_2O_3 ratio's (>50) showed larger yields of light olefins (58%).[15] Similarly, Jung *et al.* explored the effect of altering the Si/Al ratio on the catalytic cracking of n-octane, where the density of acid sites influenced the conversion but not the selectivity. The conversion of n-octane was found to decrease in the 200°-600°C temperature range when utilising increasingly higher Si/Al ratio ZSM-5 (25, 75, 100). However, the selectivity was found to be reliant on reaction temperature, regardless of this ratio.[16]

Mukarakate *et al.* examined the role of varying acidity on the upgrading of biomass pyrolysis vapours over β - zeolites. The SAR was varied from 21-250 and was carried out in a flow micro-reactor and monitoring the changes is product selectivity and deactivation. Results showed that high Silica/Alumina ratio zeolites (75 and 250)

produced a host of oxygenated products such as furans, benzofurans, phenol etc. more readily, while low acid site density zeolites showed a slower rate of diffusion and retained a high degree of activity. Selectivity on the other hand was found to be more-or-less similar across all catalyst samples. They concluded a greater separation between acid sites (low acid site density) leads to greater efficiency in converting pyrolysis vapours.[17]

Aside from tuning Brønsted acidity, Lewis acidic zeolites also have various applications, for example; the isomerisation of sugars. Transition metal containing zeolites are of special interest in this field as inserting isolated Ti or Sn species into high silica content zeolite frameworks creates hydrophobic zeolites, which are ideal for bio-mass transformation processes in water.[7] Moliner *et al.* used Sn modified zeolite Beta for the isomerisation of glucose to fructose, a large scale reaction for the production of high-fructose corn syrup. A 10 wt% glucose solution catalysed by Sn-Beta (1:50 Sn:glucose molar ratio) produced yields of 46% glucose, 31% fructose and 9% mannose. The catalytic activity of Sn modified zeolite beta was found to be superior to ordered meso-porous silica (MCM-41) modified with the same metal centres. Most notably, the isomerisation reaction was possible under highly acidic aqueous environments, opening up the possibility of coupling with other acid catalysed reactions, including hydrolysis/isomerisations (starch to fructose) or isomerisation/dehydration (glucose to 5-hydroxymethylfurfural)[18]

From the above examples it is clear zeolite acidity plays a major role in activity and selectivity of various chemical reactions and therefore the precise tuning of the acid site ratio is of utmost importance. Several post synthesis methods exist for altering the Si/Al ratio through dealumination. Of these methods steaming (hydrothermal treatment) and acid leaching are considered the most feasible techniques in terms of research and industrial applications.[19]

1.3 Hydrothermal Treatment

Hydrothermal treatment or steaming is often used for pre-treatment of zeolite powders in order to alter the Si/Al ratio and impart intra-crystalline meso/macro pores.[19,20] Both of these effects are accomplished through the removal of Al atoms from the framework (dealumination). This process causes a reduction in Brønsted acid sites (BAS) and also results in extra-framework Al species, forming Lewis acid sites (LAS).[6,21,22] Desilication is also a possible route to altering zeolite acidity but is typically carried out through leaching with alkaline solutions.[23] Post synthesis modifications such as steaming are necessary to overcome certain limitations regarding the Si/Al ratio in zeolite synthesis. For example, FAU zeolites cannot be effectively synthesised with a Si/Al ratio higher than 3, therefore if a more silacious version is desired, post-synthesis treatment of the parent zeolite is required.[23]

The extent of dealumination is dependent on temperature, steam pressure and period of hydrothermal treatment.[24] Steaming is typically carried out at ∼723 K under 1 atm pressure for a time period of 1-12 hours or more.[25–28] However, hydrothermal treatment can lead to an non-homogeneous distribution of meso-pores, with harsher steaming conditions exacerbating this effect.[29] Furthermore, excessive amount of extra-framework Al species could result in zeolite pore blocking.[29]

Hydrothermal effects are also observed *in situ* during industrial reaction processes, such as the methanol-to-hydrocarbons (MTH) conversion where the high temperature and pressure along with the presence of water, as a result of methanol dehydration, effectively steam the catalyst[30] This, in turn reduces the Brønsted acidity, resulting in reduced capability to convert methanol.[31,32] Gayubo *et al.* investigated the deterioration of ZSM-5 acidity due to reaction medium water. Their findings indicated that irreversible loss of acidity occurs at 450°C when water is fed into the reactor with methanol at a 1:1 ratio. Severe dealumination was also reported by water produced in the reactor through methanol dehydration (pure methanol), which occurs at 500°C and results in a more pronounced loss of strong acid sites.[24]

The influence of steaming on various zeolites such as ZSM-5, zeolite Y etc. is well documented.[32,33] Ong *et al.* conducted a kinetic study on the steaming of ZSM-5 at different times under hydrothermal treatment, identifying the extra-framework species formed and proposed a reaction scheme for de-alumination based on NMR measurements. They concluded that the process of de-alumination does not follow a random path and certain Al sites are more labile than others.[34]

While using XPS sputter depth profiling to measure the amount of silicon and aluminium on the surface of a two zeolites Aramburo *et al.* came across an interesting result. Applying a mild hydrothermal treatment (500°C) to a ZSM-5 zeolite, the resulting dealumination should have increased the Si/Al ratio. However, surface analysis of the first ∼100 nm showed the surface Si/Al ratio had in fact decreased (more Al in the framework). This effect, where Al migrates back into the zeolite framework known as "re-alumination" was assumed to be the caused by interactions of mobile extra-framework Al species.[35] While these extra-framework groups procure some academic interest, the mechanism of re-alumination is oftentimes mentioned but mostly overlooked.

Aside from altering the acidic properties, dealumination of zeolite frameworks also creates intra-crystalline meso/macro-pores.[19,20] Having covered the acidic properties of zeolites, the porosity of these materials also demands attention as apart from tuning acid sites, the ability to alter the dimensionality of the pores and hence, impart molecular size restrictions on the desired species in a reaction, are what makes zeolites ideal shape selective catalysts.

1.4 Porosity

While zeolites are shown to be excellent at catalysing certain feed stocks, their micro-porous nature means they suffer from a certain degree of diffusion limitation and susceptibility to coke formation, limiting the lifetime of the catalyst.[20,36] This is overcome by introducing different levels of porosity; so called hierarchical zeolites,

which possess at least two levels of pore sizes.[37] In addition to the conventional micro-pores they may also possess meso/macro-pores. To date, the study of meso-porous zeolites is confined to small scale academic research, due to synthesis methods being prohibitively expensive for industrial scale up. Meso/macro-pores in zeolite powders can be introduced through synthesis methods such as hard templating using a carbon matrix (Figure 1.2) as well as post synthesis methods such as steaming and acid/base leaching.[37]

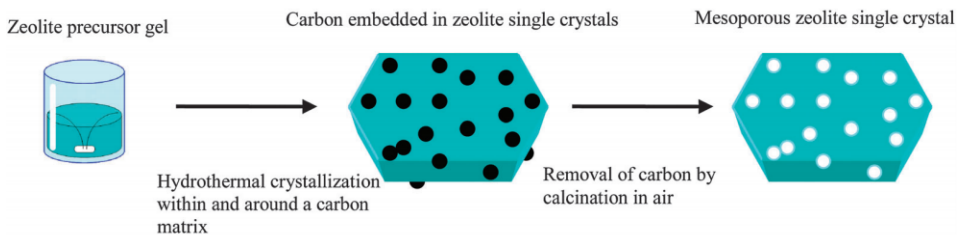

Figure 1.2: Scheme of the synthesis of hierarchical zeolites using carbon matrices as hard templates to induce meso-porosity in zeolite single crystals. Reproduced from Serrano *et al.*[37] An excess of zeolite precursor gel is used so the zeolite crystals encapsulate the carbon particles, which are then removed through calcination leaving behind meso-pores.

Hierarchical zeolites are shown to improve catalytic performance compared to conventional ones due to the lowering of steric hindrance with respect to the acid sites. In most reactions involving zeolite catalysts, the diffusion of the molecule through the pores is the rate determining step, therefore any limitations imposed by slow diffusion through the micro-pores is reduced with the introduction of larger pores.[37,38] In powder zeolites, it is known that mass transfer decreases due to a reduction in crystal size leading to internal defects or surface blockages. Gueudre *et al.* compared the differences in mass transfer effects between conventional zeolite powders versus those extruded with a porous binder material. The hierarchical powder samples showed increased diffusion in the order of 4.6 compared to the conventional powder samples. It was found that mesopores not only shorten the diffusion pathway but also contribute to the overall mass transfer process. The researchers also concluded that the shaping process does not hinder the diffusion in hierarchical materials by blocking the mesopores etc.[39]

Changing crystal size or introducing meso-pores has shown to increase the catalyst lifetime/ resistance to coking, attributed to the larger surface area which helps with the expulsion of coke precursors and the larger area that needs to be covered to block the micro-pores. Catalytic testing to find the effect of mesopore quality was done using methanol-to-hydrocarbons (MTH) and propanal to hydrocarbon conversions. The conventional zeolite samples deactivated much earlier for MTH (24 h on stream) where it was also found that catalyst resistance to deactivation by coking does not depend on an increase in surface area by itself.[36] Other factors such as the number of internal defects in the zeolite crystals did not yield any meaningful correlation with catalyst lifetime, however a critical mesopore volume was found, above which further increase in size no longer helps with the removal of coke.[40]

Additionally, many reactions are determined by chemical factors related to active sites.[37,38] For the catalytic conversion of bio-mass the presence of extra-framework Al species, created during the steaming process, was shown to positively affect the cracking performance, they did however lead to a reduction in access to active sites and increased diffusion limitations. Therefore hierarchical zeolites were utilised as the secondary level of porosity allows for more access to the active sites while also aiding diffusion. Better diffusion of the products out of the crystal results in lower contact time of the products with the surface active sites, lowering the degree to which side reactions occur, as seen in the isomerization of n-alkanes.[2] Serrano *et al.* prepared mesoporous zeolites by varying the concentration of a salinization agent, which was expected to show a different distribution of the hierarchical porosity between micro and meso pores. Catalytic testing using 1,2-epoxyoctane isomerization showed the high significance of accessibility to the active sites. The main products formed in with the parent sample were octanal and octenols, while for the hierarchical samples there was a moderate increase in selectivity towards heavier products.[41]

A similar result was seen in the porosity-acidity interplay in hierarchical ZSM-5 for the production of aromatic enriched bio-oils. In particular ZSM5 with mesopores showed an increase of 25% in the BTX fraction. The main factors in attaining these conversions was the number of Brønsted acid sites in relation to surface area as well

as the access to said acid sites at the mesopore walls and external surface of the zeolite. The hierarchical zeolites induce decarbonylation reactions as opposed to the dehydration reactions that occur over the bulk materials. The increase in the aromatics fraction is accompanied by a decrease in amount of oxygenates.[42]

From the aforementioned examples it is clear that effectively tuning the zeolite porosity is essential for reaction efficiency. However, these so called 'research' catalysts usually only comprise of a single bulk or active phase in powder form.[13] While laboratory studies focus on single crystal or powdered zeolites, industrial applications demand more robust catalysts to function at optimal levels in the reactor.

1.5 Shaped Catalyst Bodies

Zeolites can be applied in several industrial scale processes, such as cracking, isomerisation, hydrocarbon synthesis etc. Unlike laboratory scale research, industrial scale production utilises large fixed bed or fluidised-bed reactor setups where the poor mechanical strength of powder zeolites and harsh reactor conditions can lead to damage or degradation of the catalyst. Therefore, shaped catalyst or 'technical' bodies, in pellet or extrudate form are necessary to overcome limitations related to mass/heat transfer and pressure drop issues as well as being relatively robust and abrasion/fracture resistant during loading/use in the reactor.[43] While not prevalent in academic studies, research into catalyst scale up using extrudates for example, is necessary as the industry continues to grow.[13]

The synthesis of extrudates involves the non-homogeneous dispersion of the zeolite in a binder or matrix which is then shaped to the desired specifications, usually in the form of extrudates, granules or pellets, with clays, aluminas and silicas commonly used as binders.[44] Other additives such as peptising agents (mineral/organic acid) as well as plasticisers (starch, water etc.) are added to the mixture to aid with extrusion and then removed through calcination in the final synthesis stage (Figure 1.3).[13] The binder materials are chosen for their primary goal of enhancing stability;

in principle, having no interaction with the zeolite or influencing the reaction in anyway.

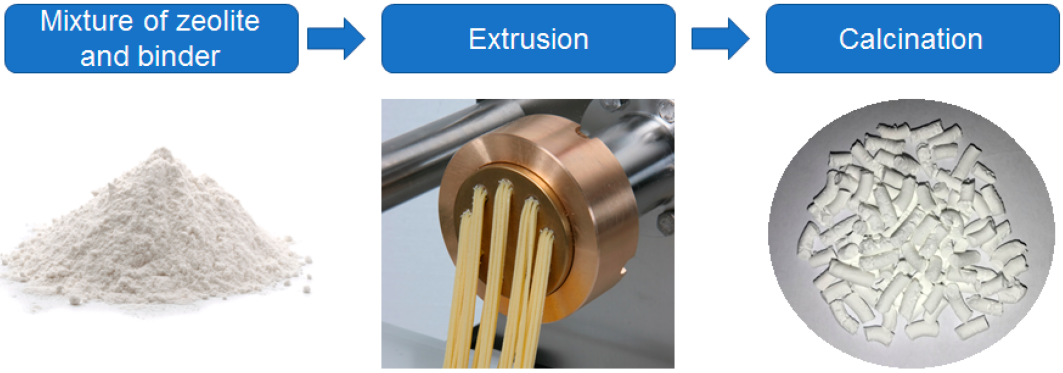

Figure 1.3: Scheme of the extrusion process, reproduced from Bingre *et al.*[43] Additives such as plasticisers, peptisers etc. are also added to the zeolite/binder mixture to aid in the extrusion process. Following the extrusion step, calcination is then used to remove said additives as they are no longer of any use.

The effect of the binder is often overlooked in literature, even though they are shown to exhibit significant impact on catalyst behaviour through physical and chemical means, which can be beneficial or detrimental to catalyst performance.[45] Michels *at al.* investigated the effects of binders on the performance of shaped hierarchical MFI zeolites in the MTH process. Firstly, Hg porosimetry and gravimetric uptake of 2,2-dimethylbutane showed the extrudates exhibited superior macro-porosity and mass transfer properties. Of the various binder matrices used, attapulgite bound extrudates showed superior catalyst lifetime and light olefin selectivity, arising from partial ion exchange from mobile Mg species. In contrast, catalyst performance and selectivity to light olefins was negatively affected through the use of silica or boehmite binders, where the tightly packed structures and reduced Brønsted acidity were found to be responsible for these effects. Looking further into zeolite-binder interactions it was found that reversible Brønsted acid neutralisation by soluble alkaline oxide species present in the clay improved the coke tolerance and light olefin selectivity. Clearly, active sites on the zeolite can be created, or lost as a result of interaction with the binder.[46] Taking these results into consideration, it is reasonable to suggest that the "re-alumination" effect due to steaming discussed

in the hydrothermal treatment section can also occur in extrudates, perhaps to an even greater extent.

Recently, Zhang *et al.* conducted hydrothermal treatment on alumina bound ZSM-5 extrudates and investigated the resulting catalytic activity. While the focus of the paper was firmly on the performance of the catalysts under reaction conditions, the characterisation data showed the change in extrudate Brønsted acidity, to be less than that of the powdered zeolite. Thus, some form of stabilisation in terms of acidity is taking place, most likely the migration of Al atoms back into the zeolite framework.[47] Indeed, as was observed with clay binder bound extrudates, a partial exchange between protons of the zeolite and ions present in the clay is observed when suspended in water during pelletization, neutralizing acid sites in the zeolite.[48,49] Therefore, a pre-steamed zeolite bound in alumina may exhibit Al migration (re-alumination) from the binder back to the zeolite under hydrothermal treatment.

Interest in the "re-alumination" of zeolite bound in alumina can be found as far back as 1985. Chang *et al.* attempted to insert Al into high-silica content zeolite frameworks from an alumina binder through hydrothermal transfer. FTIR measurements showed an increase in the 3610 cm^{-1} band (proportional to Al content in ZSM-5) upon hydrothermal treatment, indicating Al migration from the binder. Al transfer was seen to increase at the expense of the 3742 cm^{-1} corresponding to terminal Si-OH, indicating some form of interaction between the two species, while the mechanism of Al transport itself was deemed to be carried out as aquo-species, such as $Al(H_2O)_6{}^{3+}$. However, literature regarding these interactions has since been very scare, which is unfortunate since research into this area is necessary as these interactions have further implications for large scale use of catalyst bodies.

As seen throughout the porosity and shaped catalyst body sections, hierarchical zeolites, in both powder and extrudate form have shown great promise in terms of catalytic performance. Aside from the meso-porosity (2-50 nm diameter) of the extrudate binder, which helps to overcome issues related to diffusion and deactivation, inter-particle spacing also creates macro-pores (>50 nm diameter) which can be of

similar use. These cavities are created largely by chance and can vary depending on the choice of zeolite/binder used.[46] Therefore, in order to benefit from more uniform interconnected macro-porosity in extrudates an alternative synthesis method is required.

1.5.1 Porogens

Porogen, short for pore generating agent and also known as pore-forming agents, are typically used to induce macro-porosity into various substrates. While literature on the use of porogens for catalyst bodies is rare, they serve a variety of applications such as thermal insulation systems, filtration membranes, bone tissue engineering and pre-form fabrication of ceramics and indeed catalysis.[50] This is mainly due to the pore forming method's relative ease of manufacture, where the porogen agent is included in the synthesis mixture and then expelled using chemical methods or calcination, much like carbon templating discussed in earlier sections (Figure 1.2).[13] Various agents such as polymer beads, starch, glass particles and even liquids are used depending on the desired pore morphology.[51,52] However, excessive weight loadings of porogens could result in a loss of mechanical stability, especially in extrudates.[53]

While not prevelant in academic literature, porogens are known to be used for industrial applications. A patent by Øygarden *et al.* outlines a method for producing supported oxide catalysts in pellet form for N_2O decomposition where a soluble cobalt precursor is added to a slurry of cerium oxide and processing aids in water. Cornstarch (particle size 10 - 15 μm) is used as a pore forming agent and added to the slurry, with the possibility to change the pore size using starches of varying size ranges (rice, potato etc.). They explain that in principle, "any material which is insoluble and thermally decomposes without leaving an inorganic residue may be used" as a porogen.[54] The starch was added after the milling process in order to maintain the grain structure. After the pellets are pressed from the mixture, they were calcined to remove the pore forming agent and then sintered to produce the

finished catalyst body. In order to avoid any deleterious effects to the integrity of the pellet through uncontrolled combustion, the thermal treatment was carried out in 10-20 mbar of O_2 diluted with an inert gas (N_2/Ar).[54] Additionally, Gu *et al.* showed a facile method for the fabrication of porous silicon carbide, through sintering with SiC powder and carbon pellets. This was then used as a host to grow ZSM-5 crystals, and further upgrading with molybdenum, showing increased catalytic activity in the methane de-hydroaromatization reaction.[55]

Prabhakaran *et al.* prepared macro-porous alumina ceramics using wheat particles as a pore forming agent. Wheat starch was added to the aqueous alumina slurry, then calcined to remove the porogen and sintered to produce ceramic. Wheat starch was added between 50-96 wt% yielding alumina bodies with porosity 67-76.7 % and a large distribution of pores between 200-800 μm. While not an application of porogens in catalysis, several aspects related to synthesis and characterisation can be adapted for use in extrudates. A similar synthesis approach can be utilised, with pre-mixing the zeolite + additives and then the addition of the porogen under constant mixing as well as the same temperature programme for the removal of wheat particles. Researchers used SEM to characterise the changes in porosity of the different samples brought on by changing the porogen loading and qualitatively determine the pore sizes present. This type of analysis is not suitable for use with extrudates as more precise methods (physisorption, porosimetry) will be needed to differentiate between the varied levels of porosity. However, SEM can be used to determine what kind of interaction, if any, the porogen has with the zeolite and binder, before and after calcination.

As seen here, porogens are currently being used for a variety of applications, including catalyst bodies for industrial processes. However, understanding the effects brought on by inducing porosity by these means, in terms of catalytic activity has not been attempted in academia. Using a variety of characterisation techniques utilised for research catalysts and adapting methods used in other fields, these effects can hopefully be elucidated. Having discussed how the acidity and porosity of zeolite catalysts can be altered through various methods and explored several

examples of these techniques, the catalyst must ultimately be tested under realistic reactor conditions.

1.6 Methanol-to-hydrocarbons Process (MTH)

This reaction, as the name suggests, is used to convert methanol to useful hydrocarbons, which can then be used in the production of various value added chemicals and fuels. Methanol can be derived from synthesis gas, made from any carbon containing source such as coal, biomass and natural gas.[56] Large scale production of methanol is now possible through the use of direct oxidative conversion of methane, or by the reductive conversion of atmospheric carbon dioxide with hydrogen. Therefore the methanol-to-hydrocarbons process (MTH), used to test the catalytic activity of the zeolites in this case, has attracted a substantial amount of both academic and industrial interest. Various zeolite catalyst materials have been studied for use in the MTH reaction, one of the most promising being ZSM-5.[35] The MTH process has several variations depending on the type of products that are desired, namely the MTG (Methanol-to-gasoline), MTO (Methanol-to-olefins) and MTP (Methanol-to-propylene). Varying product selectivity is achieved through carefully altering the reaction conditions and type of catalyst.

Alternative feedstocks such as methanol coupled with chemical processes such as the MTO reaction allows for the production of light olefins (ethylene and propylene) without the need of fossil fuel precursors. Lighter olefins such as ethylene and propylene are of great importance for both the petrochemical industry and well as society in general due to their ease of transport and as building blocks for polymers.[57]

Light olefins are currently extracted through the steam cracking of natural gas liquids (NGL), naphtha or other fractions obtained from crude oil. By comparison MTO is able to provide a wider and more flexible range of ethylene and propylene ratios.[56] In addition to the depletion of crude oil, environmental factors such as the contribution to the greenhouse effect means that it is imperative an alternative source for light

olefins is found. Therefore, utilising the syngas to methanol route coupled with the MTO process, an alternative 'green' source for the production of light olefins is possible, as long as the feed-stock is naturally produced.

1.6.1 Mechanism

The MTH process works by producing hydrocarbons from methanol over acidic zeolite catalysts at temperatures above 300°C.[58] The exact catalytic mechanism of the process however, has been under debate for several years. Initially, direct mechanisms were proposed, but these were later disproved due to the large activation energies associated in the formation of C-C bonds.[59]

The most widely accepted mechanism for the MTH process is the hydrocarbon pool (HP) mechanism, where the active sites for the production of hydrocarbons is a mix of Brønsted acid sites and a pool of various hydrocarbon species, which exist in either a neutral or charged state.[60] The hydrocarbon pool is formed in the initial stage of the MTO process, building up from reactions between methanol, DME and other reactants. The retained hydrocarbon species are alkylated by the methanol feed and the resulting de-alkylation of these species produces olefins. The size and shape of the zeolite pores dictate the exact nature of the hydrocarbon pool, therefore medium pore MFI zeolites undergo a different reaction mechanism compared to small pore frameworks such as CHA.[57]

More recently a dual cycle mechanism was proposed for the hydrocarbon pool as it was found that the formation of different reaction products was mechanistically separated.[61] As seen in Figure 1.4, alkene intermediates which are alkylated by methanol and then de-alkylated, mainly yield propylene as well as larger alkenes, while the aromatic cycle intermediates which are alkylated by methanol yield ethylene in addition to smaller aromatics.[57,62] Product selectivity is influenced by promoting one of the two cycles over the other. For example, to increase selectivity towards propylene and similar lower olefins the alkene cycle should be promoted.

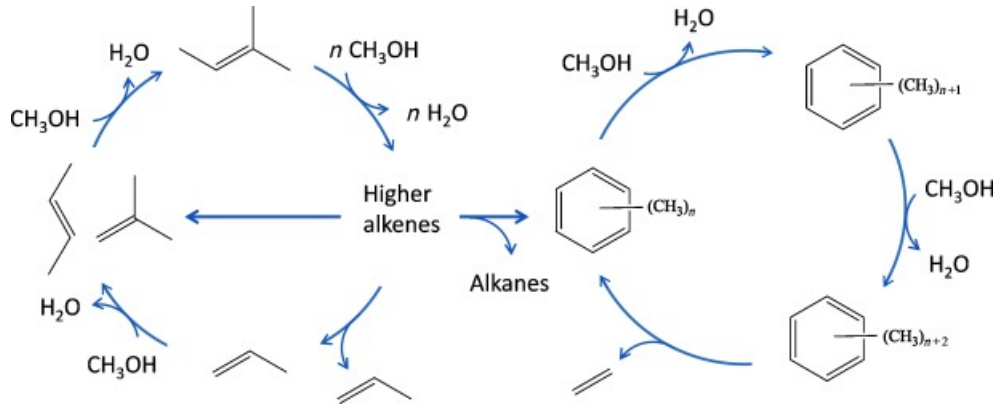

Figure 1.4: Proposed dual cycle mechanism of the hydrocarbon pool for MTH over ZSM-5 catalysts. Reproduced from Olsbye et al.[57] The hydrocarbon pool is formed in the initial stage of the MTO process, building up from reactions between methanol, DME and other reactants. The alkene cycle (left) produces mainly propylene and larger alkenes while the aromatic cycle (right) produces not only aromatics, but ethylene as well.

1.6.2 Product Selectivity

As demands for different olefins is constantly changing, varying the product selectivity is advantageous for industrial scale production. Porosity of the catalysts, which have size dimensions in the range of small hydrocarbons can be used to tune which products are formed inside the catalyst and exit the pores. When ZSM-5 is used for the MTH process the ten ring pores of the MFI structure produces a mixture of olefins, small aromatics and paraffins.[58] Product selectivity can also be controlled through changing the acidity or reaction conditions. Olefin selectivity can be increased by using low methanol pressures and high reaction temperatures. Varying the Si/Al ratio of zeolites, thus changing the acid strength/density can influence the lifetime and selectivity of the catalyst. Additionally, modification through the introduction of alkaline metals into the zeolite framework has a similar effect.

Goetze *et al.* studied the effect of varying ZSM-5 acidity through Mg modification on the selectivity and catalyst lifetime in the MTO reaction. NH_3-TPD and CO indicated that modified Mg-ZSM-5 had a larger density of weak acid sites compared to the parent ZSM-5, where stronger Brønsted acid sites were measured, albeit in

lower concentrations. Mg treatment was shown to increase catalyst lifetime from 16.2 h (parent) to 54.7 h (modified) as well as increase selectivity towards propylene (37 %), C_4/C_5 olefins (20%/8%) while lowering selectivity towards ethylene (6%) and paraffins (5%). Clearly, reduction of the strong Brønsted acid sites through Mg modification has an influence on the MTO mechanism, with the alkene cycle being prioritsed over the aromatic cycle.[58]

As determined by Mitchell *et al.* the introduction of mesopores has also been shown to improve the catalytic activity in MTO. The catalytic cycle of the MTO process follows the relative selectivity to light olefins trend: propylene > butylene > ethylene. The hierarchical zeolites exhibit a near constant selectivity profile during the whole cycle and exhibits a higher average selectivity to C2-C4 olefins (52%) compared to the conventional (48%). Additionally the selectivity to propylene, one of the most desired olefins is higher in the hierarchical zeolite.[63] Zhang *et al.* further investigated the porosity-acidity interplay through steaming of ZSM-5 catalyst bodies with alumina as a binder. Hydrothermal treatment at 773K for 12h was found to be ideal for increasing selectivity towards propylene (43%) and longer catalyst lifetime (89h, WHSV = $6h^{-1}$)[47] ZSM-5 is ideal for the MTO reaction as acid sites can be distributed in the straight and sinusoidal channels as well as the channel intersections due to the MFI topology. Therefore, altering the siting of framework Al should lead to enhancement of catalytic properties, provided the effects of these sites are understood.[64]

1.7 Aims

The focus of the first chapter, utilising zeolite powders and alumina binder bound extrudates, is to analyse the resulting physical/chemical changes that occur due to hydrothermal treatment and correlate it to the results seen in the MTO process. The aim is to determine if the zeolite in shaped catalyst form is more resistant to acidity loss upon steaming and if so, elucidate the origin of this increase in stability. Since it has been established that methanol dehydration steams the catalyst in the reactor, hydrothermal treatment of these materials can be used to mimic conditions in said reactor and shed light on the physio-chemical changes that occur to these catalysts. Firstly, the hydrothermal treatment of zeolite powders, under mild steaming conditions and subsequent characterisation of their physical (Physisorption) and chemical (CO/pyridine FTIR, NH_3-TPD) properties will serve as a point of reference for further study of shaped catalyst bodies utilising these same conditions/characterisation techniques. Emphasis is placed on this comparison, as to the best of our knowledge, no study of this nature has yet been attempted in academia. Taking binder effects into consideration acidity measurements should indicate the zeolite acidity is stabilised in the extrudate form. Possible mechanisms include the shielding of the zeolite framework by alumina binder particles and/or the migration of Al atoms back into the framework (re-alumination), making the zeolite more resistant to hydrothermal conditions. Due to this acid site robustness it is likely the hydrothermally treated extrudate will show a higher degree of catalytic activity compared to the steamed powder in the subsequent catalytic testing with the MTO process.

The second chapter will centre around inducing further macro-porosity in extrudates, with the intention of improving inter-connectivity through the use of a porogen. These type of porogen-based extrudates are currently used for industrial purposes, however the effects of this technique on the catalytic activity has not been investigated. Therefore, this study aims to fill in knowledge gap in order to better understand how these industrial catalysts function under realistic reactor conditions.

Firstly, interaction of the porogen with various components of the extrudate will be examined using a variety of charaterisation techniques, with emphasis on the use of fluorescent probes coupled with Confocal Fluorescence Microscopy (CFM) as a facile technique to visually study the accessibility of the catalysts. These results will then be correlated to the catalytic data and movement of catalytic reaction molecules in the MTO process to provide a proof of principle into the effects of how porogens influence the physio-chemical catalytic properties of extrudates. Prior literature on meso-porous zeolites indicate that higher accessibility to the active sites will be observed, possibly resulting in a higher yield of products. However, varying the porosity to such an extent could result in other physical and chemical changes, where selectivity in the MTO reaction could possibly shift towards undesired aromatic products.

2 Methodology

2.1 Catalyst Preparation

2.1.1 Powder Zeolite

Powder ZSM-5 samples were provided by ACS Material (MR 38 and MR 117), correspoding to a silica/alumina ratio of 38 and 117 respectively. These were steamed in a quartz tubular oven at 500° C for 7h under nitrogen flow (100 ml/min) with a bubbler to produce steam at a temperature of 140° C. The standard materials were heat treated under the same conditions without steam for a proper comparison.

2.1.2 Shaped Catalyst Bodies

Powder ZSM-5 was mixed with either CATAPAL D, PURAL TM70 or TH100 alumina binder (SASOL), methyl cellulose (Sigma Aldrich, 4000 CP) and the required amount of acetic acid dissolved in Milli-Q water. A torque rheometer (Caleva) was used to measure the optimum viscosity for extrusion. The paste (total weight 20 g), which contained a 50:50 wt% (zeolite : binder) ratio was extruded using a Mini-screw extruder (Caleva) with a 2 mm cylindrical die plate. The freshly made extrudates were left to dry overnight and then calcined in a tubular oven at 600°C (10°C/min) for 6 h under air flow (150 ml/min). The method used for porogen synthesis in this project was adapted from that used by Prabakharan *et al.* for the preparation of macro-porous alumina ceramics using wheat particles as pore forming agents.[51]

They were made by adding wheat (10/30 wt%) or rice starch (10/30 wt%) to the initial mixture and extruding through the same process as the zeolite extrudates. Based on TGA measurements (Appendix Figure 1), the porogens were heat treated at 300°C (2.5°C/min) for 6 h and then at 600°C (2.5°C/min) for 6-12 h under O_2 flow (120 ml/min) to completely remove the carbon template.

2.2 Characterisation

2.2.1 Physisorption

Dimensional properties of the zeolites and extrudates were measured through physisorption on a Micrometrics TriStar 3000 V6.08 surface area and porosity analyser. Brunauer-Emmett-Teller (BET) analysis was carried out for the pressure range 0.05 $\leq p/p_0 \leq$ 0.25 to obtain the BET surface area, while micro/meso porosity was derived using a t-plot analysis based on the Harkins-Jura reference isotherm:

$$t = \sqrt{\frac{13.99}{0.034 - log\frac{p}{p_0}}} \tag{2.1}$$

which is based on general oxide support molecules and can therefore be used in this instance. Barrett-Joyner-Halenda (BJH) analysis was used to determine the pore size and cumulative pore volume. The pore size distribution was derived from the adsorption branch of the isotherms. In order to negate any vapour liquid interactions taking place due to capillary condensation, Ar was used instead of Nitrogen. Measurements were performed at 77 K.

2.2.2 X-ray Diffraction

The crystal structure of the zeolite samples were probed using X-ray diffraction (XRD). The constructive scattering of the incoming X-ray beams on the surface

and their subsequent reflections obey Bragg's law:

$$2dsin\theta = n\lambda \tag{2.2}$$

where d is the inter-planar distance, θ the angle of incidence, n an integer, and λ is the wavelength of the x-ray beam in Å. A Bruker D2, with a cobalt Kα X-ray tube (λ = 1.7902 Angstroms) was used to perform all measurements. All XRD patterns were measured at room temperature in the range $5^o > 2\sigma > 80^o$ with an increment of $0.02^o/s$. The crystal phases were determined using the PDF 2015 database.

2.2.3 NH_3-TPD

The acidity of the zeolites and related materials were measured using temperature programmed desorption (TPD) with ammonia as the probe molecule. Measurements were carried out on a Micrometics Autochem 2910 apparatus equipped with a thermal TCD detector, using 100 mg of sample, placed in a quartz tube reactor. The sample was dried at 600°C for 15 mins with a temperature ramp of 10°C/min. Ammonia (10 vol % in He) was adsorbed for 45 minutes at 373 K using pulses.

2.2.4 Mass Spectrometry coupled Thermogravimetric Analysis

In order to determine the proper calcination procedure for removing the carbon template, mass spectrometry-coupled thermo-gravimetric analysis (TGA-MS) was performed, using a PerkinElmer TGA 8000 apparatus, with a Hidden Analytical HPR-20 Mass spectrometer. Prior to the temperature increase, the apparatus was flushed with Ar with a flow of 14 mL/min for 10 minutes at 30°C afterwhich the gas was switched to O_2 (20% in Ar) . Sample weight was $\sim$ 5 mg while the method was programmed to hold at 30°C for 10 minutes, then heat to 700°C with a ramp of 2.5°C/min.

2.2.5 Pyridine FTIR

Temperature programmed desorption of pyridine, monitored by Fourier Transform Infra-red (FTIR) spectroscopy was used to determine the nature and concentration of the acid sites. The IR spectra were recorded on a Thermo IS5 spectrometer with each spectrum consisting of 32 scans recorded with a resolution of 4.0 cm^{-1}. Pellets with diameter 1.2 cm and approximately 20 mg of sample were made by crushing the sample and then pressurizing it under 5 tons for 30 seconds. The samples were dried under ultra-high vacuum ($10^{-4} - 10^{-5}$ mbar) at 550°C for 60 minutes. Pyridine was desorbed at a temperature range of 50-550°C (ramp of 10°C/min) with a measurement taken every 50°C. It was then left at the final temperature for a further 60 minutes to ensure complete desorption of pyridine.

Concentrations of acid sites were determined using the following equations:

$$[BAS] = IMEC(B) \times IA \times \frac{\pi R^2}{W} \tag{2.3}$$

$$[LAS] = IMEC(L) \times IA \times \frac{\pi R^2}{W} \tag{2.4}$$

where IMEC(B,L) is the integrated molar extinction coefficients (cm/μmol), IA(B,L) the integrated absorbances (cm^{-1}), R the radius of the catalyst pellet (cm) and W is the weight of the pellet (mg).[65] Spectra were corrected to the weight of the wafer and integration of the peaks was performed in Origin2017.

2.2.6 CO FTIR

Self-supporting pellets were made using ∼20 mg of catalyst. The pellets were first calcined at 550°C with a ramp of 10°C/min for 60 minutes under vacuum (10^{-4}–10^{-5} mbar) After cooling to room temperature, the samples were cooled even further through circulating liquid nitrogen through the cell. When the temperature was

stable at -189°C, CO (10% in He) was added and left to equilibrate at different pressures. Spectra were recorded between 10^{-2} - 1 mbar. For the extrudates; the lower concentration of zeolite meant the standard method was unable to detect any acid sites. Therefore the cell was 'flooded' with CO (250 mbar), cooled with liquid nitrogen to -189°C and then desorbed by decreasing the pressure. Deconvolution of the peaks was performed using the Voigt function on plotting software Fityk.

2.2.7 UV-Vis Spectroscopy/ Micro-spectroscopy

The physiochemical changes in the samples were studied using in-situ UV-Vis spectroscopy, using thiophene as a probe molecule. Measurements were performed using an in-situ cell (FTIR600, Linkam Scientific Instruments) equipped with a temperature controller (Linkam TMS 93). 30 mg of zeolite powder was compressed into a pellet using the same method as pyridine/CO IR and placed on the linkam cell with the UV lamp, connected to a spectrometer (AvaSpec-2048TEC, Avantes) directly above. 20 μL of thiophene dropped onto the surface upon which the temperature ramp was started, heating the sample to 130°C at 30°C/min. Spectra were recorded every 10s with an integration time of 14.5 ms. This procedure was replicated for catalyst bodies, using the same mass of extrudates instead of pellets.

UV-Vis micro-spectroscopy was used to measure specific points on the spent MTO samples. A CRAIC 20/30 PVTM micro-spectrometer equipped with a 74 $\times$ 0.65 NA lens was used in reflectance mode. The surface of the sample was illuminated with a 30 W halogen lamp and spectra were recorded in the 250-900 nm range, at different locations on the extrudate cross-section surface.

2.2.8 Focused Ion Beam/Energy Dispersive X-ray Scanning Electron Microscopy

Scanning electron microscopy (SEM) allows the investigation of the surface morphology with very high resolutions (<10 nm). FIB-SEM was conducted on a FEI Helios Nanolab 600 Dualbeam microscope. Extrudate samples were first attached to an aluminium stub with carbon tape and then coated with 4.5 nm of Pt using a Cressington 208HR sputter coater, to increase conductivity. Before the milling procedure, a 3 µm thick layer of Pt was deposited near the desired cutting location using a Gas Injection System (GIS), the purpose of which is to protect the desired area from the ion beam and improve the milling quality.

A trench was milled into the cross-section of each extrudate using a 30 kV Ga beam with a current of 47 nA and was followed by a cleaning step. Imaging was done at various magnifications with a dwell time of 10.00 µs and electron beam at 2.00kV/0.10 nA. Energy-dispersive X-ray (EDX) spectroscopy was performed using an Oxford instruments silicon drift detector X-max energy dispersive spectroscope with an electron beam at 5.00 kV and a current of 0.10 nA.

2.2.9 Mercury Porosimetry

Hg porosimetry in-/extrusion measurements were carried out externally using an AutoPore IV 9500 V1.09 (Micromeritics) instrument. The extrudates were degassed in N_2 flow at 353 K overnight. Surface tension (γ) and contact angle (θ) were set to 485 dyn·cm^{-1} and 140°, respectively, with the materials infiltrated up to P_{max} = 60 000 psi to probe pores of a minimal diameter ø= 4 nm.[66] The samples were subjected to one intrusion-extrusion cycle, and the Washburn law;

$$P = -\frac{4\gamma cos\theta}{d} \tag{2.5}$$

was applied in the pressure range probed. Where P is the pressure, γ is the surface tension of the liquid, θ the contact angle of the liquid and d is the diameter of the capillary.[67]

2.2.10 Confocal Fluorescence Microscopy

Confocal Fluorescence Microscopy (CFM) provides us with true three-dimensional (3D) optical resolution. This is accomplished through the suppression of any signal originating from an out-of-focus plane through the use of a pinhole in front of the detector. Light coming in from an in-focus plane is let through the pinhole while out-of-focus light is mostly blocked. A laser, used to excite the sample, passes through a pinhole, is then reflected by a dichroic mirror and focused by the microscope objective on a small area of the sample (Figure 2.1). The dichroic mirror works by reflecting light shorter than a certain wavelength while transmitting light of a longer wavelength, allowing us to observe only the emitted light, which is focused into the pinhole and finally measured by the photomultiplier tube. Rejection of out-of-focus fluoresecent light means that CFM produces very accurate 3D images of a sample with better horizontal/vertical resolution.[68]

Fluorescent imaging of the extrudates was done using a confocal fluorescence Nikon Eclipse 90i microscope with a pin-hole to filter out-of-focus light and dichroic mirrors, corresponding to the relevant laser wavelength. The microscope was equipped with a Nikon A1 scan head, accomodating the optics, which couple fibre optics for excitation and emission light with the microscope. A Nikon 10 X/0.30 objective was used along with a spectral analyser in the Nikon A1 system, equipped with 32 photomultiplier tubes (PMT's), set to collect emission light in the region 509-749 nm (resolution 6 nm).[66]

Fluorescent and photostable dyes of differing sizes were used as probe molecules. The 5 nm probe molecule, N,N'-Bis(1-hexylheptyl)-perylene-3,4:9,10-bis-(dicarboximide) (PDI, Sigma Aldrich) has an absorption maximum at 525 nm and was supplied di-

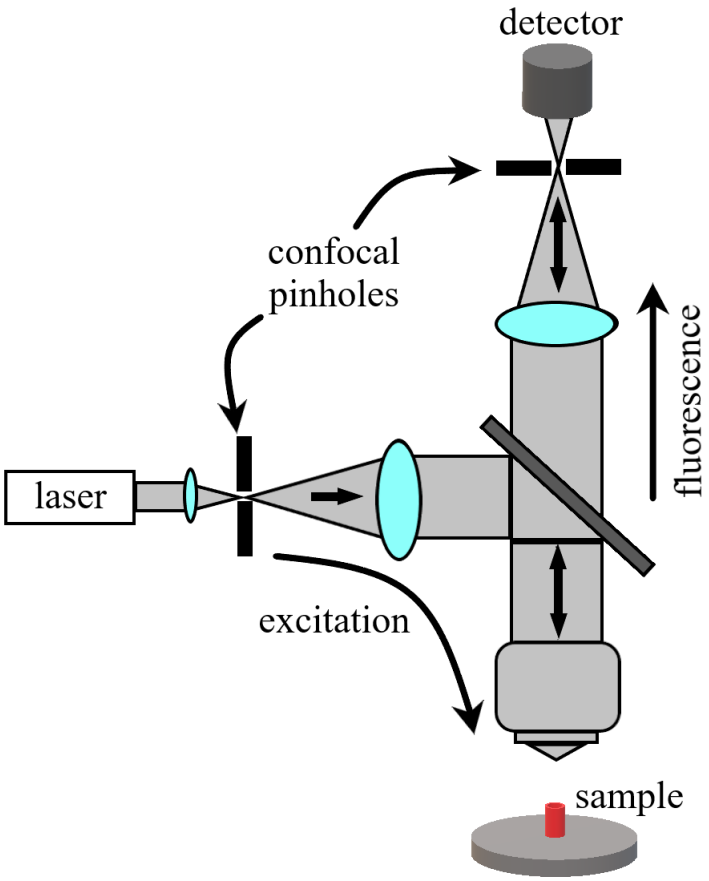

Figure 2.1: Confocal Fluorescence Microscope. Reproduced from Mueller *et al.*[68] Light coming in from an in-focus plane is let through the pinhole while out-of-focus light is mostly blocked. A laser, used to excite the sample passes through a pinhole, is then reflected by a dichroic mirror and focused by the microscope objective on a small area of the sample.

luted in toluene, while the larger probes of 20/100 nm (FluoSpheres^{tm}, Carboxylate-Modified Microspheres, ThermoFisher Scientific) were supplied diluted in MilliQ water. Impregnation with the probes was carried out on single catalyst bodies for different incubation times, left to dry at room temperature, cut width wise and imaged with a 488 nm laser. Penetration depth of the probe was measured manually using the 3D volume scale bar and were taken for 4 different regions of the extrudate cross-section, creating an average penetration depth. Imaging of the spent MTO extrudates was done using the same procedure using both 488 and 642 nm lasers simultaneously, with dichroic mirrors at 488, 561 and 642 nm. The raw fluorescent images were then converted to green (509-637 nm) or red (641-749) grouped

spectra to better visualise the boundaries between fluorescent regions.[66]

2.3 Methanol-to-olefins Reaction

Measurements were performed in a fixed bed reactor with 66 mg of sieved catalyst (212 - 425 μm fraction) used in each measurement. Before the measurement step the catalyst was heat treated at 400°C under 100% oxygen flow (10 mL/min) for 30 minutes and then cooled to reaction temperature under helium flow (40 ml/min) to purge the line of oxygen. Helium was used as a carrier gas and flown through a methanol saturator kept at 21-22°C with a weight hourly space velocity (WHSV) of 8 $gg^{-1}h^{-1}$. Helium coupled with methanol is flowed through a reactor bypass to determine when the level of methanol is stable and thus time to start the measurements. Reaction was carried out at a temperature of 350°C while the analysis of the reactants and resulting products was carried out using an Interscience Compact GC equiped with Rtx-1+Rtx-Wax, Rtx-TCEP+Rtx-1 and Al_2O_3/Na_2SO_4 columns with two flame ionization detectors (FID's). Products were identified according to retention times using reference standards. Methanol conversion was calculated using the equation:

$$Conversion(\%) = \frac{[MeOH_{in}] - [MeOH_{out}]}{[MeOH_{in}]} \tag{2.6}$$

while hydrocarbon (C_nH_m) yields calculated from:

$$Yield(\%) = \frac{n[C_nH_m]}{[MeOH_{in}]} \tag{2.7}$$

UV-Vis spectroscopy was used to determine the formation of active species in the hydrocarbon pool and related coke compounds. Measurements were performed in the range of 250 - 1000 nm using a high temperature UV-Vis probe provided by Avantes. The probe consists of an excitation and collection optical fibre, diameter 400 μm and

length 1.5 m, within a strainless steel protective sleeve. A deuterium-halogen lamp was used as a light source, coupled to an AvaSpec 2048 UV-Vis spectrometer.[69] The spectra were saved every 10 seconds, with 375 accumulations and 25 ms integration time.

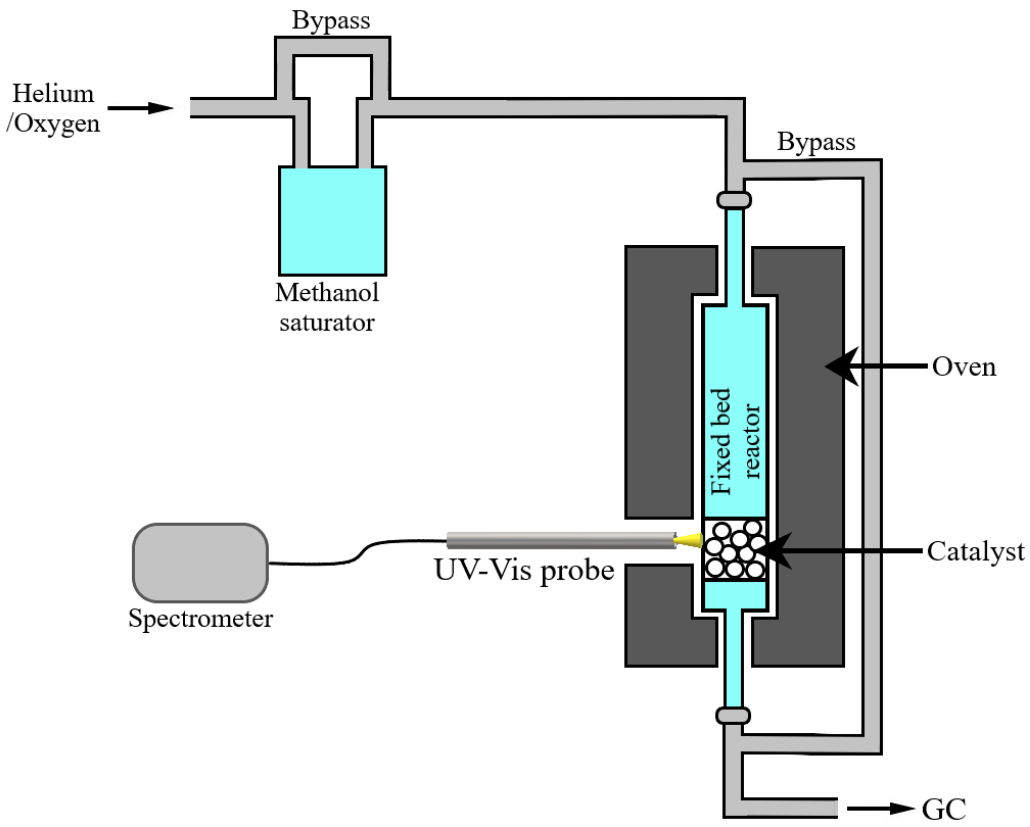

Figure 2.2: Methanol-to-Olefins reactor setup. Methanol is flowed into the reactor using helium, with the distribution of products being monitored by an online-GC, while *Operando* UV-Vis spectroscopy was used to monitor coke formation in the catalyst.

3 Hydro-thermal Treatment of Zeolite Powders/Extrudates and its Effect on Catalytic Activity

This chapter will focus on the effect of hydro-thermal treatment on the acidic properties of zeolite powders and zeolite/binder bound extrudates. As mentioned in the introduction, hydro-thermal treatment causes de-alumination of the zeolite framework, which results in a loss of Brønsted acidity, amongst other effects. The zeolite powder samples utilized were chosen for their differing silica/alumina ratio (ZSM5-117/38), the purpose of which is to observe whether the amount of silica/alumina plays a role in acidity loss when steamed. The changes seen in the powder zeolites were then compared to extrudate samples, comprised of ZSM-5 38 and an alumina binder. However, physical properties of the binder; particle size, surface area etc. can also influence the characterisation/catalytic activity. Therefore a host of different binders (CATAPAL D, TM70 and TH100), where the "M"and "H" correspond to medium and high degree of porosity respectively, will be used. These have varying physical properties (Appendix Table 1), which will allow us to postulate what properties, if any, aside from acidity are influencing the characterisation and catalytic results.

The comparison with the high silica and alumina content zeolties is to observe the effect of Al concentration on acidity loss. While the main focus of this chapter is the comparison of zeolite powder and extrudates in terms of hydro-thermal stability. In particular, the effect of a binder in either preserving or re-forming Brønsted acid

sites in the zeolite that would otherwise be lost upon steam treatment. Mechanistically, the de-alumination process has been studied quite extensively, also identifying the extra-porous species that are created in this process.[23,34] Using what is already known about the chemical process of de-alumination and the results obtained here, a hypothetical mechanism for the process involving binder effects can be created. Since the dehydration of methanol, coupled with the high temperature and pressure essentially steams the catalyst in the MTO reactor, any revelations in the characterisation of hydro-thermal treatment can also be applied to realistic reactor conditions.

3.1 Characterisation

3.1.1 X-ray Diffraction

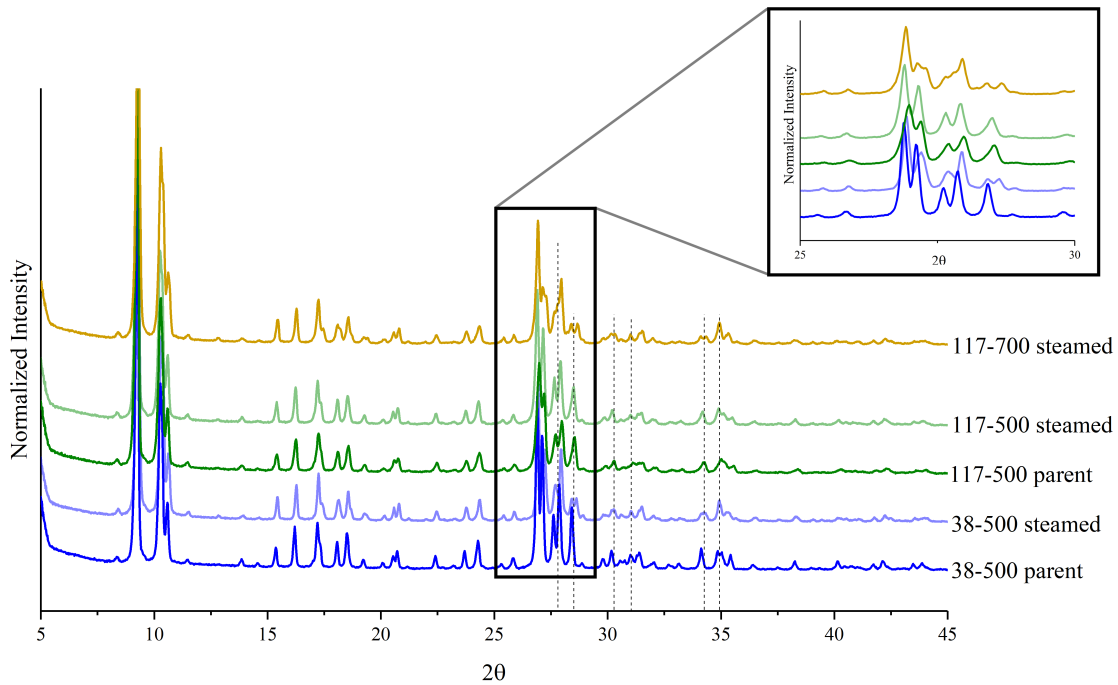

Figure 3.1: X-ray Diffraction patterns of ZSM-5 powder samples, slight changes in crystal structure can be observed at $2\theta \sim 27°$, 30°and 35°these changes are magnified in the sample steamed at 700°C.

XRD is used to examine the long range atomic structure of materials and in the case of zeolites, the patterns can inform us about framework topology as well as the positions of extra framework cations/adsorbed species.[5] For this purpose it is possible to observe the extent to which different steaming conditions affect the crystal structure. Ideally hydro-thermal treatment should change the acid sites while not resulting in degradation of the zeolite framework. Aramburo *et al.* hydro-thermally treated a SAPO-34 zeolite (Si/Al = 37) at 700°C and compared it to the parent zeolite. XRD measurements on the steamed sample showed a large loss in crystallinity, evident by peak broadening and increase in overall background caused by amorphous material.[70] However in another study involving ZSM-5 crystals (Si/Al = 17), steaming temperatures of 500°and 700°C resulted in no detrimental effects to the zeolite framework.[31] Based on these results, an optimum steaming temperature for further use in this project needs to be determined.

XRD measurements were performed on the powder zeolite samples under investigation and the results are summarised in Figure 3.1 . All parent zeolite diffraction patterns are in accordance with the reference data for calcined ZSM-5.[71] The patterns indicate that despite the de-alumination process, both zeolite samples maintain their crystallinity. Changes at $2\theta = 27°$, 30°and 35°show a subtle loss in crystallinity and peak broadening, most likely arising from the hydrolysis of Al atoms from the framework structure.[70] The sample steamed at 700°C showed a greater change in crystal structure in the $2\theta = 26°$region, indicating that severe steaming conditions resulted in a larger loss of crystallinity. Therefore, we can establish that severe steam treatment at 700°C is detrimental to the zeolite crystal structure and should not be used further.

Diffraction patterns were also obtained for the zeolite extrudates under investigation, and the results are summarised in Figure 3.2, the purpose of which, as before is to identify if any noticeable changes to the crystal structure occur under hydro-thermal conditions in the presence of a binder. Similar to the powder samples, the steamed extrudates show minor changes compared to the parent catalysts. Certain peaks arising from the alumina binder can be seen at $2\theta = 17°$and 34°but are mostly buried

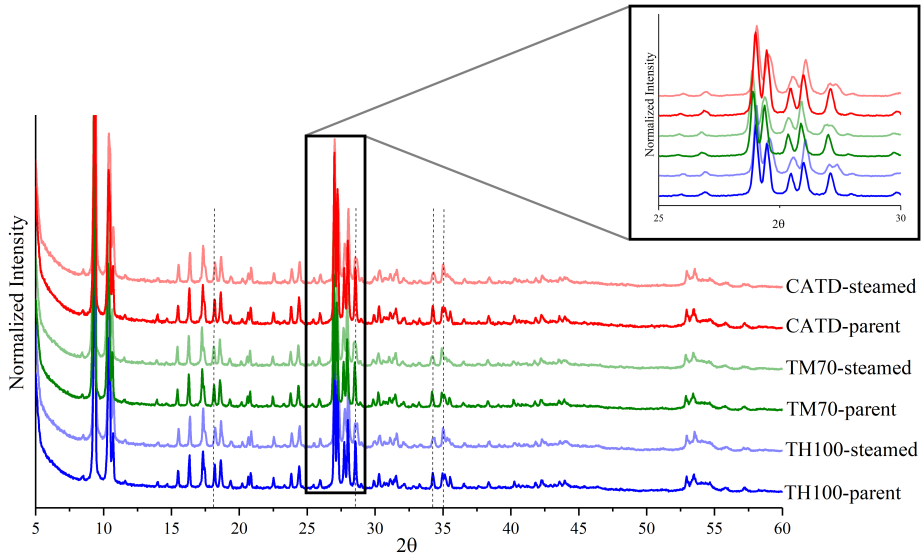

Figure 3.2: X-ray Diffraction patterns of ZSM-5 Extrudate samples steamed at 500°C. The 2θ = 53-55°region shows an area of increased background, indicative of slightly amorphous material, most likely the binder.[70] It appears all samples maintained their crystallinity after hydro-thermal treatment.

under the zeolite signal or background noise (Appendix Figure 13). The 2θ = 53-55°region shows an area of increased background, indicative of slightly amorphous material, most likely the binder.[70] Regardless, the patterns indicate that despite Al migration from the framework all samples retain a great deal of crystallinity.

3.1.2 Ar Physisorption

Physisorption was used to probe the dimensional properties of the zeolites and extrudates. After hydro-thermal treatment the process of de-alumination should result in the formation of meso-pores which, in turn causes a reduction in micro-porosity. Maier *et al.* used N_2 physisorption to quantify the changes that occurred in zeolite BEA upon hydro-thermal treatment for 24 h. Steaming resulted in a reduction of micro-pore volume by 19 % as well as a decrease in BET surface area.[25] However, the specific interaction of N_2 with the adsorbant surface affects the micro-pore filling pressure, with very slow diffusion at low pressures, making it difficult to measure equilibrated adsorption isotherms.[72] For these reasons, Argon was used to charac-

terise these materials.

Results for BET surface area and pore volumes can be seen in Appendix Table 2. With the exception of the 117-500 parent/steamed sample, which shows the same micro-pore volume, all parent samples show a reduction in BET surface area and micro-pore volume upon steaming, consistent with results seen in literature.[25] The micro-pore volume for 117-500 parent/steamed remained unchanged, compared to 38-500 which showed the largest change in this volume. These results show a higher alumina content zeolite exhibits a larger loss of micro-porosity, which can be correlated to a greater degree of de-alumination. The total pore volume was not interpreted quantitatively as the measurement also incorporates the external surface of the materials. Therefore, further analysis of the isotherms and pore-size distributions will be done in a qualitative manner.

As depicted in Appendix Figure 2 the adsorption and desorption isotherms of ZSM-5 were typical for small spheroid aggregates formed by smaller individual particles.[35] The isotherms are classified as Type I, which is characteristic of micro-porous solids, while the hysteresis loop is Type H4 and is associated with narrow slit-like pores.[73] In the case of 117-500-steamed a slight change in the hysteresis cycle appears at high partial pressures, compared to the parent zeolite. This change is indicative of the formation of meso-pores through hydro-thermal treatment. 38-500-steamed exhibits a similar trend where the variation in hysteresis cycle is observed at a higher partial pressure, indicating the possibility of more pronounced meso-pore formation.[74]

The pore size distribution can be seen in Figure 3.3 where all samples exhibit a relatively wide variety of pore sizes. The increase in meso-pore volume after hydro-thermal treatment is more easily visualised in this graph. The high silica content zeolite shows a small increase in the larger diameter pores (Figure 3.3a). A much larger increase is seen in the high alumina content zeolite (Figure 3.3b), showing a large adsorption in the meso-pore range, which correlates to an increase in total pore volume (Appendix Table 2). This is in line with the trend of increased de-alumination, and hence meso-pore formation with a lower silica/alumina ratio.

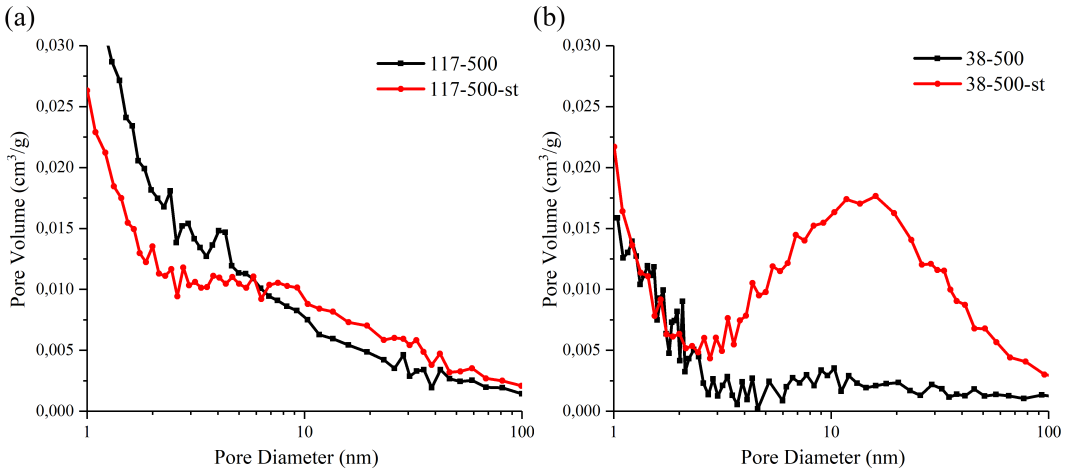

Figure 3.3: Pore size distribution for (a) 117-500-parent/steamed (High silica content zeolite) and (b) 38-500-parent/steamed (high alumina content zeolite), determined by BJH adsorption with Argon. The more Al rich zeolite exhibits greater framework de-alumination upon steaming and therefore a larger distribution in the meso-pore range.

Depicted in the Appendix Figure 3, the adsorption and desorption isotherms of the extrudate samples are noticeably different from the powder zeolites. Isotherms of Appendix Figure 3a-b can be classified as Type IV, which is characteristic of meso-porous adsorbants, while the hysteresis is most similar to Type H2, although it is difficult to interpret. The rest of the samples (Appendix Figure 3c-f) are not easily discernible. The isotherm is between a Type II (non-porous) and Type IV (meso-porous) while the hysteresis is somewhere between Type H1 and H2. Interpreting these isotherms has proved difficult, as the pore size distribution and shape are not well defined.[73] In the case of TH100 (Figure3e-f) the hysteresis cycle appears at a slightly higher partial pressure compared to the other samples, most likely due to meso/macro-pores orginating from the binder and inter-particle spacing.

The pore size distribution of the zeolite extrudates can be seen in Figure 3.4. All samples show adsorption in the meso/macro-pore range. The main cause of this phenomena is the binder, which accounts for the large meso/macro-pore range in addition to inter-particle spacing. Pore size distributions of the binders can be seen in Appendix Figure 14. The distributions are especially broad for the TM70 and TH100 samples, which could possibly be attributed to the smaller crystal size and

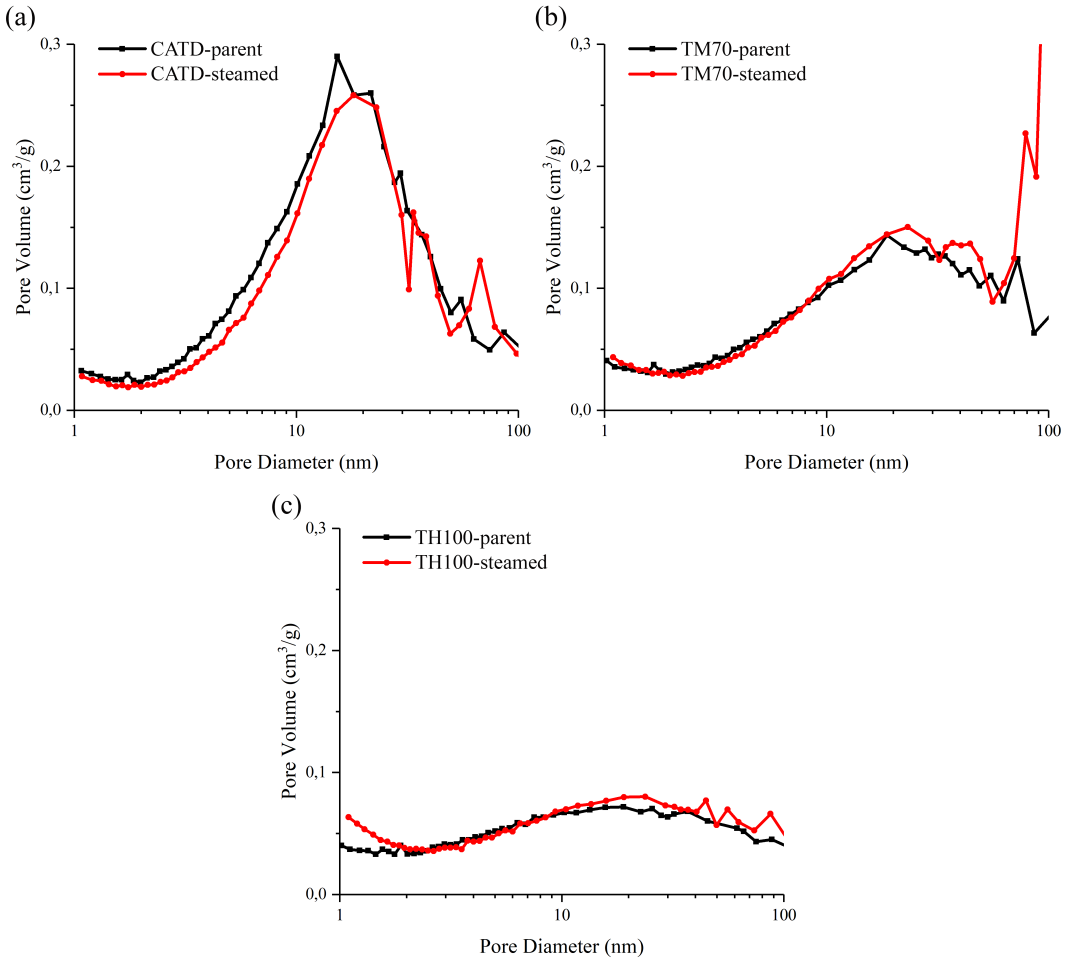

Figure 3.4: Pore size distributions of extrudate samples (a) CATD-Parent/Steamed, (b) TM70-Parent/Steamed and (c) TH100-Parent/Steamed. All samples exhibit a very large distribution of pores, largely due to the meso/macro-porous nature of the binder as well as inter-particle spacing.

thus, larger distribution of inter-particle spacing (Appendix Figure 1). It should be noted the BET surface area and pore volume results obtained here are different to those provided by the manufacturer. As with the powder samples, hydro-thermal treatment changes the distribution due to the formation of meso-pores. However, unlike 38-500-parent the change is not as pronounced, while this can be attributed to there being half as much zeolite by mass in the sample it could also indicate that de-alumination takes place to a lesser extent in the presence of a binder.

A large increase in pore volume is seen at $\sim$ 90 nm pore diameter for TM70-steamed. While this result can be linked to the known macro-porosity seen in this sample

it is important to consider that the BJH analysis used here is not applicable for the characterisation of pores in this size range.[72] Therefore, without alternative techniques such as mercury porosimetry, definitive characterisation of the macro-pore size range is not possible.

Overall, physisorption has shown that a higher framework Al content in zeolites results in more de-alumination. Since acid site concentration/strength can be correlated to Al content, further characterisation of these effects is explored through acidity measurements.

3.1.3 NH_3-TPD

Ammonia Temperature Programmed Desorption (TPD) is used to determine the concentration of acid sites corresponding to peak area while temperature of the peak maxima can be correlated to acid site strength.[5] The relatively small molecular size of ammonia allows it to probe the narrow pore structures of zeolites, able to access acid sites on the surface as well as the interior. Furthermore NH_3 is a strong base and produces reliable acid strength measurements based on chemisorption energies.[6] For this purpose the changes in acidity that occur after hydro-thermal treatment can be easily quantified and used to determine to what extent each type of acid site is affected by the steaming process. Comparison of the powder and extrudates was done in a qualitative manner. Since it is not possible to definitively differentiate between zeolite and binder acidity the extrudate graphs were not normalised to the zeolite/binder ratio.

The results, shown in Figure 3.5 indicate a decrease in overall acidity (total area under desorption curves) after steaming. The absence of distinct desorption peaks for the 38-500 steamed sample, in particular towards higher desorption temperatures indicates that a total loss of strong acid sites occurs. Additionally, the shift in the peaks for the 117-500 steamed sample shows that the acid sites present after steaming are not only lower in concentration but also desorb at a lower temperature and

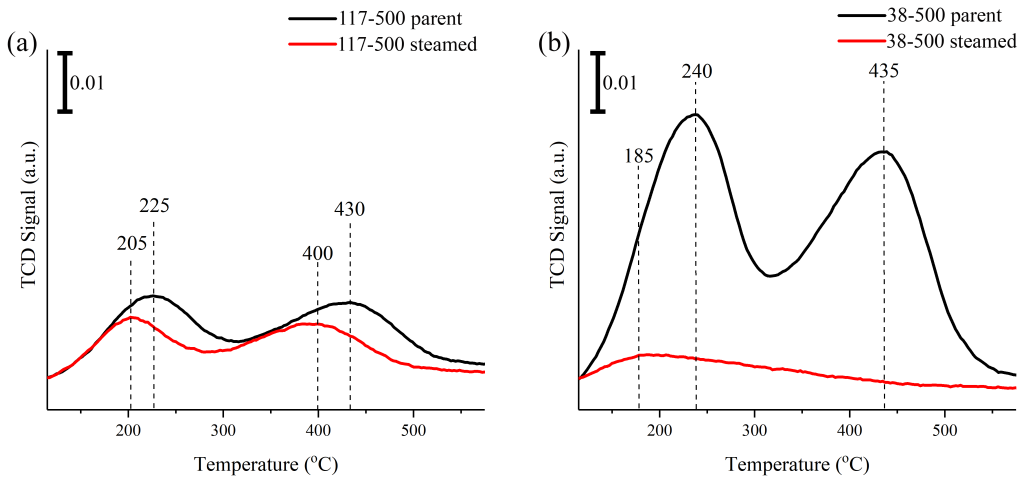

Figure 3.5: Ammonia TPD profiles of ZSM5 powder samples (a) 117-500 parent/steamed and (b) 38-500 parent/steamed. Decrease in overall acidity for all samples upon steaming due to de-alumination. Significant loss of all acid sites in the 38-500-steamed sample. Peak shifts towards lower temperatures indicate that acid site strength also decreases upon steaming.

are therefore weaker in terms of strength.[35] An alternative reason was proposed by Grejtak *et al* who conducted NH_3-TPD measurements on dealuminated naturally occuring zeolite clinoptilolite. Namely, the shift towards lower desorption temperatures was a result of increased probe molecule diffusion caused by the formation of mesopores.[75] Indeed the physisorption results (Figure 3.3a) did show a slight pore volume increase in the meso-pore range (10-20 nm). While this effect should not be ignored, acid site strenght should still be considered the deciding factor contributing to peak shift. Therefore, these results indicate that when tending towards a higher SiO_2/Al_2O_3 ratio (SAR) through de-alumination the lower concentration of BAS does not result in an increase in individual acid site strength.

Thus, we conclude that steaming has a significant impact on the acidic properties of ZSM-5 powder samples. As expected, the larger amount of framework Al induces a much higher concentration of acid sites in the 38-500 parent sample, compared to the 117. Furthermore, they appear to desorb at slightly higher temperature compared to the high silica content zeolite, indicating that in this case, strength of the acid sites is not compromised by increased concentration.

Desorption and relative intensity are consistent with those seen in literature for ZSM-5 with similar SAR.[76] Aramburo *et al.* conducted NH_3-TPD analysis on ZSM-5 (Si/Al = 11) steamed at 600, 700 and 800°C. Mild steaming temperatures resulted in a loss of overall peak area and a shift towards lower temperatures. Severe steaming at 700/800°C resulted in complete loss of both types of acid sites. These trends correspond to those seen in 117-500 parent/steamed and 38-500 parent/steamed respectively.

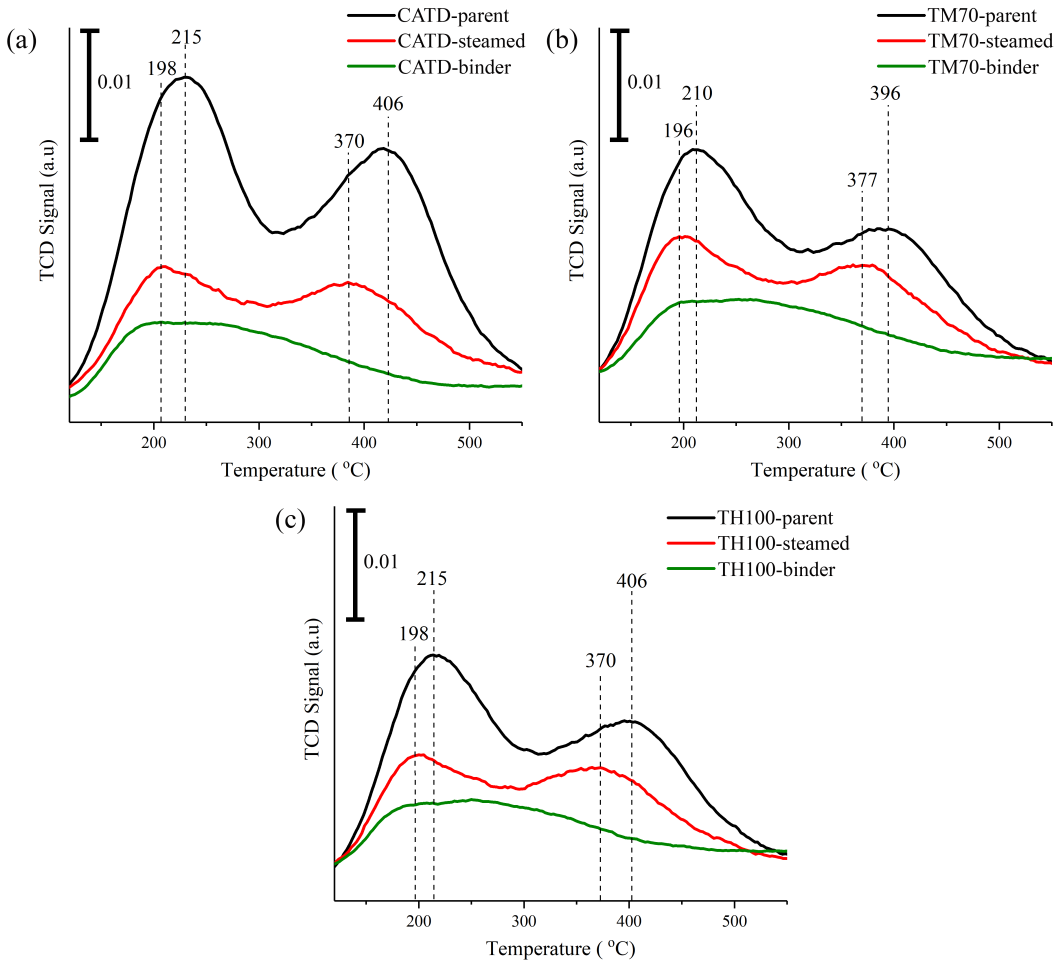

Figure 3.6: Ammonia TPD profiles of extrudate samples (a) CATD-Parent/Steamed, (b) TM70-Parent/Steamed and (c) TH100-Parent/Steamed and their corresponding binders. Decrease in overall strong and weak acid site concentration upon steaming, with the largest difference seen in (a), although no definitive reason can be found for this result. Binder peaks show majority of strong and weak acid sites originate from the zeolite. Peak shift towards lower temperature indicates a decrease in acid site strength.

The TPD profiles were de-convoluted (Appendix Figure 4) and the weak/strong acid site concentrations are displayed in Table 3.1. From the de-convoluted peaks we observe the presence of a third 'intermediate' acid strength peak. These can be assigned to mainly; mildly acidic silanol groups, Lewis acid sites and Brønsted acid sites respectively.[58]

The changes in acidic properties resulting from hydro-thermal treatment of the extrudates were also investigated through TPD measurements, and the results are shown in Figure 3.6. As with the powder samples, the extrudates also showed a decrease in overall strong and weak acid site concentration upon steaming, with the largest difference seen in the CATAPAL D binder sample (Figure 3.6a). A similar shift to the powder samples is observed, indicating that the acid sites present after steaming also desorb at a lower temperature and are therefore weaker than in the parent. A comparison with the powder zeolite equivalent (Figure 3.5b) indicates the extrudate peak shift is far less significant.

The curves were deconvoluted (Appendix 5) and the weak/strong acid site concentrations are displayed in Table 3.1. Comparing results for the extrudate samples with those of the powder zeolite (Table 3.1) it is apparent that the concentration of acid loss is much less in the extrudates. In particular, the strong acid sites which almost completely disappeared in 38-500-steamed, are still present. This effect will be discussed further in subsequent sections. The CATD sample experiences the largest loss in strong and weak acid sites, excluding any discrepancies arising from the measurement itself it appears the only other variable that could cause this result originates from the binder. While it is possible to relate this effect to the properties of the binder, such as larger particle size and surface area, it is difficult to identify a single factor that contributes the most to this effect. Furthermore, the effects of these properties may vary with the degree to which the extrudate is crushed during sample preparation.

Finally, while TPD is an effective technique to quantify acid sites, even those deep in the zeolite structure, it is unable to classify the exact nature of the acid sites

Concentration of Acid Sites ($mmol/g$)			
Sample	Weak	Intermediate	Strong
117-500 parent	0.13	0.05	0.12
117-500 steamed	0.07	0.03	0.10
38-500 parent	0.47	0.13	0.37
38-500 steamed	0.04	0.01	0.03
CATD-parent	0.32	0.08	0.22
CATD-steamed	0.07	0.03	0.13
TM70-parent	0.17	0.08	0.17
TM70-steamed	0.08	0.04	0.13
TH100-parent	0.18	0.06	0.16
TH100-steamed	0.06	0.03	0.12

Table 3.1: Weak, intermediate and strong acid site strength determined via deconvolution of Ammonia TPD peaks. hydro-thermal treatment results in a significant change in weak acid sites as well as changes in intermediate and strong acid sites concentrations.

present. Therefore, we require further techniques with different probes to properly identify these sites.

3.1.4 CO-IR

Adsorption of CO, followed by infra-red spectroscopy was used to probe the strength of the acid sites and can be used in conjunction with TPD to effectively quantify the nature and change in acid site concentration upon hydro-thermal treatment. The CO stretching region gives information about how the C-O bond is pertubed upon adsorption and can therefore be used to determine the presence of Brønsted/ Lewis acid sites; carried out at low temperature (100K), so it is more sensitive to the presence of weaker acid sites. Figure 3.7 shows the spectra for all powder zeolite

samples. The characteristic Brønsted acid site peak at ∼2175 cm^{-1} is seen in all samples except in 38-500-steamed, where it is almost completely absent.[58]

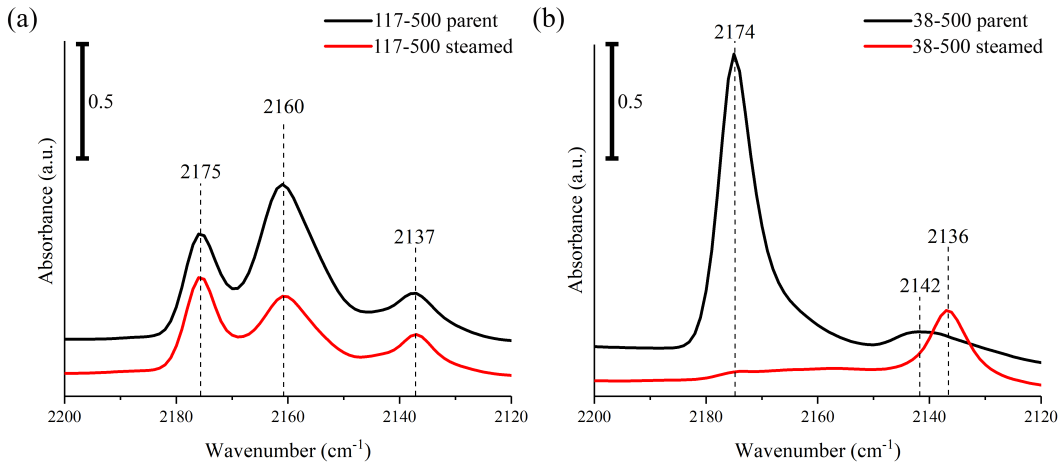

Figure 3.7: CO IR spectra for powder samples (a) 117-500 Parent/Steamed (b) 38-500 Parent/Steamed. Peaks seen at 2174-2175 cm^{-1}, 2160 cm^{-1} and 2136-2142 cm^{-1} correspond to Brønsted acid sites, silanol groups and physisorbed CO respectively. As with the pyridine and TPD data, the largest difference is seen in the 38-500 sample which exhibits a large change in the Brønsted acid peak while the 117-500 shows a uniform decrease in all peaks.

Physically absorbed CO, which can be observed at ∼2140 cm^{-1} is seen for all samples. The larger peak is observed for 38-500-steamed, showing that a majority of CO molecules are not absorbed onto the surface of the sample and is therefore consistent with the lower strength of Brønsted acidity. Silanol groups at ∼ 2160 cm^{-1} are displayed very prominently in 117-500-parent/steamed, while being absent in the 38-500 samples; the broadness of the Brønsted acid peak for the 38-500-parent most likely consists of the silanol peak as well. Goetze *et al.* obtained similar results for CO FTIR on powder ZSM-5 (Si/Al = 50) with Brønsted acid sites, silanol groups and physisorbed CO occuring at 2176 cm^{-1}, 2159 cm^{-1} and 2137 cm^{-1} respectively.[58] As seen in the NH_3-TPD results a complete loss of all types of acidity is observed for 38-500-steamed. CO FTIR confirms the trend seen in TPD, indicating that indeed, zeolites with higher alumina content in the framework are more susceptible to de-alumination through hydro-thermal treatment.

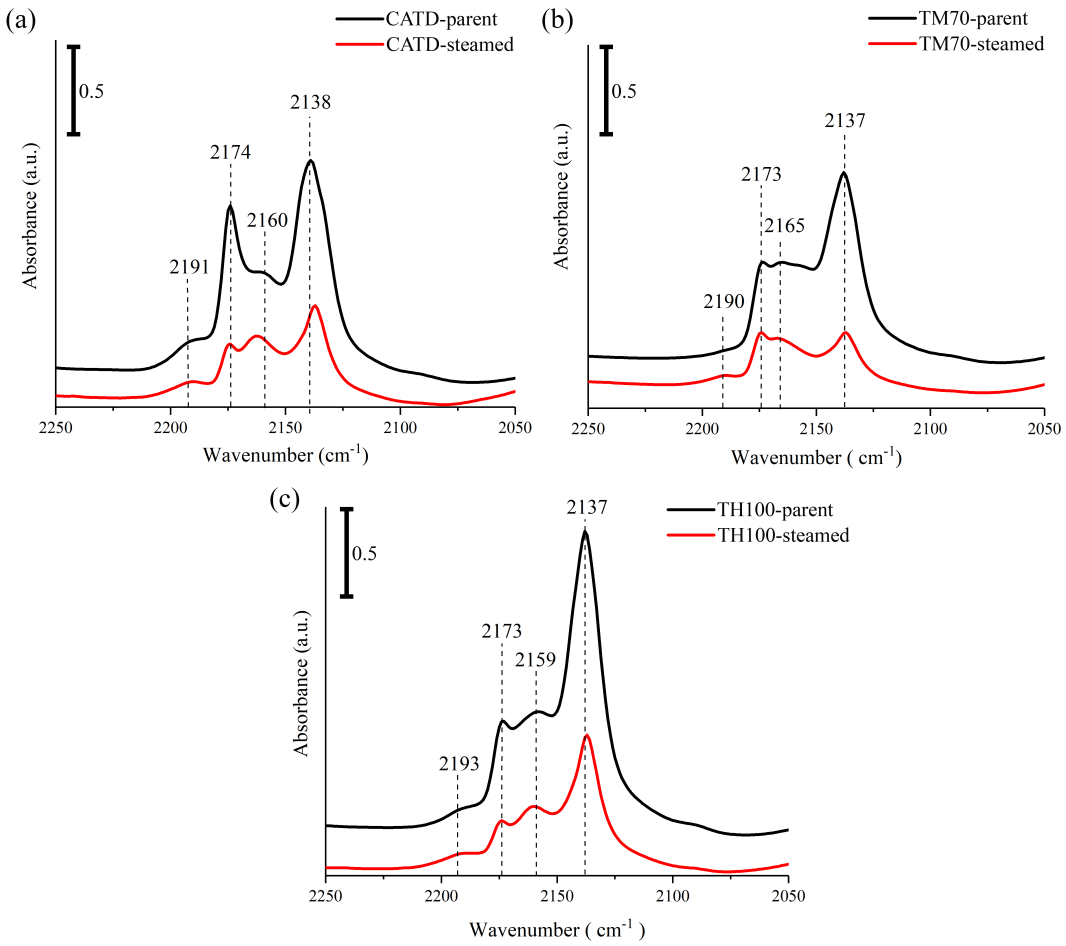

Figure 3.8: CO IR spectra for extrudate samples (a) CATD-Parent/Steamed, (b) TM70-Parent/Steamed and (c) TH100-Parent/Steamed. Spectra are plotted with an offset for clarity. A large amount of physisorbed CO is seen, due to the "flooding" technique used. More peaks are observed compared to powder samples, indicating presence of extra-porous aluminium species.

Figure 3.8 shows the spectra for all extrudate samples. Due to the significant overlap seen in all measurements, deconvolution (Appendix Figure 7) is neccessary to properly identify the peaks present. As with the powder samples the Brønsted acid peak at ~2175 cm^{-1} is visible for all samples, which also becomes less intense upon hydro-thermal treatment. This peak is overlapped by a broader peak between 2140-2180 cm^{-1} which corresponds to weaker Brønsted acid sites arising from mostly silanol groups.[58]

A very broad shoulder peak of varying intensity is seen in several of the samples be-

tween 2185-2200 cm^{-1} and can be attributed to extra-framework Al species present in the zeolite channels as oxides,[77] which was not observed in the powder samples, probably due to the absence of many extraporous Al species. Interestingly, while the TM70 and TH100 samples show an increase in this region upon steaming (as expected due to de-alumination), the CATD sample shows the opposite. However, this may indicate that other Al_{EF} species different to those seen in TM70/TH100-steamed are being formed. Due to the nature of the technique used here (evacuating down from 250 mbar) a large amount of physisorbed CO is seen at ~2140 cm^{-1}. A broad peak at ~2120 cm^{-1} is as of now, not identifiable. Since a different measurement procedures were used for the powder and extrudate samples a quantitative comparison is not possible. However, the nature of the spectra shows there to be many more CO adsorption sites in the extrudates, and therefore a larger range of different acidic sites, which would need to be taken into account when performing reactions with these catalysts.

For the powder samples; the Lewis acid site region, which occurs at >2180 cm^{-1} (not pictured), did not yield any relevant peaks to quantify LAS. The extruate samples showed a broad peak between 2185-2200 cm^{-1} but this appeared to overlap with the Brønsted acid peak. Therefore, a more sensitive probe molecule coupled to FTIR is needed to properly differentiate between Lewis and Brønsted acid sites.

3.1.5 Pyridine IR

Pyridine Fourier Transform Infra-Red (FTIR) can be used to determine the nature and strength of acid sites through desorption.[78] In this case Pyridine IR was used to probe the Brønsted and Lewis acid site concentrations of the ZSM-5 samples before and after hydro-thermal treatment. As discussed earlier, the process of steaming results in framework de-alumination, resulting in a loss of BAS while increasing the LAS concentration through the formation of Al_{EF} species. This technique is often used as a post synthesis modification in order to tune the acid site properties of zeolite catalysts. Therefore changes seen in Brønsted and Lewis acid sites need to

be properly quantified in order to obtain the desired catalytic reactor conditions. Pyridine FTIR is ideal for monitoring changes in acid sites simultaneously and these trends should be reflected in the peaks corresponding to Brønsted and Lewis acidity.

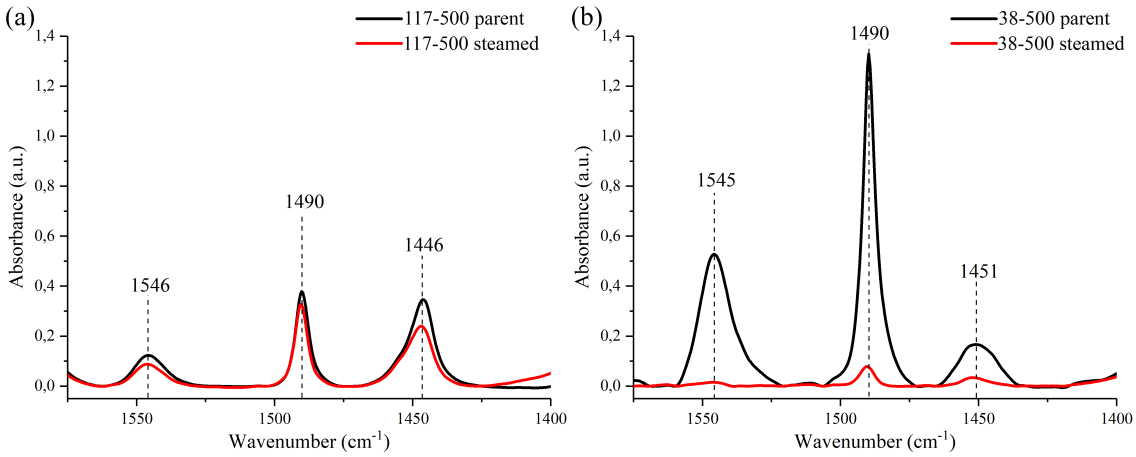

Figure 3.9: Pyridine IR spectra for the zeolite powder samples. 117-500 remains largely unchanged after hydro-thermal treatment. 38-500-steamed shows a complete loss of Brønsted acid sites and a large decrease of Lewis acid sites upon steaming. Clearly, hydro-thermal treatment results in a high degree of de-alumination in low silica/alumina ratio zeolites.

Three distinct bands in the 1600-1400 cm^{-1} region can be observed for the powder zeolite samples (Figure 3.9). These correspond to the C-C stretching vibration of the pyridinium ion (1545 cm^{-1}) used to detect the presence of Brønsted acid sites while Lewis acidity arises from the band at 1450 cm^{-1} which is associated with the C-C stretch of a coordinately bonded pyridine complex. The band at 1485 cm^{-1} arises from a combination of the BAS and LAS sites and is therefore not useful for identification.[79] The sharp peaks in the Brønsted/Lewis acid regions allow us to effectively visualise the changes that occur due to hydro-thermal treatment, where the overall loss in acid site strength is more significant in the high alumina content zeolite (Figure 3.9b).

The numerical concentrations of the acid sites can be seen in Table 3.2. The Ammonia TPD results (Figure 3.1) showed the same trend, but reported higher concentration values. This can be attributed to the higher accessibility of the NH_3 molecule,

allowing it to probe smaller pores.[80] Thus, the pyridine IR and NH_3-TPD data indicate that the higher alumina content ZSM-5 is more prone to de-alumination as a result of steaming, due to the larger amount of Si-OH-Al bonds available for cleavage. In contrast, the low Al content in the 117-500 parent/steamed samples limits the extent of aluminium extraction from the framework structure during hydro-thermal treatment.[81]

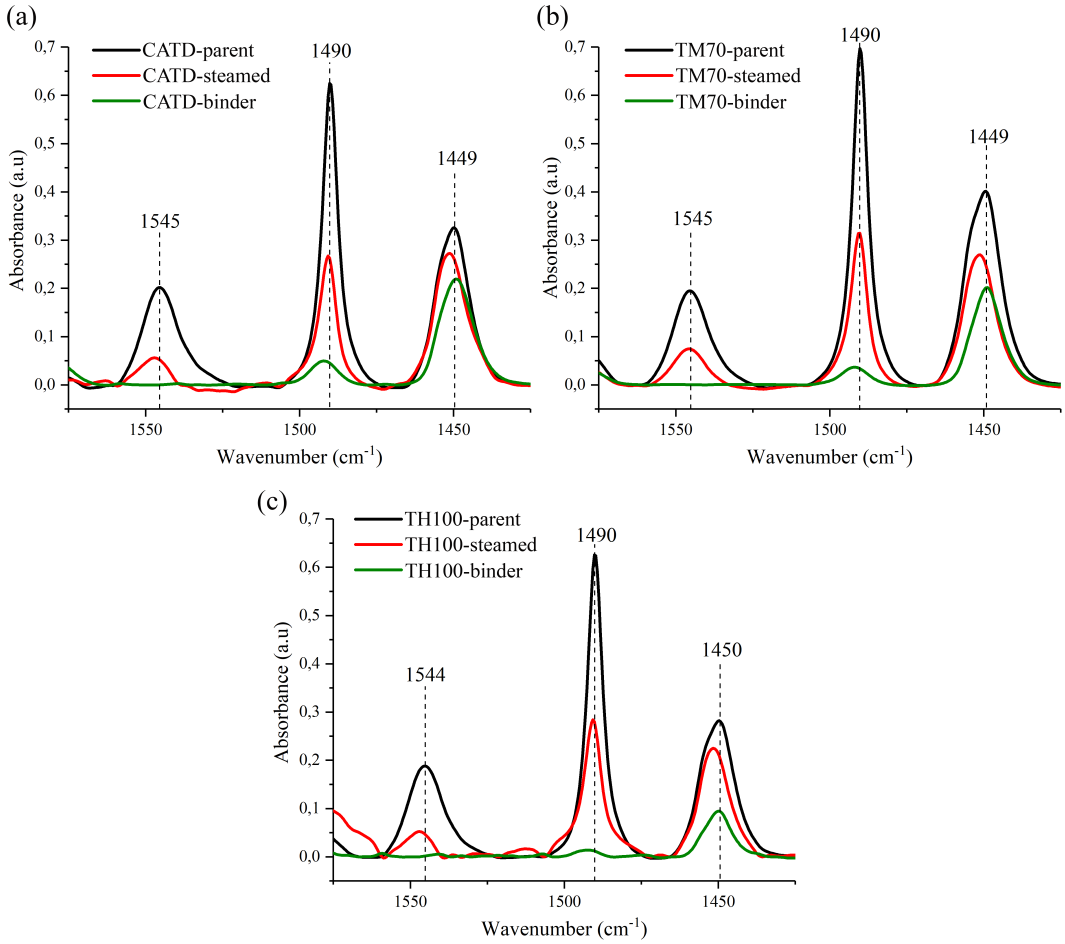

Figure 3.10: Pyridine IR spectra for extrudate samples (a) CATD-parent/steamed, (b) TM70-parent/steamed, (c) TH100-parent/steamed and their corresponding binders. All spectra were normalized to pellet mass, while binder only spectra was also normalised to zeolite/binder ratio. All spectra show significant absorbance in Lewis acid site region, attributed mainly to the binder. Some amount of Brønsted acid sites also appear to be retained compared to the powder sample. Evidently, the presence of an alumina binder causes the zeolite to be more resistant to de-alumination.

Pyridine FTIR was also carried out on the extrudate samples before and after hydro-thermal treatment (Figure 3.10). The alumina binder is known to be Lewis acidic and therefore a relatively large peak corresponding to LAS is seen in the 1455-1445 cm^{-1} region for all samples. In the case of the parent samples, this region appears to be a more complex peak made up of an absorbance at ∼1445 cm^{-1} corresponding to pyridine adsorbed on less accessible aluminium cations further inside the zeolite interior and hydroxyl groups (most likely from the binder) while the shoulder at ∼1455 cm^{-1} can be attributed to easily accessible extra framework Al species.[34] This trend in the Lewis acidic region was not observed by Zhang *et al.* for the steaming of alumina bound zeolite extrudates (70:30 zeolite binder ratio) but was however, observed by Ong *et al.* while applying a harsh steam treatment (960 °C) to powder zeolites (Si/Al = 87). Therefore this effect most likely arises from the zeolite.[34,47] Interestingly, this complex peak merges into a single slightly blue-shifted absorbance peak upon steaming. A large part of this absorbance can be attributed to the Lewis acidic binder, as evident by the overlapping peaks. Clearly, the Lewis acidic species formed after hydro-thermal treatment are of similar strength to the binder and experience the same form of coupling with pyridine.

As stated before, hydro-thermal treatment is often used to tune the acidic properties, in this instance several changes in the ratio of [BAS]/[LAS] can be observed (Table 3.2). Applying the same steaming conditions to all extrudates, CATD and TH100 show very similar ratio's before and after steaming. TM70 on the other hand appears to have a noticeably higher initial LAS concentration and after steaming for BAS concentration. While this binder has several parameters differentiating it from the others (surface area, pore volume etc.), as of yet no single parameter could be linked to this result.

The binder spectra are characteristic of γ-alumina, with a strong absorbance in the Lewis acidic region (∼1449 cm^{-1}). Since alumina requires no counter-ion to maintain charge neutrality, no pyridinium ion stretch corresponding to Brønsted acidity is seen.[82] A slight absorbance at ∼1490 cm^{-1} in the binder spectra can be seen, leading to the assumption that the intensity decrease of the peak in this region

Sample	[BAS] μmol/g	[LAS] μmol/g	[BAS]/[LAS] ratio
117-500-parent	56.5	110.2	0.51
117-500-steamed	37.6	78.1	0.48
38-500-parent	252.5	65.1	3.88
38-500-steamed	5.5	10.0	0.55
CATD-parent	100.9	110.0	0.92
CATD-steamed	19.9	92.0	0.22
TM70-parent	92.0	142.4	0.65
TM70-steamed	29.7	87.5	0.34
TH100-parent	88.7	94.4	0.93
TH100-steamed	17.0	68.4	0.25

Table 3.2: Brønsted and Lewis acid concentrations determined from integrating the corresponding Pyridine IR peaks and normalising to pellet mass.

upon steaming can be largely attributed to the change in Brønsted acid sites of the zeolite. The peaks of all steamed samples are also blue-shifted, indicating a change in acid site strength. This is indicative of the shift towards lower temperatures seen in the NH_3 results (Figure 3.6) showing a decrease in overall acid site strength.

As evident from these results, significant changes can be seen between the parent and steamed samples for both powder and extrudate samples. Interestingly, it appears the Brønsted acidity loss in the extrudates is mitigated compared to the powder 38-500-steamed, indicating some form of stabilisation of the acid sites is occurring. In order to better visualise and possibly identify the nature of these results a kinetic study of the de-alumination process will need to be conducted between 0 and 7 h steaming time. Additionally this will also allow us to identify the Lewis acid trend, where the initial Al_{EF} sites aggregate to form weak/non-acidic species towards longer hydro-thermal treatment times.

3.1.6 De-alumination Kinetics During Hydro-thermal Treatment

From the pyridine IR results discussed in the earlier sections we can conclude that the powder zeolite, in particular 38-500-parent has a much larger decrease in Brønsted acidity compared to its extrudate counterparts. It is known that highly silicious zeolites are more resistant to hydro-thermal treatment,[34] which is reflected in the acidity loss for the 117-500-steamed sample in the results presented here. Therefore, for the higher alumina content zeolite to retain its acidity to a certain degree in extrudate form while its original powder form showed almost no Brønsted acidity upon steaming, indicates that some form of acid site stabilisation occurs in alumina bound extrudates.

In order to better understand and visualize the changes in acidity that occur in the powder versus the extrudate, a kinetic study of the Brønsted/Lewis acid concentrations over different times under hydro-thermal conditions was conducted. Such as study has already been done on ZSM-5 powder[34] but no comparative study on extrudates exists. Both 38-500-parent and CATD-parent were chosen as powder and extrudate samples respectively, where any changes to acid site concentration could easily be observed.

Figure 3.11 shows the changes in acidity that as a function of time under hydro-thermal treatment. It is evident that both Brønsted and Lewis acid site densities decrease at the same time. This is contrary to the mechanism which shows an increase in LAS at the expense of BAS due to steaming.[6] One reason for this may be the excessive build up of extra-porous Al species which prevent the pyridine probe molecule from accessing the LAS within the framework. These species may polymerise to form species with low acid strength, which can be seen in the shift towards lower temperature desorption in the TPD data (Figure 3.5 and 3.6). It is possible that the peak seen in the low temperature region after steaming in the TPD graphs arise from mostly non-acidic species,[83] could be the reason for these trends..

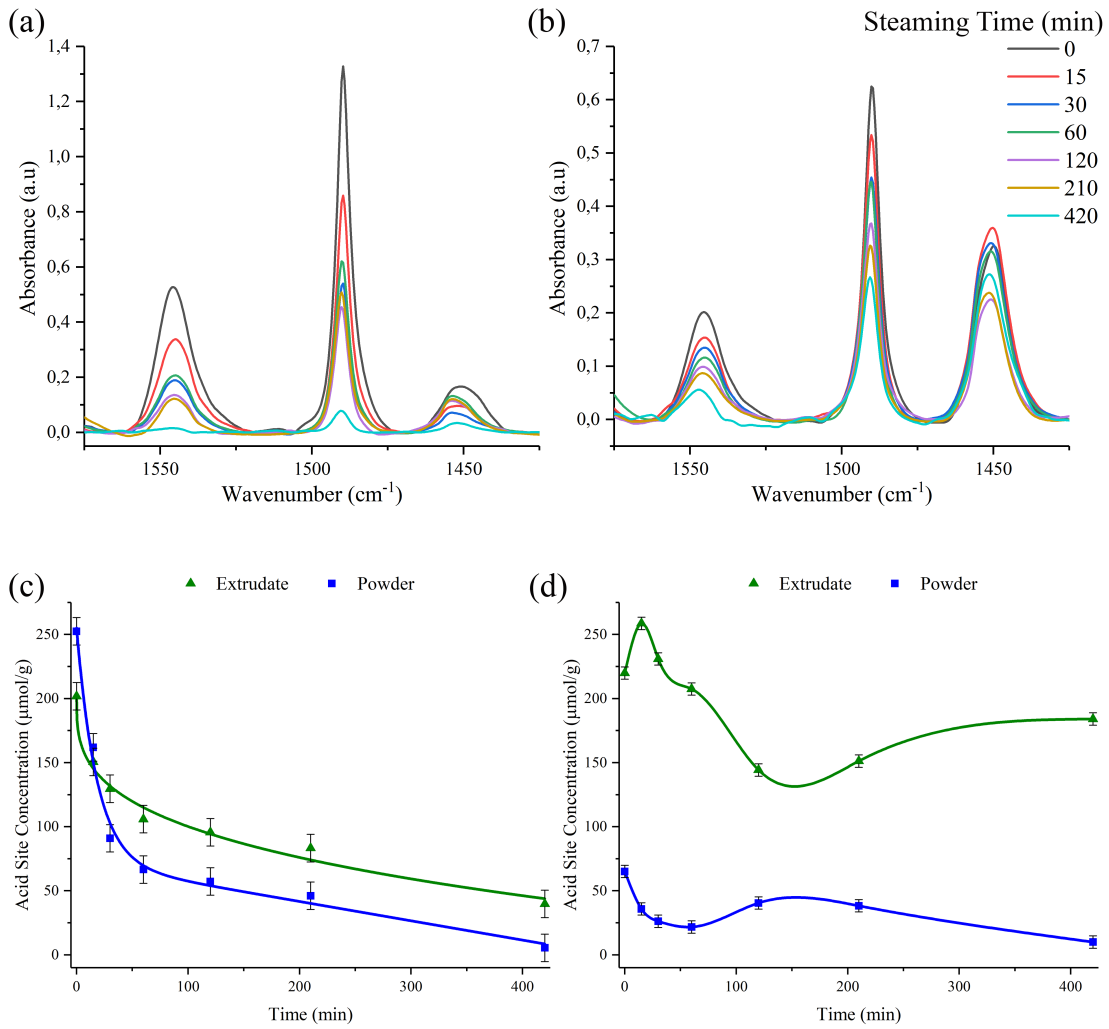

Figure 3.11: Pyridine IR spectra of (a) powder zeolite and (b) extrudate samples as a function of steaming time. Comparison between powder and extrudate acidity concentrations over time for (c) Brønsted acidity and (d) Lewis acidity (only Brønsted acid curve was normalised to zeolite content) Brønsted acid curve clearly shows extrudate dealuminates to a lesser extent over time compared to powder zeolite, indicating a stabilisation effect. Lewis acid site (LAS) curve for extrudate shows a slight increase at 15 minutes steaming time consistent with initial stage of de-alumination. A large decrease in LAS concentration follows, most likely caused by the migration of Al atoms back into the zeolite framework via extra-porous Al species, referred to as "re-alumination".

Additionally, no major shift in Brønsted acid peaks is seen upon steaming, contrary to the accepted opinion that Brønsted acid site strength increases with a reduction in acid site density.[6] Again, the inaccessibility of the pyridine molecule into the

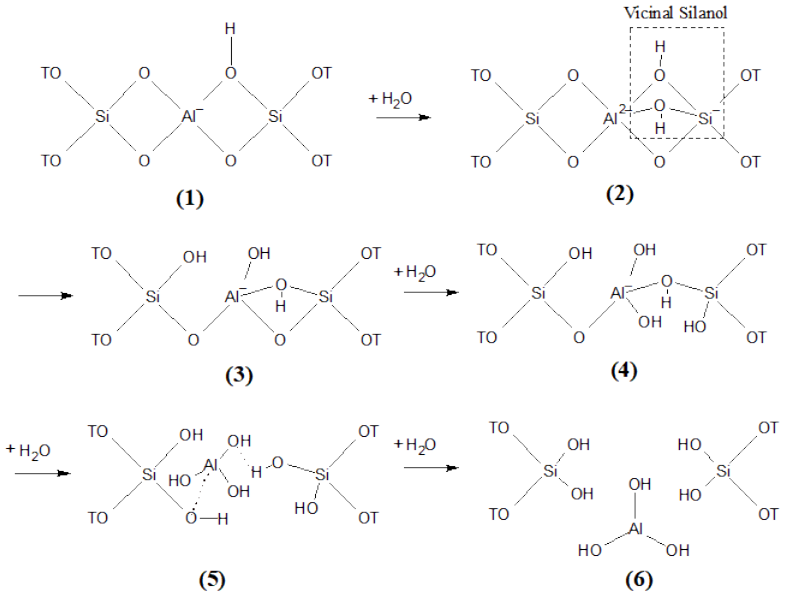

Figure 3.12: Scheme for de-alumination, reproduced from Silaghi et al.[23] Silanol nests form upon de-alumination while extra-porous Al species created remain in close proximity to the zeolite framework.

zeolite channels where the strongest Brønsted acid sites are presumed to be, and/or the conversion of Si-OH-Al sites to weaker/non acidic sites[83] is determined to be the reason.

The change of BAS concentration over time in Figure 3.11, clearly shows the extrudate to be more robust in terms of acidity loss. A higher initial concentration is seen for the powder compared to the extrudate, despite normalising. This is most likely due to the in-accessibility of the pyridine molecule into a large portion of the zeolite channels, due to blockage by the binder. The initial sharp loss in acidity follows the standard mechanism for de-alumination[23] (Figure 3.12), where the addition of one water molecule for each step causes the breaking of each Al-O-Si bond (with the exception of the first step), resulting in the formation of Al_{EF} and silanol nests (Figure 3.12(6)).

There are several theories to explain the stabilisation of the BAS in the extrudate. The first is that the zeolite is shielded from acidity loss by the binder. However, since we see a sharp increase in LAS upon steaming of the extrudate as well, it is

unlikely this effect plays a major roll. Additionally, there is no mechanism by which Al species can stabilise the zeolite acidity without also neutralising the BAS.[34] A more likely explanation is that Al_{EF} species created as a result of steaming and from the binder cause Al migration back into the zeolite framework. A third theory, investigated by Yu *et al.* is that the close proximity of BAS and Al_{EF}, seen in Figure 3.12(6) causes a partial electron transfer from the framework OH bond to $Al(OH)_3$ species, which increases acid site strength through a decrease in OH bond length.[84] However, this concerns mainly acid site strength and also occurs in zeolite powders, although Al_{EF} from the binder could amplify this effect and an indication as to why there is no substantial BAS peak shift.

For the LAS curve (Figure 3.11d); the initial loss in LAS in the powder sample can be attributed to the gradual loss of framework Al Lewis acidity, causing the formation of weak/non-acidic silanol nests. Resulting Al_{EF} from the de-alumination, causes the increase in LAS seen between 100-200 min. Al removed from the framework is present in the form of labile Lewis acidic cations such as Al^{3+}, AlO^{+}, $Al(OH)_2^{+}$, $AlOH^{2+}$ etc. In addition to these ions, neutral Al species such as AlO(OH), $Al(OH)_3$ and $Al(OH)_3{\cdot}H_2O$ can also be formed,[34] which can be attributed to the gradual decrease in acid sites seen towards excessive time under hydro-thermal treatment. The extrudates displays shows a different trend; the sharp increase in Lewis acidity is seen within 15 minutes of steaming, after which substantial loss in LAS concentrations is observed. The initial peak can so +assigned to the formation of Al_{EF} through de-alumination and/or the further reaction of mobile Al species originating from the binder.[23]

Aside from the pyridine coordinating acid site region, it is also possible to visualise the region corresponding to hydroxyl groups. Figure 3.13 shows the FTIR spectrum in the OH vibrational region. Both samples contain the characteristic bands for surface silanol groups ($\sim$3742 cm^{-1}), and zeolite framework OH groups (3608-3610 cm^{-1}) which is directly proportional to Brønsted acidity.[80] Therefore, we clearly see the loss in powder BAS as opposed to the extrudate, where the zeolite content results in lower initial acidic but the loss in peak intensity is largely mitigated. The

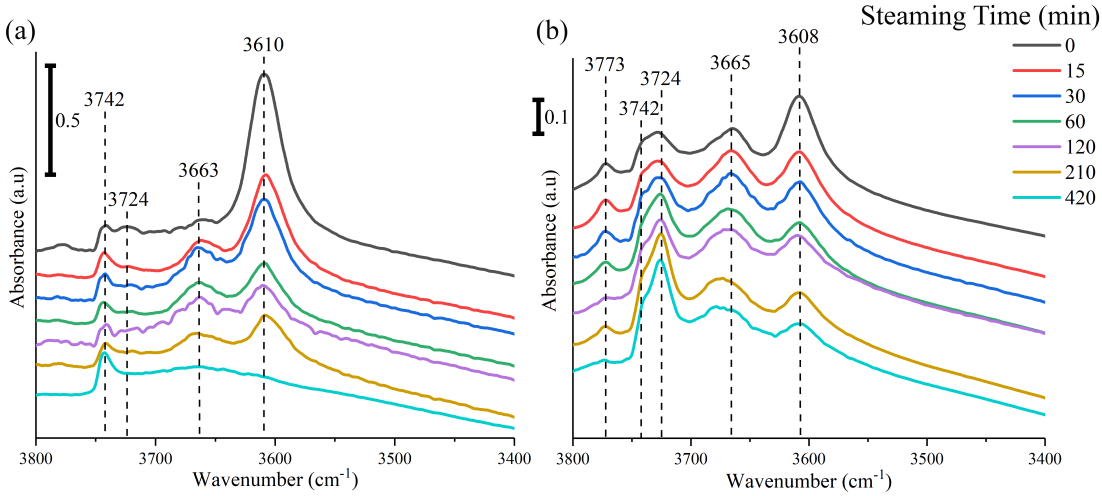

Figure 3.13: Pyridine FTIR spectra of the OH stretching region for (a) zeolite powder and (b) extrudate samples. Spectra were taken at room temperature under high vacuum after heating to 550°C and are plotted with an offset for clarity. Characteristic bands for surface silanol groups (∼3742 cm^{-1}), and zeolite framework OH groups (3608-3610 cm^{-1}) which are directly proportional to Brønsted acidity.[80] Change in the doublet of peaks seen at 3742-3724 cm^{-1} between t = 0 and t = 420 indicates an increase in surface Si-OH from the creation of silanol nests.

band at 3665 cm^{-1} in the extrudate also corresponds to Al-OH groups and shifts to the more characteristic 3670 cm^{-1} region at longer steaming times. This is due to partially framework bound Al species (Figure 3.12(5)) which then form Al_{EF}.[85]

The band at 3724 cm^{-1} can be assigned to silanol groups within the zeolite and a combination of such groups/aluminol in the extrudate sample.[23,80] As seen in the powder sample, the change in the doublet of peaks seen at 3742-3724 cm^{-1} between t = 0 and t = 420 indicates an increase in surface Si-OH from the creation of silanol nests. A larger increase in this region is also seen in the extrudate, but can be largely correlated to the freeing of Si-OH groups involved in H-bonding to Al-OH groups at the surface.[86]

In conclusion, it is clear the process of de-alumination and any following interactions are very complex, with several different species interacting within the system. Using the characterisation data measured thus far it is difficult to identify a single (or

multiple) mechanism by while the zeolite acidity is stabilised by the binder. Using prior literature and the data collected in this report it can be concluded that "re-alumination" does indeed occur to a significant extent. However further research is needed to provide insight into how exactly this phenomenon arises. While techniques such as pyridine FTIR and NH_3-TPD have proved invaluable for characterising the influence of hydro-thermal treatment on zeolites, they are somewhat unrealistic in terms of catalytic reactivity. Pyridine and NH_3 are strong bases compared to catalytic reaction molecules and therefore interact with weaker acid sites that may not participate in the reaction.[87] In order to properly observe the role of these acid sites it becomes necessary to observe their effects *in situ* using a model catalytic reaction.

3.1.7 UV-Vis Spectroscopy

Probe molecule reactions, such as the oligomerisation of thiophene or fluorostyrene, coupled to *in-situ* UV-Vis spectroscopy can be used to monitor the acidity changes in zeolites. The oligomerisation of 4-fluorostyrene has already been used to probe the acidity of zeolite powders steamed under various conditions while the acidic properties of zeolite extrudates have been investigated using thiophene as a probe.[74,88,89] Since the earlier characterisation data does not properly represent the behaviour of a catalyst under realistic reactor conditions it is necessary to use a model catalytic reaction (thiophene oligomerisation) coupled to *in-situ* UV-Vis spectroscopy to better understand the acidic properties. In this method, thiophene was added to the parent and hydro-thermally treated samples (powder and extrudates), with UV-Vis spectra recorded every 10 seconds.[88,89] As was evident in the acidity characterisation data, the extrudates retain a significant amount of acid sites upon hydro-thermal treatment compared to the powder zeolites. Furthermore, hierarchical porosity induced through steaming and inclusion of the binder may also play a role in the formation of larger oligomers. Characterisation results can then be correlated to what is observed here in order to determine how the enhanced stability affects the reactivity/product selectivity.

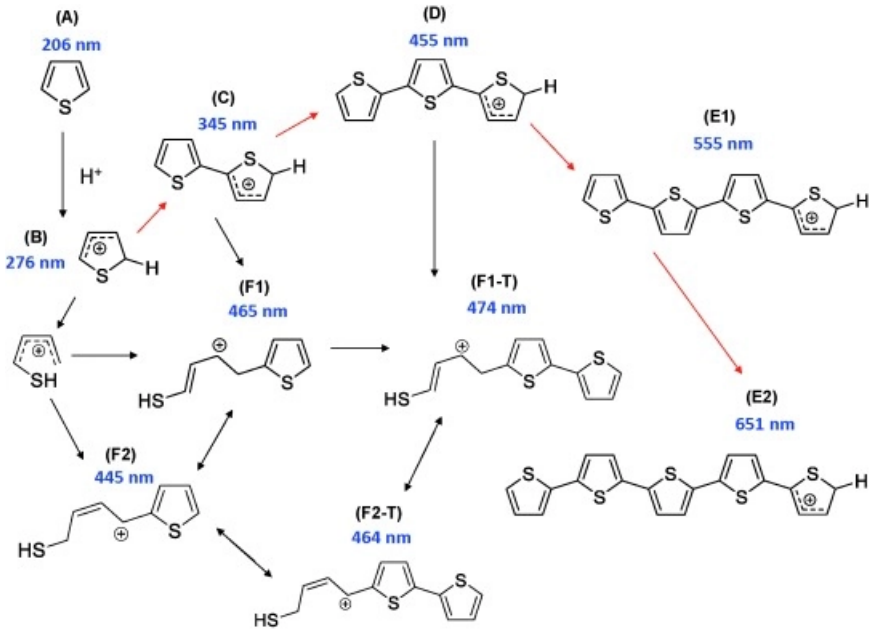

Figure 3.14: Proposed reaction pathway of thiophene oligomerisation on zeolite acid sites as determined from DFT. Reproduced from Whiting et al.[89] Two distinct pathways can be seen; oligomerisation (C/D/E1 etc.) and ring opening reactions (F1/F1-T etc.) Formation of these compounds depends on the Si/Al ratio, pore size etc. of the zeolite.[90]

The different compounds formed here are attributed to 2 distinct reaction pathways; oligomerisation and/or the ring opening reactions. The formation of these compounds depends on the Si/Al ratio, pore size etc. of the zeolite.[90] During the course of the reaction different thiophene carbocations are formed, which absorb at different wavelengths and indicate the existence of different reaction pathways (Figure 3.14). The Thiophene monomer (A) undergoes protonation on Brønsted acid sites to form the protonated monomer (B). After this two different reaction pathways are possible: the ring opening mechanism and subsequent reaction with the second monomer to form a thiol-like carbocation (F1/F1-T/F2/F2-T) or the dimerisation (C) resulting in further oligomerisation (D) which could follow the ring opening mechanism as well (F1/F1-T/F2/F2-T). (D) can undergo further oligomerisation to form more conjugated species (E1/E2), as well as even larger carbocations that were not theoretically determined.[88,89] These findings are of course for the free version of these compounds. As seen in the results here, the zeolite environment and protonation process will cause some of these bands to shift, which is necessary

for their formation and stability.[90]

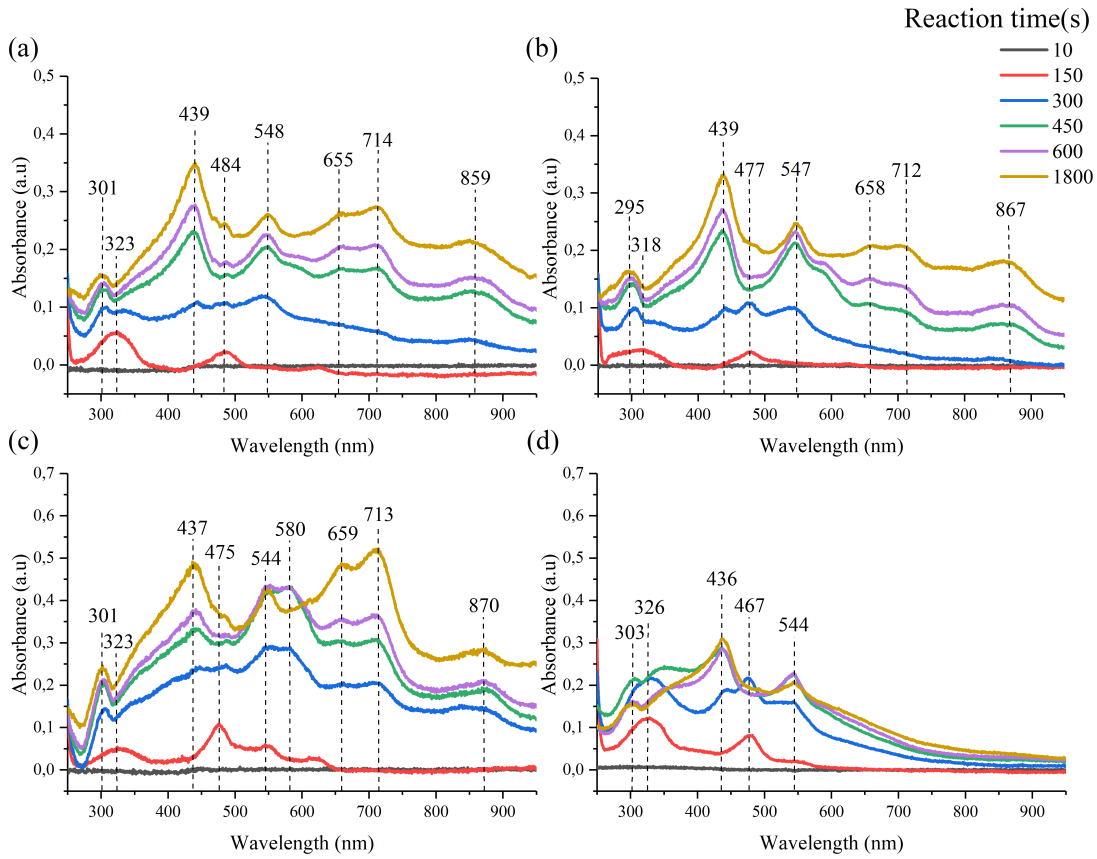

Figure 3.15: UV-Vis absorption spectra for (a) 117-500-parent, (b) 117-500-steamed, (c) 38-500-parent and (d) 38-500-steamed. Initial thiophene monomer region (∼206 nm) was intentionally left out for more clarity with the following absorption bands. 38-500-parent obtains a higher aborbance at ∼301 nm compared to the others, due to the large number of Brønsted acid sites available to protonate thiophene monomers.

In Figure 3.15 the time-resolved UV-Vis absorption spectra obtained from the powder samples are shown. All samples show absorption peaks that can be assigned to the different oligomers being formed. Looking at the high silica content samples first (Figure 3.15a-b), we can see the characteristic bands associated with the formation of the initial monomer compounds at 295-323 nm, with 117-500-parent showing a higher initial absorbance in this region at t = 150 s. At 300 s reaction time both samples show broad absorbances corresponding to the formation of several species; firstly, a trimeric carbocation (D) at 439 nm or ring opening pathway forming a thiol like species (F2), as well as further dimeric intermediates (F1-T) at 477-484

nm, then most likely converted to other conjugated ring opened species and finally the most defined peak at this reaction time corresponds to the E1 carbocation seen at 548-547 nm. Additionally, 117-500-parent also shows a broad absorbance beyond these wavelengths, indicating that even larger carbocations begin to form earlier in the parent sample. This trend continues into the higher reaction times with 117-500-parent showing more absorbance in the higher wavelengths. The absorbance band at 547 nm (E1) in 117-500-steamed shows only a minor change between t = 450-1800, as its being converted to E2 and higher carbocations. However, the tetrameric carbocation species seen at 548-547 nm as well as any larger oligomers are unlikely to fit inside the zeolite channels and are therefore most likely formed on the outer surface.[89]

The characterisation data indicated that 117-500-steamed had a slightly higher pore size distribution in the meso-pore range (Figure 3.3a) and a lower acid site density (Figure 3.9a). Coupled with the UV-Vis data seen here it is apparent that acid site density, not porosity is the dominant factor in the formation of the larger oligomers.

The high alumina content zeolite shows many of the same bands albeit at much higher absorbance. At t = 150 s a ring opened thiol-like carbocation (F1-T) has already begun to form, followed by a very broad absorbance band across all visible wavelengths at t = 300 s, owing to the large amount of Brønsted acid sites available for reaction. The rate of formation for species between 544-580 nm begins to slow as they are converted to larger oligomers (E2 and further) between 450-1800 s reaction time.

A large drop in intensity is observed upon steaming, consistent with the almost complete loss of Brønsted acidity. While retaining some peaks for the products formed at lower wavelengths, the larger conjugated species are non-existent. While bulk characterisation techniques such as NH_3-TPD (Figure 3.5) and CO IR (Figure 3.7) appear to show the complete loss of almost all Brønsted acidity, it is clear from the UV-Vis spectra that some amount of possibly weaker acid sites are still able to perform an oligomerisation reaction.

Since the larger oligomers were shown to form on the zeolite surface, we can assume that indeed the smaller carbocations being formed in 38-500-steamed are from acid sites within the zeolite framework. This is contrary to the characterisation data, where TPD was used to probe acid sites deep inside the zeolite framework, showed a very low acid site concentration. Therefore it is puzzling that thiophene, a larger molecule than NH_3 is able to find Brønsted acid sites to be protonated over.

The extrudate samples, seen in Figure 3.16 show very similar trends across all spectra. The parent samples (Figure 3.16a,c and e) show the same bands as 38-500-parent, albeit with lower intensity due to the 50:50 zeolite/binder ratio. The steamed samples indicate the presence of the same products in the lower wavelengths (295-544 nm) as the parent extrudates. However, the intensity of the bands in the 660-715 region, corresponding to higher order carbocations are noticeably lower in the steamed samples (Figure 3.16b,d and f). Furthermore, the sharp peak at 478-479 nm seen in all spectra between t= 150-300 which corresponds to a ring opened thiol-like carbocation decreases over further reaction time as other peaks corresponding to larger oligomerised products (D, E1, E2 etc.) This is especially noticeable in the steamed samples and indicates competing reaction pathways. From what is seen in these spectra it appears the weak acid sites catalyse the ring opening pathway while the stronger acid sites form larger oligomers. Pyridine IR (Table 3.2) showed that the ratio of BAS:LAS decreased significantly upon steaming, where most of the Lewis acidity arises from the binder. Assuming the alumina binders do not take part in the reaction,[89] other mildly acidic extra-porous species such as those discussed in the earlier 'de-alumination kinetics' section could also be reacting the thiophene.

Comparing the the parent extrudates to 38-500-parent several noticeable differences can be observed. Firstly, the formation of the ring opened thiol like species (F1-T) at ∼474 nm yields a sharper absorbance band in the parent extrudates. As we saw with the steamed extrudates the intensity of this band is proportional to the decrease of the larger oligomer peaks seen at 651 nm and beyond. With this in mind it appears thiophene in the parent extrudates is also being catalysed by similar molecules. It is possible the extrusion/calcination process leads to the formation

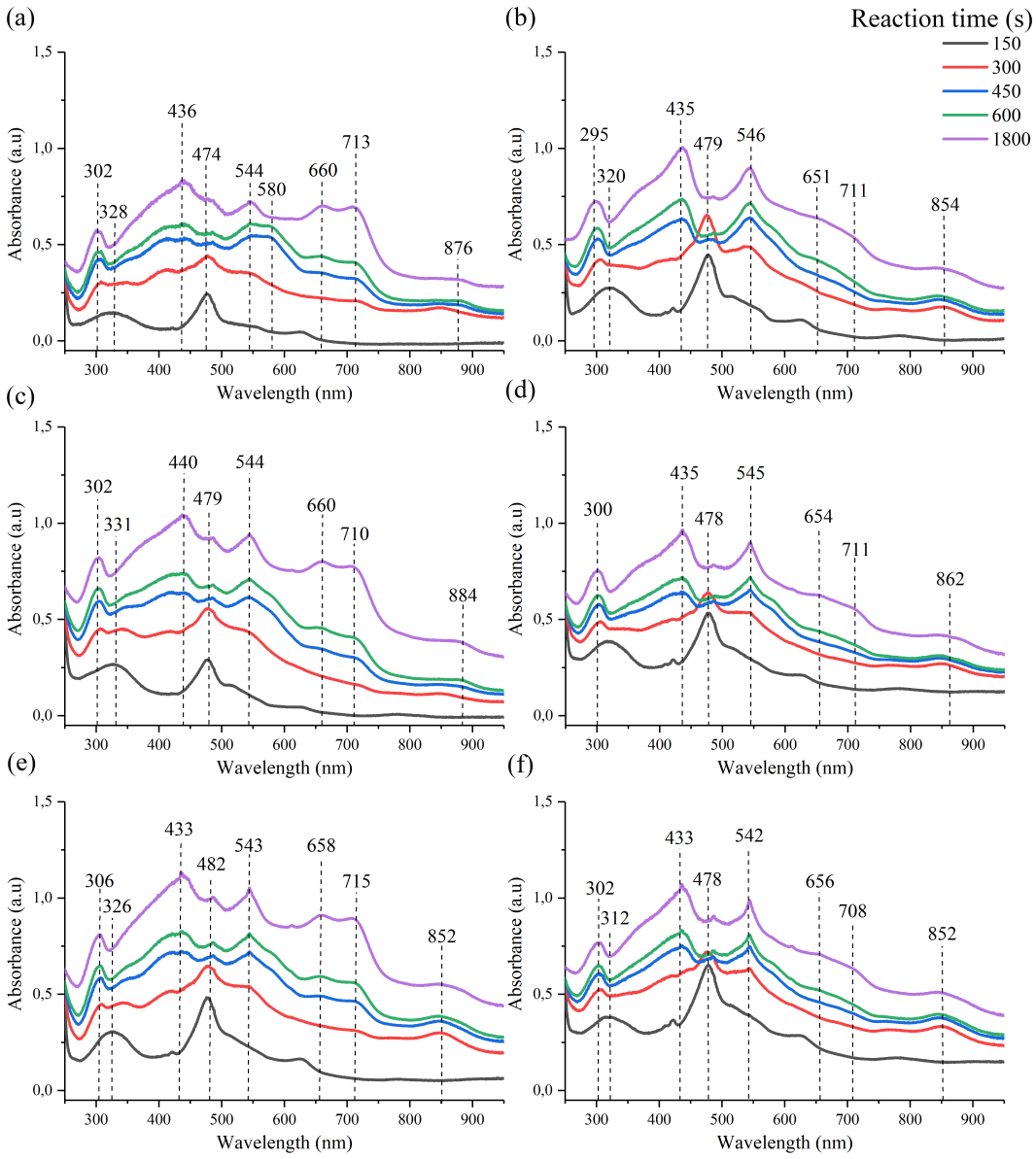

Figure 3.16: UV-Vis absorption spectra for (a) CATD-parent, (b) CATD-steamed, (c) TM70-parent, (d) TM70-steamed, (e) TH100-parent and (f) TH100-steamed. The parent samples show the same bands as 38-500-parent, with lower intensity due to the 50:50 zeolite/binder ratio. Larger oligomers are not formed in the steamed extrudate samples, excluding effects due to pore blocking it appears acid site density determines the formation of oligomers in the higher wavelength regions.

of acidic Al_{EF} or a certain degree of de-alumination, both of which occur to a lesser degree in 38-500-parent. Powder zeolite 38-500-parent also shows a higher ratio of bands corresponding to oligomerised species compared to the ring opened.

Indeed, it appears the higher density and strength of the BAS in the powder zeolite favours the oligomerisation pathway. In the parent extrudates, the formation of these large oligomers on the zeolite surface (due to their size) indicate that the inter-particle porosity caused by the binder in terms of affinity towards larger products is largely negligible in this case. The density of surface acid sites determines their formation. This is of particular interest in the comparison of the steamed powders and extrudates where 38-500-steamed produces no large oligomers.

The steamed extrudates show broad bands in the higher wavelengths. The presence of these bands indicates that strong surface acid sites (and perhaps Al_{EF}) are still prevalent after hydro-thermal treatment of the catalyst bodies. Whiting *et al.* conducted the thiophene oligomerisation reaction on several extrudates bound by silica, alumina etc. Results suggested that the alumina-bound pellets induced additional acid sites of a different strength to what was expected, which favoured the ring opening pathway. It was proposed this effect was caused by the apparent "re-aluminaion" process.[89] As discussed in the 'de-alumination kinetics' section, "re-alumination" effects caused the extrudate to maintain significantly more (surface) acid sites after hydro-thermal treatment compared to the powder zeolite. While the acid sites in the steamed extrudates are not completely retained, compared to their parent counterparts, a noticeable percentage of these sites are still able to react in the oligomerisation of thiophene.

In conclusion, the oligomerisation of thiophene as a model catalytic reaction has been beneficial in understanding the reactivity and selectivity of these materials. However, in order to properly test these catalysts, a more complex reaction with a more defined product distribution and ability to monitor deactivation is needed.

3.2 Catalytic Testing

The zeolite powder and extrudate samples were tested in the MTO reaction, with the aim of assessing the influence that hydro-thermal treatment has on the catalytic

activity. Helium was flown through a methanol saturator into the reactor containing the catalyst, forming products that were then measured using an online GC while *operando* UV-Vis spectroscopy was used to monitor the coke formation. The resulting GC chromatograms were then used to calculate the yields of different products and the methanol conversion.

MTO data for the powder zeolite samples can be seen in Figure 3.17. Notable differences in yields can be seen for ethylene, where 38-500-parent shows a much higher yield compared to 117-500-parent/steamed. Since ethylene and aromatics are considered to be the main products of the aromatic cycle, it is evident this reaction pathway is participating the most in this case.[91,92] This observation is supported by the results in Figure 3.17d, as paraffins are also formed through hydrogen transfer reactions, so an increase in this product is indicative of the aromatic cycle.[93] Furthermore, the high SAR zeolites 117-500-parent/steamed show a lower yield of both ethylene and paraffins. Clearly, condensation reactions are more likely to take place with higher BAS density zeolites and a strong interaction with coke precursors.[94] To elaborate further; the close proximity of the BAS in 38-500-parent means more reactions can occur on these sites in succession. Therefore, there is a greater chance the initial reactants will form aromatics or coke species, thus favouring the aromatic cycle and resulting in a higher yield of ethylene.[94]

Alternatively, the lower acid site density zeolites show a much higher yield of propylene, in particular the dealuminated 117-500-steamed sample (Figure 3.17b). Unlike the acid site dense zeolites, the isolation of BAS in this case favours methylation and cracking reactions, with less consecutive reactions taking place and therefore possibly less aromatization/coking. From these results it appears BAS density is the main factor governing the direction of the various hydrocarbon pool mechanisms, as the clear differences in yields for ethylene and propylene indicate that these two products are formed via competing routes. Ethylene is mostly formed via xylenes and tri-methylbenzenes as opposed to cracking reactions like other olefins.[62]

Finally, in terms of conversion (Figure 3.17f), it can be observed that the par-

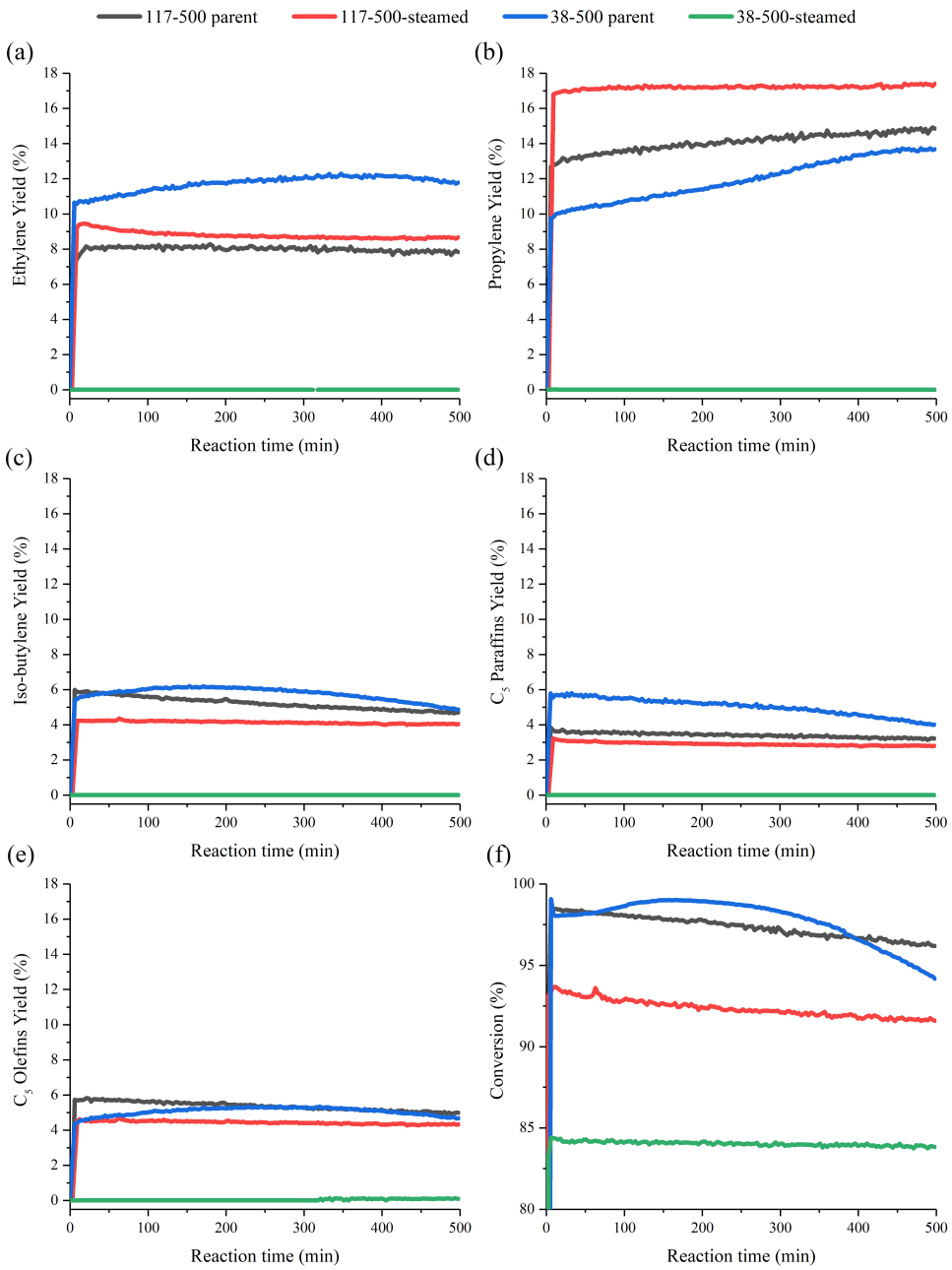

Figure 3.17: MTO data for all powder samples showing yield for (a) ethylene, (b) propylene, (c) iso-butylene, (d) C_5 paraffins, (e) C_5 olefins and (f) conversion. Higher BAS density in 38-500-parent causes shift to aromatic cycle and hence higher selectivity to ethylene while low BAS density in 117-500-steamed shifts selectivity towards propylene which is formed through the alkene cycle. Graphs with error bars plotted can be seen in Appendix Figure 15.

ent ZSM-5 samples 117-500 and 38-500 showed almost complete methanol conversion at the start of the reaction, while their hydro-thermally treated counterparts

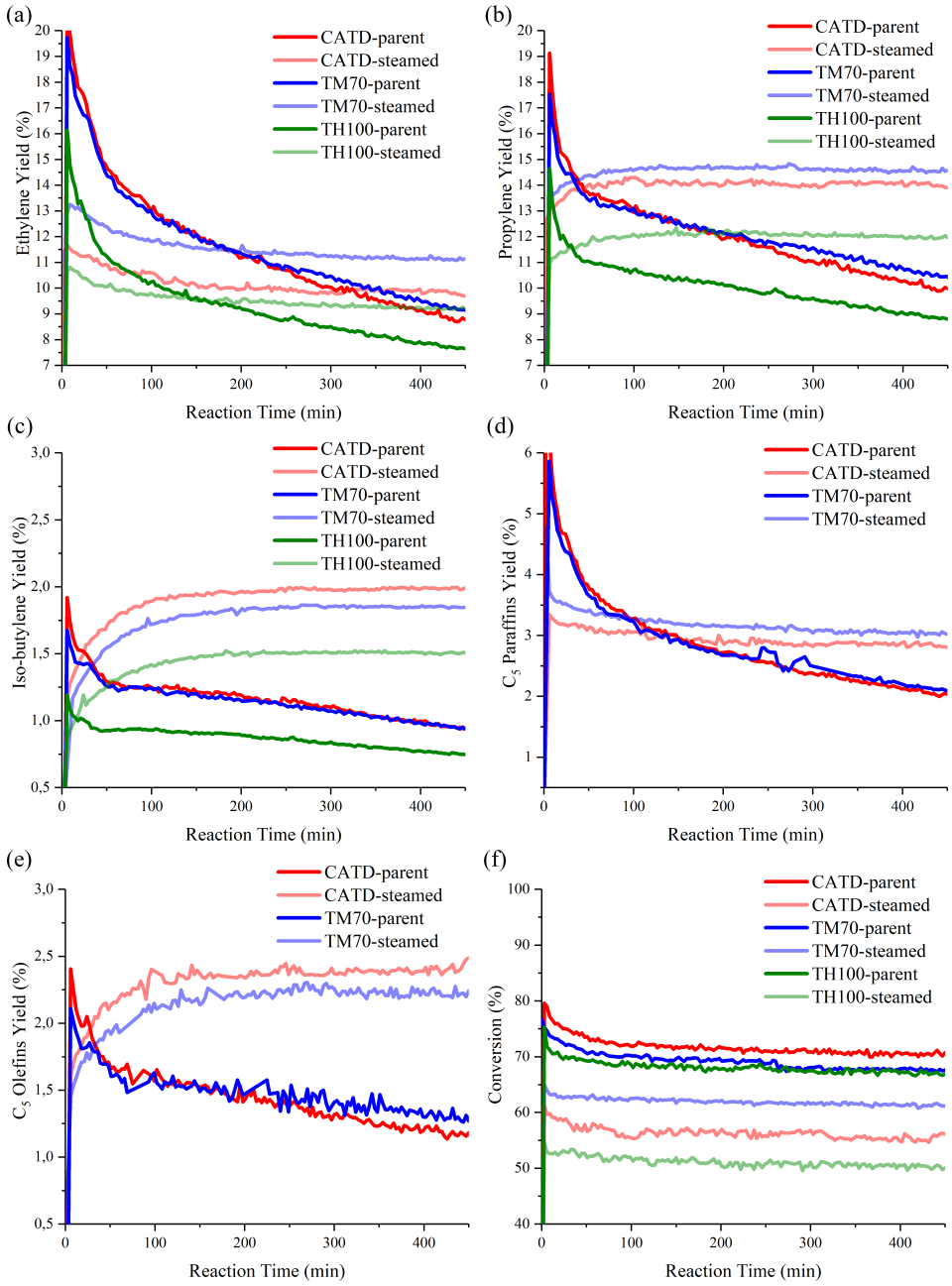

Figure 3.18: MTO data for all extrudate samples showing yield for (a) ethylene, (b) propylene, (c) iso-butylene (d) C_5 paraffins, (e) C_5 olefins and (f) conversion. Yields were normalised to zeolite content. C_5 paraffins/olefins yields for TH100 were not plotted due to quality of the results. Change in type of binder causes noticeable differences in results, however the reason for this effect could not be identified. Graphs with error bars plotted can be seen in Appendix Figure 16.

recorded slightly lower conversions, in particular 38-500-steamed which showed an initial methanol conversion of ∼84%. Goetze *et al* defines a catalyst as deactivated once the conversion is lower than 80%.[58] All catalyts are therefore still active after 8 h under stream, although it is clear 38-500-steamed is not producing the desired products and is instead forming methane, CO_2 etc. The initial activities correspond quite well to the acid site densities, being lower in the steamed samples and higher in parent. The trends in conversion are very similar but 38-500-parent shows a rapid deactivation after 6 h under stream. It appears catalyst lifetime is largely determined by Brønsted acidity, where consecutive reactions on the BAS dense surface results in a higher change of aromatic coke species being formed.[94] Decrease in acid site density causes a lowering of coke formation, however in the case of 117-500-parent/steamed the deactivation occurs at the same rate, where it appears the catalyst still deactivates with simply less coke being needed.

MTO results for the extudates can be seen in Figure 3.18. Overall, compared to the powder zeolite (38-500-parent) we see a significantly higher yield of ethylene, for all extrudate samples. A very high initial yield of ethylene is observed in the first 2 hours, followed by a rapid decrease, which is contrary to the trend seen for 38-500-parent, where a gradual increase in yield was observed. The high BAS density likely favours the aromatic cycle (at least initially) resulting in a higher selectivity to ethylene, however the close proximity of the acid sites coupled with better accessibility as a result of the binder could also cause more poly-aromatic coke species to form, accounting for the loss of ethylene yield. The steamed extrudates show a lower initial yield but remain relatively stable throughout the reaction period. As with the powder zeolites, the isolation of the BAS means there is less chance the initial reactants will form aromatics, resulting in a lower yield of aromatic cycle products. TH100-parent shows a noticeably lower yield compared to the other products; it may be that the lower surface area (Appendix Table 1) results in less molecular transport of the products out of the extrudate, with the meso-pores formed through de-alumination mitigating this effect in TH100-steamed.

The parent extrudate yields for propylene and iso-butylene show a similar trend to

ethylene, indicating the aromatic and alkene cycles are participating to an equal degree. Upon de-alumination however, yields of both products increase. Here it is evident from the different trends compared to ethylene, that selectivity has switched more towards the alkene cycle. In the case of propylene the yield is greater than the powder zeolite (Figure 3.17b). The lowering of acid site density through de-alumination caused an increase in propylene yield for the powder samples (117-500-steamed), due to the isolation of BAS. This effect is magnified in the steamed extrudates and coupled with the higher accessibility to the active sites results in higher yields. Iso-butylene, the formation of which also follows the alkene cycle, shows a similar trend to the propylene results but has a lower yield overall compared to the results from the powder zeolite samples.

So far the analysis of the product selectivity has focused on Brønsted acidity, but as seen in the characterisation data (Figure 3.2) the extrudate samples contain a large concentration of Lewis acid sites, arising from the binder and extra-framework species. While the role of Lewis acidity is often overlooked in the analysis of MTO, any effects due to such a large concentration of LAS cannot be ignored. Muller *et al.* investigated the role of LAS in hydrogen transfer pathways in the methanol-to-hydrocarbons conversion. Results showed that methanol and propylene react over LAS via hydrogen transfer reactions producing paraffins and formaldehyde. Olefins then react with formaldehyde over BAS to produce aromatics, with a high tendency to oligomerise into graphitic coke molecules.[93] However, taking into the account the scope of this project it is difficult to identify the role LAS play in the reactions presented here, as the main focus was altering Brønsted acid sites through de-alumination. Further studies isolating the various Lewis acid type species will need to be conducted to properly determine how LAS concentration affects the selectivity and activity of the MTO process, such as catalytically testing the binders and zeolite free extrudates (silicalite/alumina).

The general conversion of all the extrudates are noticeably lower than the powders, mainly due to the 50:50 zeolite/binder content. Steamed extrudates, much like the powders, exhibit a lower conversion compared to the parent, this is not surprising,

as the activity is lowered due to de-alumination. However, a change in the type of binders used also seems to affect the conversion results to a noticeable extent. These results are proportional to the pyridine IR measurements (Table 3.2), and therefore can be correlated mainly to the general loss of acidity through hydrothermal treatment and not a loss molecular transport due to coking. However, in order to properly understand the mechanism of catalyst deactivation it is necessary to monitor the formation of the related poly-aromatic species that cause this.

3.2.1 *Operando* UV-Vis Spectroscopy

One method to investigate deactivation is through monitoring the catalyst with spectroscopic methods under reaction conditions. In this instance, *operando* UV-Vis spectroscopy allows us to detect hydrocarbons with conjugated double bonds and unsaturated carbocations.[69] Therefore, it is possible to monitor the formation of cyclic and poly-aromatic coke species as the reaction progresses. These results can then be correlated to the GC data regarding conversion/deactivation.

The mechanism of coke formation begins with the formation of benzene and its methyl substituted carbocations. With further addition of methanol, these compounds evolve further into mainly linear poly-aromatic coke species located in the zeolite channels. They are mainly limited to pyrene-like structures due to the spatial restrictions of the zeolite channels. The further addition of reactants as the reaction progresses causes these compounds to grow towards the outer surface of the zeolite where the absence of molecular size restrictions mean larger graphitic coke species are able to form (coronene etc.).[12] The formation of these products influence the selectivity/activity of the reaction through side reactions and/or inhibiting diffusion of reactants.

Operando UV-Vis absorption spectra of the powder zeolite catalysts are presented in Figure 3.19. All spectra show the initial absorbance band for benzene between 284-298 nm. The intensity of this band decreases with time on stream as benzene

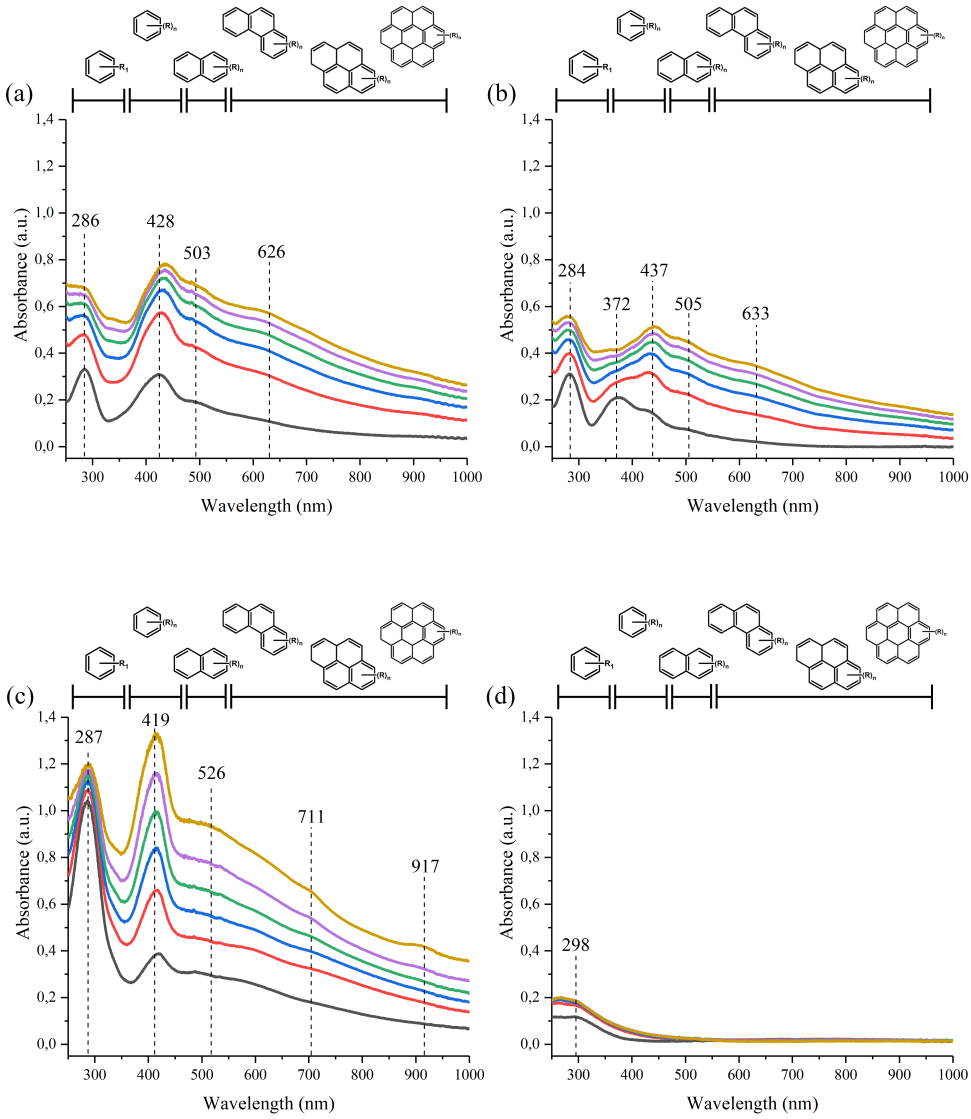

Figure 3.19: UV-Vis absorption spectra for MTO powder zeolite samples (a) 117-500-parent, (b) 117-500-steamed, (c) 38-500-parent and (d) 38-500-steamed. Spectral positions of poly-aromatic species was based on Konnov *et al.*[95] Spectra are plotted for 10, 50, 100, 150, 200 and 250 minutes reaction time in ascending order.

reacts further to form other compounds. As the reaction progresses benzene is converted to methyl-substituted benzenium cations at 419-437 nm (Figure 3.19a-c), which are said to constitute the catalytic scaffold of the hydrocarbon pool (HCP) mechanism.[12] Upon further addition of methanol an additional absorption band forms at 503-505 nm, appearing slightly red shifted towards 526 nm for 38-500-parent. Corresponding to naphthalene and its derivatives the formation of this

band over time is more pronounced with increasing BAS density. Beyond 600 nm, where absorption bands correspond to coke species formed at the outer surface of the zeolite, broad absorption bands related to the formation of phenanthrene/pyrene type molecules can be seen. The absorption in this region is less distinctive for 117-500-steamed, indicating that despite a slightly higher distribution of meso-pores (Figure 3.3), the BAS dense parent samples produce more of the large conjugated coke species. This is evident by an absorption band at 917 nm, corresponding to coronene type species for 38-500-parent (highest BAS density as seen in pyridine FTIR Figure 3.2).

Mores *et al.* studied the coke formation in large ZSM-5 crystals during the MTO conversion using UV-Vis and CFM. Results showed that higher aluminium content in the zeolite facilitated the formation of larger coke species, consistent with the results obtained in this study. Their findings also indicated that changing the Si/Al ratio did not result in different coke species being formed, rather a change in the same absorption band's intensity or position.[12] Contrary to this, 117-500-steamed displays an initial absorption band at 372 nm, which is absent from the other spectra. Upon starting the reaction benzene and its methylated derivatives (possibly toluene, p-xylene etc.) have already formed. It is possible that because the density of BAS is lower, the distance between individual acid sites increases, resulting in a lower conversion towards more conjugated coke species, in the initial reaction steps.

These results can be correlated to the selectivity data, where the BAS dense 38-500-parent showed a much higher ethylene selectivity, which mostly formed via xylenes and tri-methylbenzenes as part of the aromatic cycle. We can therefore assign the band at 419 nm to the formation of these compounds. 177-500-parent, has a broad shoulder peak in this region, corresponding to a lower selectivity towards aromatics formation while 117-500-steamed forms different products, as the lower acid site density results in higher participation of the cracking reactions through the alkene cycle and therefore less poly-aromatic coke formation.[62]

Operando UV-Vis absorption spectra of the zeolite extrudate catalysts are presented

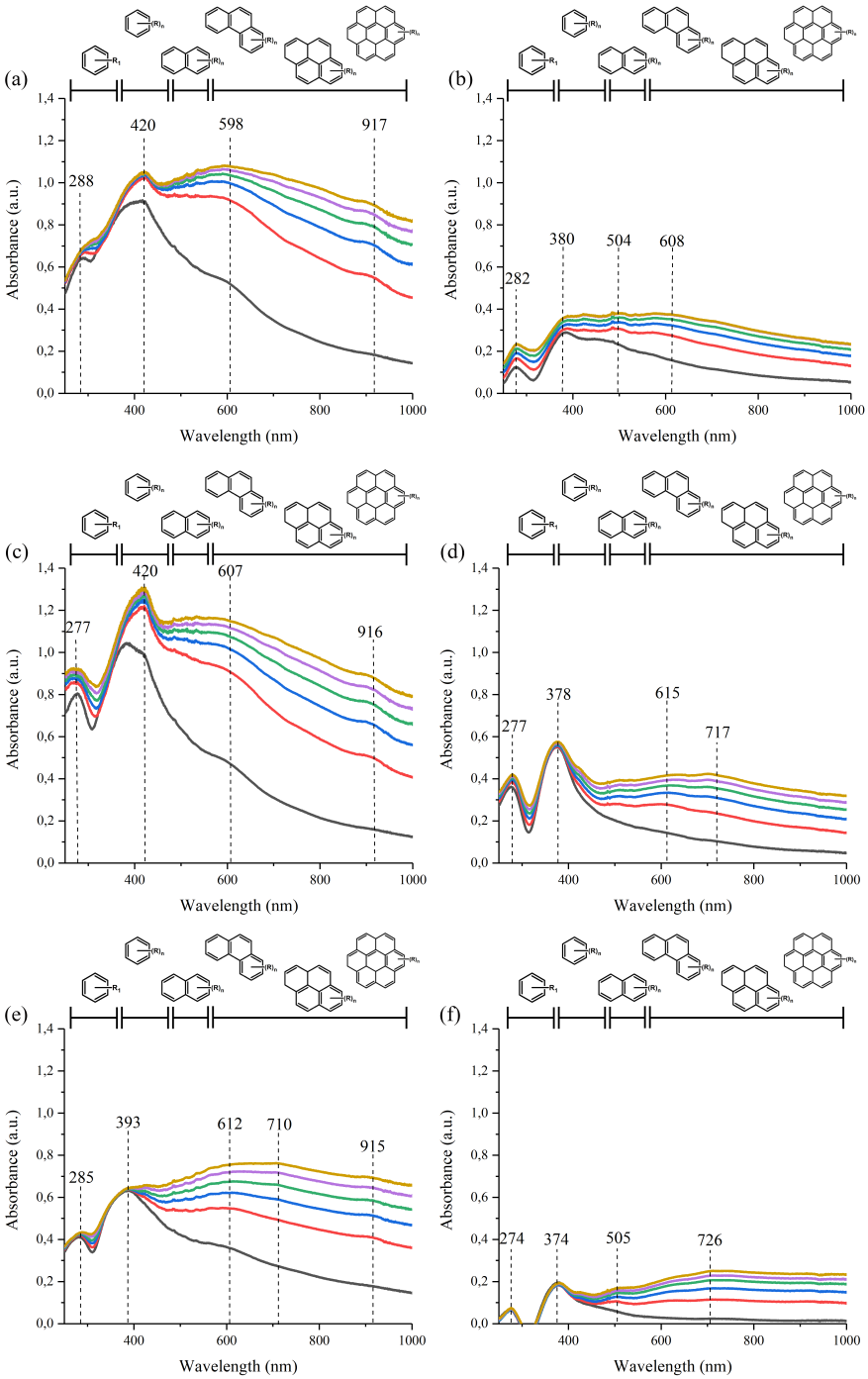

Figure 3.20: UV-Vis absorption spectra for MTO extrudate samples (a) CATD-parent, (b) CATD-steamed, (c) TM70-parent, (d) TM70-steamed, (e) TH100-parent and (f) TH100-steamed. Spectra are plotted for 10, 50, 100, 150, 200 and 250 minutes reaction time in ascending order. Spectral positions of poly-aromatic species was based on Konnov *et al.*[95]

in Figure 3.20. As with the powder zeolite, an initial absorbance band for benzene is observed at 274-288 nm in all spectra. Similarly, CATD/TM70-parent show an absorbance for methyl substituted benzinium cations at 420 nm.[12] Interestingly, this peak is absent in TH100-parent, where only a broad peak at 393 nm is seen in this region. This absorbance is seen slightly blue shifted in all the steamed extrudate samples and appears as a shoulder peak in CATD/TM70-parent as well as in 117-500-steamed, where the lower acid site density most likely caused the formation of this alternative coke compound. Therefore, we can assume this peak arises due to lower BAS density caused by the zeolite:binder ratio in the parent extrudates as well as de-alumination in the steamed extrudate samples.

Broad absorbances for larger coke molecules (pyrene,phenanthrene, coronene etc.) are seen in all parent extrudate samples. For the powder zeolites we established that the higher BAS density (towards the zeolite surface) was the main factor in forming graphitic coke molecules such as coronene etc. In the extrudates however, it appears the extra-degree of porosity brought on by the binder and inter-particle spacing has led to an increase in more conjugated coke species. Clearly, above a certain degree of porosity the reduction in acid site density becomes negligible, although said acid sites may be more accessible to coke species in extrudates. However, the steamed extrudates show a much lower absorbance in the higher wavelengths, where a decrease in BAS density occurs but no major change in meso/macro porosity is seen. Therefore, it appears the formation of larger more conjugated coke species is dependent on a balance of acid site density and porosity, at least in zeolite extrudates.

In summary, the effect of de-alumination through hydrothermal treatment on the acidic properties of zeolite powders and extrudates was studied using a combination of physical and chemical characterisation techniques, where results showed zeolite extrudates were more resistant to de-alumination compared to the powder. This phenomenon was most likely due to the "re-alumination" effect, where Al atoms migrate back into the zeolite framework via extra-porous aluminium species. Catalytic testing in the MTO reaction showed that steamed extrudates had the highest selectivity towards propylene and lower formation of coke species.

4 Inducing Further Macro-porosity in Zeolite Technical Bodies and its Effect on Catalytic Activity

Crucial to this section on porosity is the use of porogens, also known as pore forming agents, which induce further macro-porosity into the alumina binder-bound zeolite extrudates. The use of porogens for industrial applications is known, however their effects on the performance of catalyst bodies has, as far we know, not been attempted in academia.[13,54] While literature on the use of porogens in catalysis is scare, several patents and research papers on their use in the ceramics industry exist.[50,51] Using these as a benchmark, wheat (10/30 wt%) and rice (30 wt%) starch were used as pore inducing templates in the synthesis of extrudates. The reason for inducing such porosity is to create so called 'molecular highways' where reactant molecules diffusing through the catalyst have greater access to active sites as well as exiting the catalyst after being converted.[96]

Until recently the main method towards determining the porosity of catalytic materials has involved non-visual bulk measurements using probe molecules, such as Ar-physisorption and Hg-porosimetry. While these measurements do supply useful information they often times do not represent the true inter-connectivity within a catalyst. The molecular dimensions of these probes (Ar, Hg) cannot be related to the size of catalytic species formed in the reaction and are therefore not a proper representation of the accessibility such catalytic molecules would experience in a reaction. Scanning electron microscopy (SEM) can be correlated to visualise general

pore size, but is largely impractical for the purpose of visualising pore architecture.[66] Using specifically sized fluorescent probes, a facile and direct method to visualise accessibility within catalyst bodies was developed by Whiting *et al.* and is presented here.[66] These results will then be correlated to the catalytic data from the MTO process to provide a proof of principle into the effects of how porogens influence the physio-chemical catalytic properties of extrudates.

4.1 Characterisation

4.1.1 X-ray Diffraction

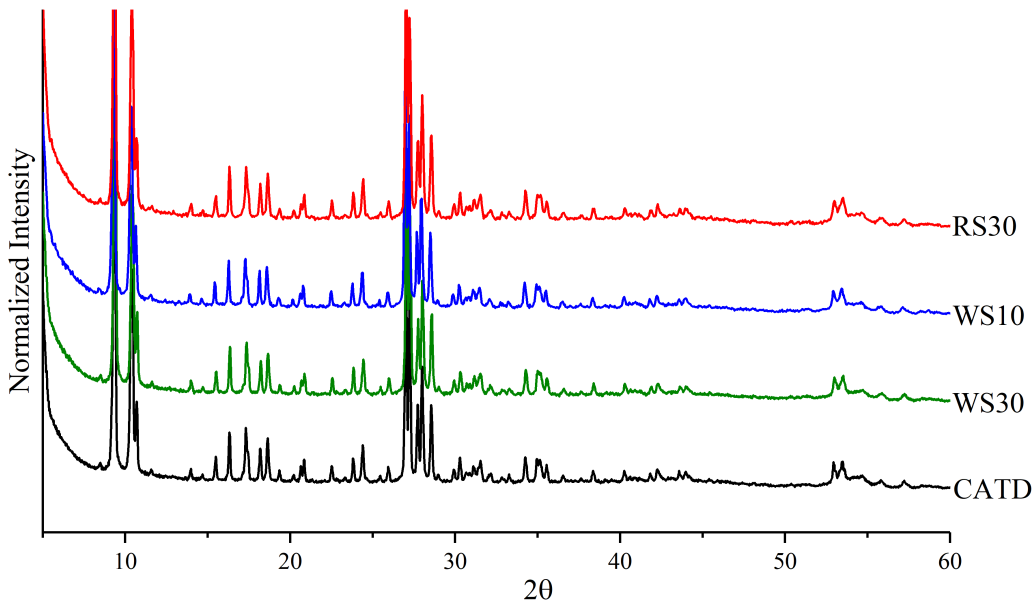

Figure 4.1: X-Ray Diffraction patterns for the wheat starch (WS10/30) and rice starch (RS30) induced porogens with CATD extrudate for comparison. As can be seen, no major change in crystalline order can be observed with the use of porogens, even at 30 wt%.

As with the powder and extrudate samples, XRD is used to probe the long range atomic structure and determine to what extent the crystallinity is affected by the use of porogens. The results are summarised in Figure 4.1, where RS30 and WS10/30 correspond to the rice starch (30 wt%) and wheat starch (10/30 wt%) porogens

respectively, after calcination. Peaks arising from the CATAPAL D binder can be seen at $2\theta = 17$ and 34 (Appendix Figure 13). As expected, compared to the standard extrudate sample (CATD) no noticeable change in the crystal structure is seen upon the use of porogens, even at higher weight loadings.

4.1.2 Mercury Porosimetry

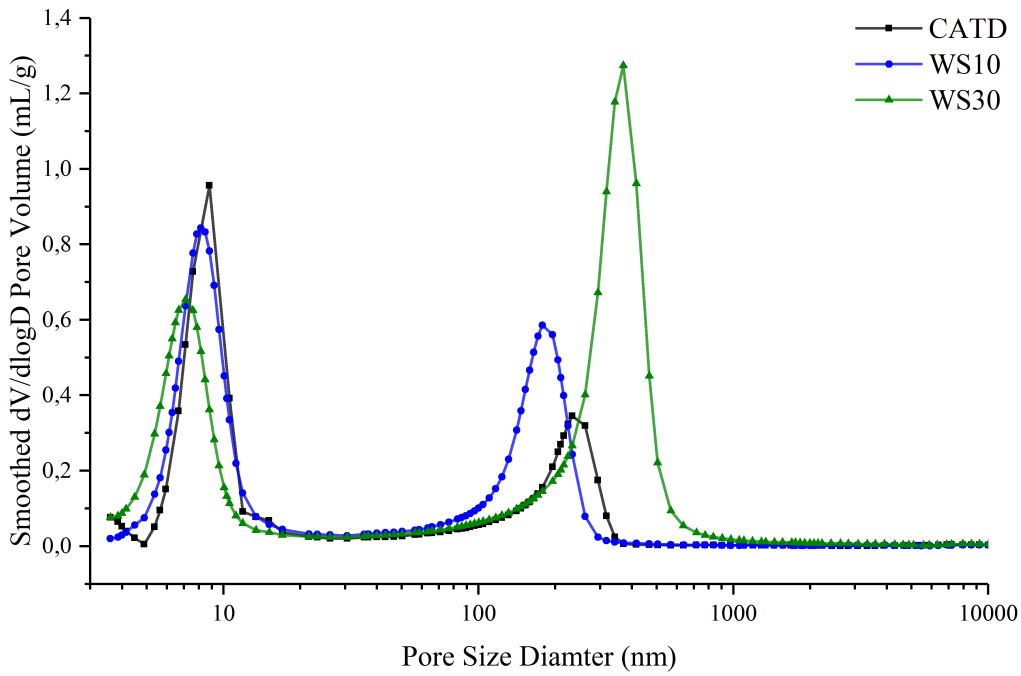

Figure 4.2: Hg porosimetry measurements. Meso-pores arising from the binder are seen in all samples. Macro-pores in the parent CATD sample can be attributed to inter-particle spacing, with a larger distribution in this region from the porogen-based samples WS10/30.

Mercury porosimetry has been used as a complementary technique to physisorption in order to probe the dimensional properties of zeolites.[97] Hg-porosimetry is excellent for probing the macro-pore range but is unable to enter pores < 3 nm due to the lower accessibility of mercury into the entire pore structure, caused by the limited maximum pressure that can be achieved.[98] As was apparent from the pore size distributions of the extrudate samples (Figure 3.4), a very large distribution of meso-pores was observed, due to the use of a binder. However, Ar/N_2 physisorption is unable to probe the macro-pore range, where the cavities created through these

pore forming agents are found.

The results for Hg-porosimetry are summarised in Figure 4.2. The initial peaks seen at a pore size distribution of 8-10 nm can be attributed mainly to the porous alumina binder, which is consistent with the Ar physisorption data for the parent extrudate (CATD) seen in Figure 3.4a. An increase in wt% of porogen results in a lower pore volume in this size region, as the binder content per gram becomes incrementally lower. In addition to this size range all samples show a pore size distribution in the macro-pore range (>50 nm). The trend in pore volume is the reverse of that seen in the meso-pore range where the porogen samples show the higher macro-pore volume. The macro-pores present in the parent CATD sample can be attributed to the interparticle spacing between the zeolite and binder particles.[98] These results are in line with those observed for zeolite extrudates with inter-particle spacing of similar dimensions.[66,98] Clearly, the porogen induces a higher level of porosity in a larger macro-pore range as well as the inter-particle spacing range seen in the parent extrudate.

4.1.3 Focused-ion Beam/Energy Dispersive Scanning Electron Microscopy (FIB-SEM, SEM-EDX)

Scanning Electron Microscopy (SEM) was used in order to better visualise how the porogen interacts in the catalyst body when introduced, and upon expulsion. Figure 4.3 shows the surface of the bi-sectioned extrudates at different magnifications and voltages. The surface of CATD shows a very uniform distribution of zeolite/binder, while in the un-calcined porogen sample (Figure 4.3b) the pore forming spherical wheat particles can easily be identified. The distribution of these "egg-shaped" particles appears to be uniform with their dimensions in line with those expected from the literature wheat starch particle size ($\sim$ 20 μm).[99] After calcination, a "shell" is leftover, which then collapses upon bi-sectioning, the nature of which appears to arise from the binder.

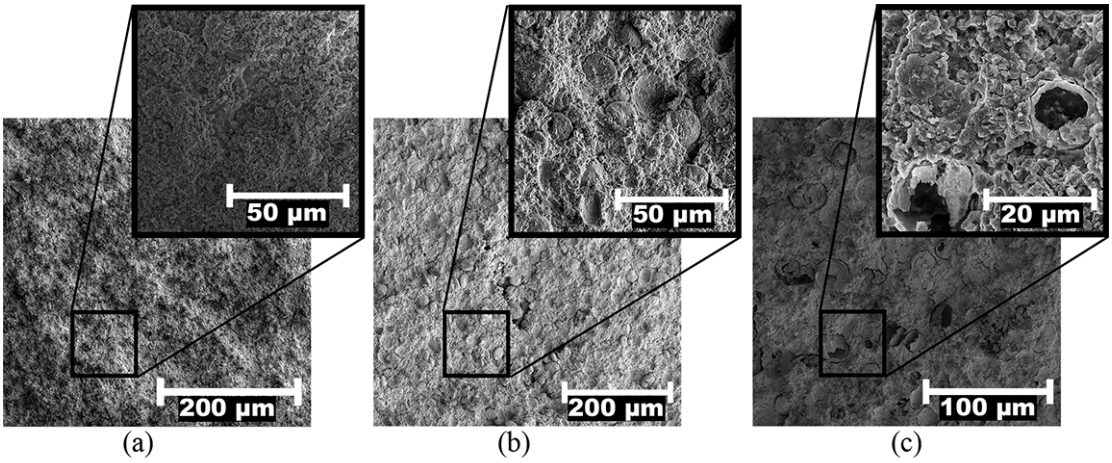

Figure 4.3: SEM of the bisectioned surfaces for (a) CATD calcined, (b) WS30 un-calcined and (c) WS30 calcined. Lower magnification images were carried out at 2 kV while the higher magnification was done at 10 kV. Spherical porogen particles can clearly be seen in WS30 un-calcined, these then leave an "shell" cavities upon calcination.

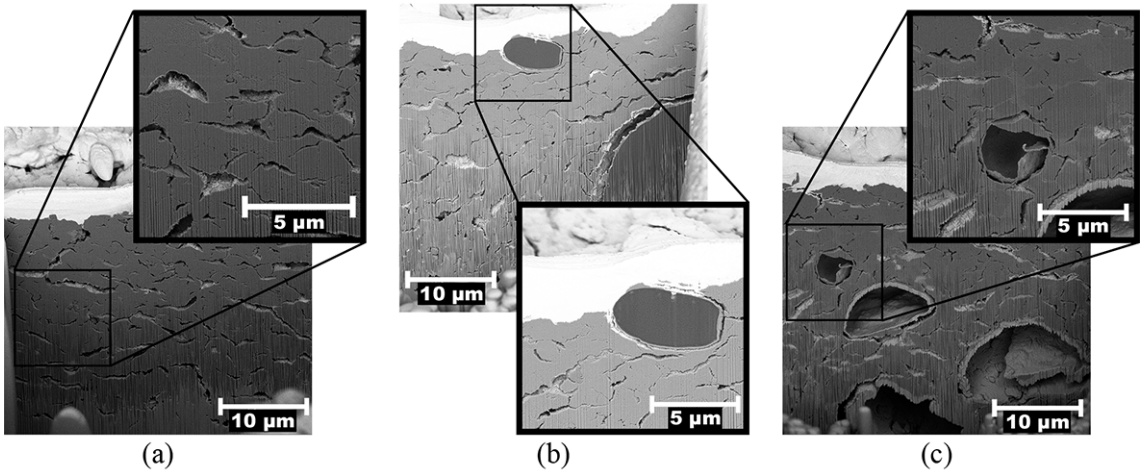

Figure 4.4: FIB-SEM images of the trench milled into the surface for (a) CATD calcined, (b) WS30 un-calcined and (c) WS30 calcined. Changes in colour correspond to back-scattering from compounds with different molecular weight.

Further FIB-SEM images of the trench created through milling with the Ga beam can be seen in Figure 4.4. The very close-packed distribution of the binder and zeolite can be seen in all samples, which can be better visualised in the the SEM-EDX images (Figure 4.5). In Figure 4.4b the pore forming wheat particle can clearly be seen as can the residual "shell" in the calcined WS30 sample (Figure 4.4c).

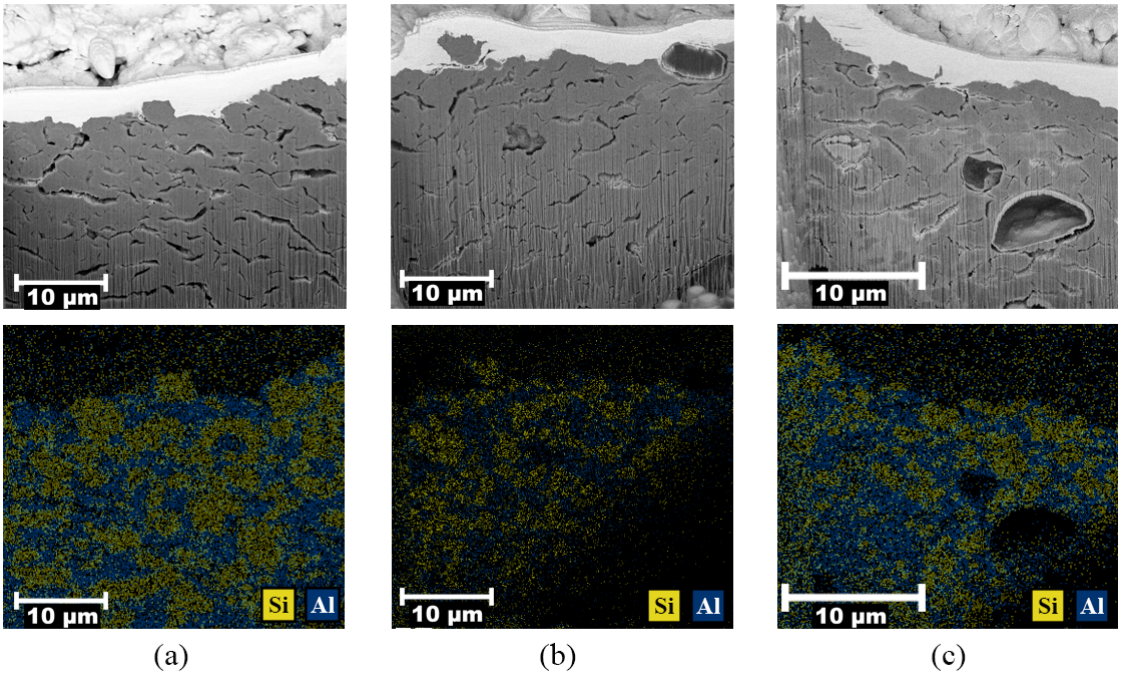

Figure 4.5: SEM-EDX measurements showing distribution of Si and Al for (a) CATD calcined, (b) WS30 un-calcined and (c) WS30 calcined. Top and bottom rows correspond to electron image and EDX map respectively. Al distribution can mainly be linked to the binder with Si corresponding to location of the zeolite particles, showing an even distribution of zeolite/binder.

In order to conclusively find out the composition of the leftover "shell" seen in the calcined images, SEM-EDX was performed, mapping the distribution of silicon, aluminium, galium and carbon. Firstly, the distribution of zeolite and binder, which correspond to the location of Si and Al respectively are uniform throughout all samples, with no changes being induced with the inclusion of a porogen (Figure 4.5). Finally, to determine the nature of the "shell" seen upon calcination, images at high magnification were mapped using EDX and are seen in Figure 4.6. In the un-calcined sample a clear Al ring (blue) around the porogen (red) can be seen in Figure 4.6a. Upon calcination this ring/shell is left over and collapses once the trench is cut into the surface, showing a void in the carbon image and a clear blue ring around it's edges.

Thus it can be concluded that the "shell" phenomena is residual alumina binder

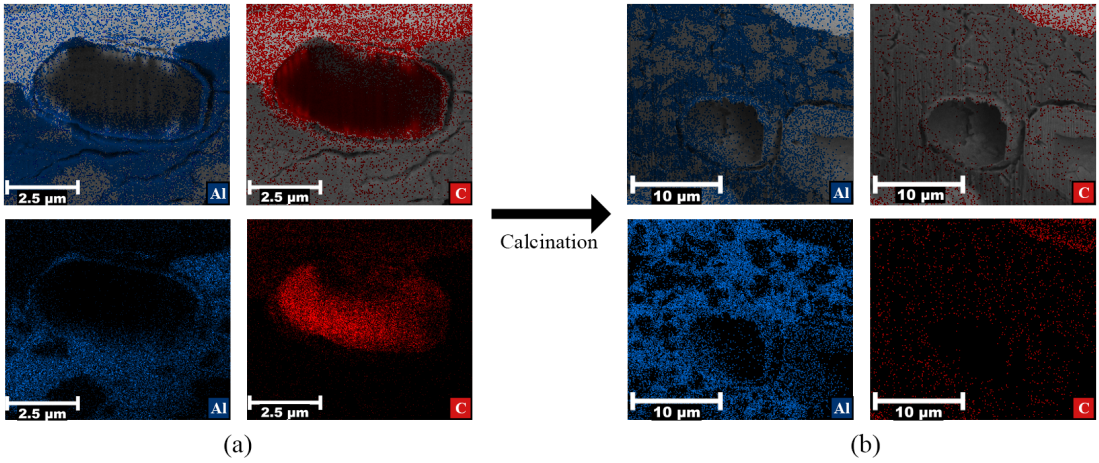

Figure 4.6: SEM-EDX measurements showing distribution of Al and C for (a) WS30 un-calcined and (b) WS30 calcined. Top row includes electron image, while being omitted from the lower row for clarity. Background carbon seen on the top is mainly due to contamination. Images show that leftover "shell" is alumina binder that encases the porogen during synthesis and then forms a cavity which collapses upon milling.

which encased the pore forming agent. This effect may also account for the pore size distribution seen in the Hg-porosimetry measurements (Figure 4.2), where once the porogen has been burnt off the binder moves in to enclose the cavity. A macro-porous cage, in the same size range as inter-particle spacing is left behind, with the inter-connecting channels from the binder surrounding it (Appendix Figure 10).

4.2 Fluorescent Imaging to Visualise Pore Architecture and Catalytic Activity

4.2.1 Visualising Accessibility of the Catalyst with Fluorescent Nano-probes

Confocal Fluorescence Microscopy (CFM) was used to image the diffusion of 5, 20 and 100 nm probes through the zeolite catalyst bodies, so as to grasp how accessible the pore architectures are of each extrudate. The 5 nm probe was N,N'-Bis(1-

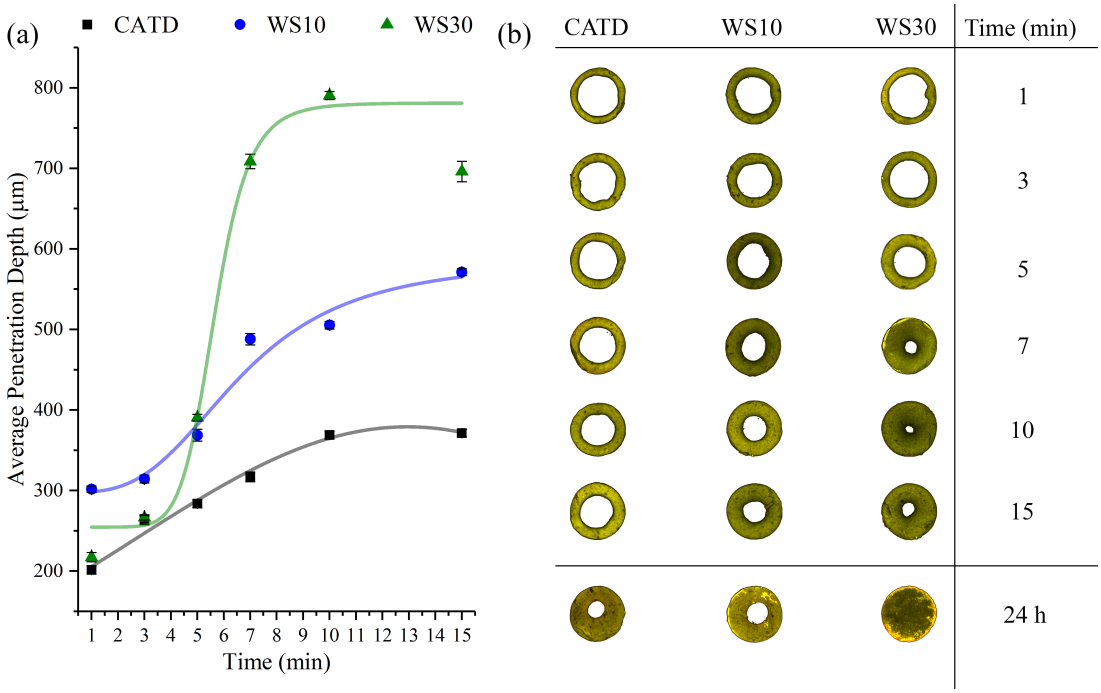

Figure 4.7: Average penetration depth using the 5nm probe. Cylindrical extrudates were left to incubate in the probe dispersion for various lengths of time, removed, bi-sectioned and the interior cross section imaged using a 488 nm laser coupled to CFM. Different incubation times were used to present a kinetic uptake study of the average penetration depth of the 5 nm probe into the extrudate. Where (a) shows the uptake trend of the probe over times and (b) is the extrudate cross section images taken at the corresponding times. The error for each measurement was calculated based on the standard deviation of 12 different measurement points from the probe penetration seen in the cross-sectioned images. WS30 shows higher uptake of the probe and a very different kinetic profile. A loss of accessibility is seen towards the centre of CATD and WS10 (24 h) due to the extrusion process. However, use of higher wt% porogen loadings largely negates this effect.

hexylheptyl)-perylene-3,4:9,10-bis-dicarboximide (PDI) while the larger 20/100 nm probes were carboxylate-modified microspheres. By impregnating the extrudates with the probe molecule, letting it incubate for various amounts of time, bi-sectioning and imaging the cross-section it is possible to establish a kinetic study of the penetration depth as a function of time.

Impregnating the catalyst body with the ∼5 nm probe, seen in Figure 4.7, it is possible to visualise the uptake and general diffusion characteristics of samples with

varying porosity. As expected, the porogen samples (WS10/30) show an overall higher penetration depth. Initially, all samples appear to have a similar uptake of the probe within the first 5 minutes. However, after this period, it is apparent the porogen-based samples exhibit a higher rate of diffusion (μm/min), after which they slow down and maintaining a steady rate. From these trend lines, it can be observed that the behaviour of the probe in terms of diffusion varies greatly with extrudates with different degrees of porosity. The most striking difference is seen in WS30, where the probe diffuses through the pores at a much higher rate overall and exhibits a very different kinetic profile. This is to be expected from the sample synthesised with the highest wt% porogen.

Complete diffusion of the ~5 nm probe into the WS30 samples takes place after 24 h.[66] However this does not appear to be the case for CATD and WS10, with the probe unable to penetrate into the centre completely. Clearly, some level of accessibility is lost at the centre of the extrudate. This is most likely caused by the extrusion process, where the shear stresses involved lead to different material density towards the centre compared to the near edge region of the catalyst body.[100] Even with the supposed increase in dimensionality using a porogen at 10 wt% it is apparent the inter-connectivity is not prevalent enough to allow for complete diffusion of the probe into the extrudate. However, it appears higher porogen loadings (>30 wt%) can largely negate this loss of accessibility. Interestingly, a large concentration of the probe is seen in the near edge area of WS30, this increased fluorescence could be indicative of the morphology created by the porogen cavities. The results for the rice starch porogen (RS30) are omitted as there was no penetration beyond the initial near edge region, indicating that significant pore blocking is present most likely due to incomplete calcination of the carbon template (Appendix Figure 9).

Diffusion of the 20/100 probes occurred very slowly and the changes seen at different time intervals was difficult to quantify, therefore a kinetic study was not conducted, with only the results of 24 h incubation time being presented (Figure 4.8). As with the ~5 nm probe, the average penetration depth is higher with increased porogen-induced loading. However the diffusion length of the probes are considerably less

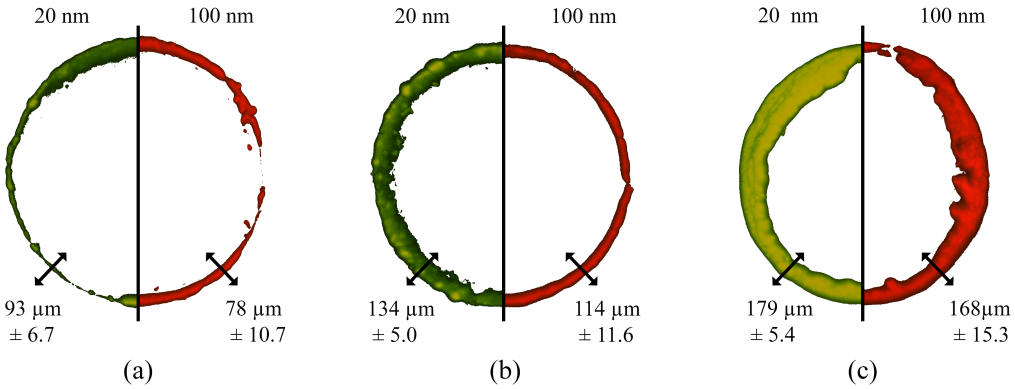

Figure 4.8: Average penetration depths using the 20/100 nm fluorescent probes for (a) CATD, (b) WS10 and (c) WS30 after 24 h incubation time. Diffusion of these probes occured very slowly and was slightly erratic, therefore no kinetic study was conducted. As with the 5 nm probe, higher porogen loadings led to greater accessibility. Compared to Hg-porosimetry measurements (Figure 4.2) these probes show the "real" accessibility of the extrudates.

than expected, taking into the account the data from the mercury porosimetry results which showed a large distribution of pores in the 200-400 nm region it was assumed this would be reflected in the probe measurements. It is therefore apparent that the "real" porosity of the catalyst bodies measured using probe experiments is different from that measured using bulk techniques such as porosimetry. While the porogen particle size (20 μm) should, in theory leave behind cavities in a large macro-pore size range, the micro/meso porosity which interconnects these cavities does not lead to an equivalent increase in accessibility. This is consistent with the theory that the meso-porous binder encloses the porogen cavity and largely prevents the 20/100 nm probes from penetrating to a certain extent (Appendix Figure 10). This affect appears to be more prevalent moving towards the centre, while increased porogen loadings appear to slightly mitigate this effect in the near-edge region.

4.2.2 Catalytic Performance

As with the previous chapter, the MTO reaction was performed on a fresh CATD sample as well as the two wheat starch induced porogens. Since no comparison to

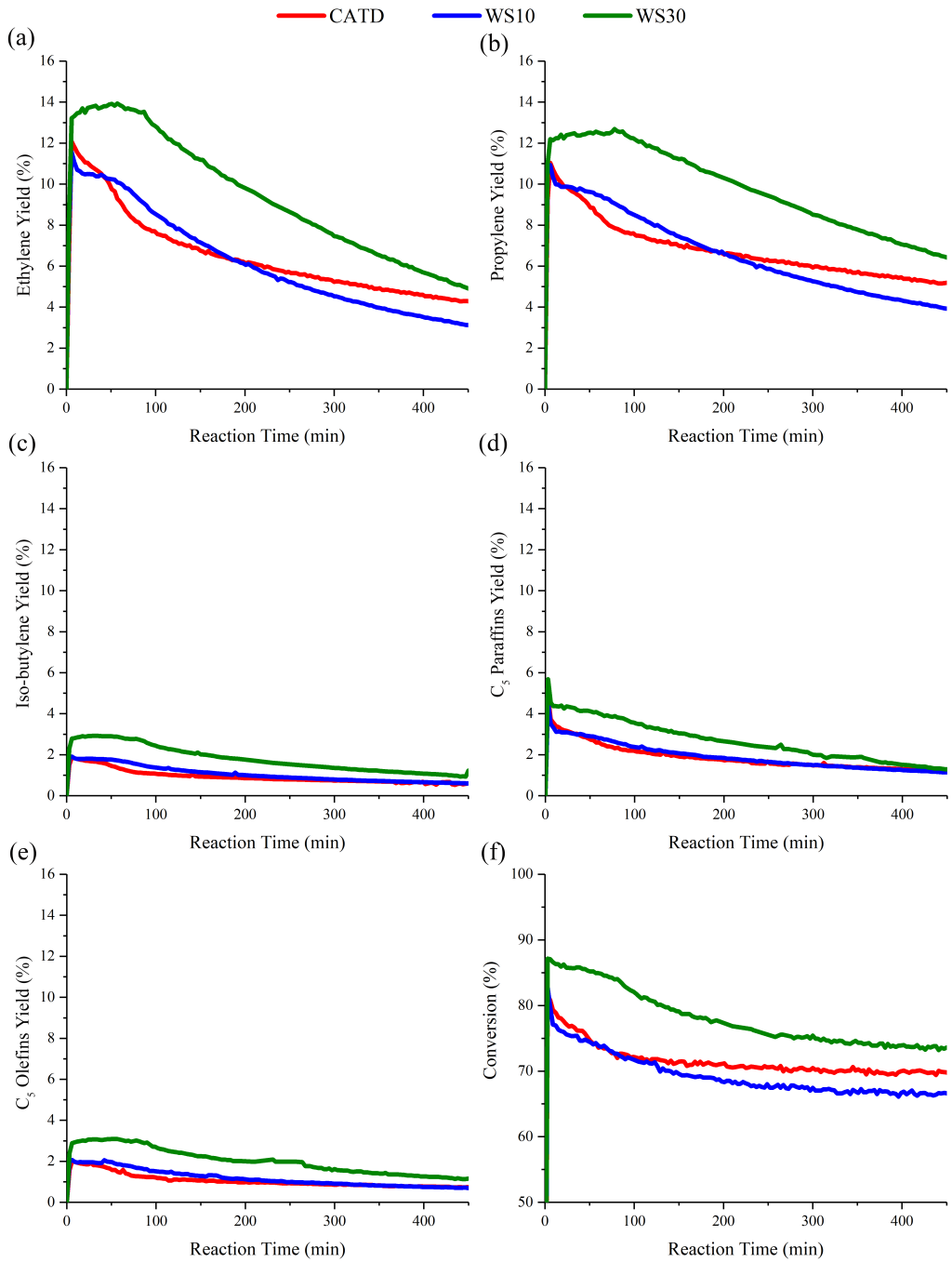

Figure 4.9: MTO data for all samples showing yields for (a) Ethylene, (b) Propylene, (c) Iso-butylene, (d) C_5 Paraffins, (e) C_5 Olefins and (f) % Conversion. A higher yield of all products is seen for WS30, due to better accessibility of acid sites through increasing macro-porosity. Graphs with error bars plotted can be seen in Appendix Figure 17.

the powder zeolite is made, these were not normalised to zeolite content. From the catalytic activity data seen in Figure 4.9 it is clear that the use of porogens affects

catalyst lifetime and selectivity towards certain products. Firstly, a larger yield of ethylene and propylene are seen for WS30, in comparison with the other samples CATD/WS10 which show very similar trends. This is consistent with the literature that stated hierarchical zeolites showed greater propylene selectivity.[63] This trend is seen all throughout the other products, though to a lesser extent. WS30 also shows the highest conversion, at above 80% for the first 2 h of reaction time, which, considering the zeolite mass per gram of catalyst, is significant. Unlike the catalytic data from the previous chapter on steaming, the absence of any acid site changes means there does not appear to be any dominance of either the alkene or aromatic cycle.

Overall, WS10 does not show any major changes compared to the parent extrudate sample, aside from a slightly lower initial selectivity to ethylene and propylene. This may appear contrary to the Hg-porosimetry and CFM characterisation data (Figure 4.2 and 4.7) which showed a noticeable change in porosity. These results indicate that the use of 10 wt% porogen does not lead to many significant changes in catalytic activity. WS30 on the other hand, produces a significant increase in the product selectivity as well as a slightly higher conversion. This could show that, at least initially, a larger portion of acid sites are available for reacting methanol.

Taking into account the results of the probe experiments, showing different diffusion regimes and overall accessibility, it is important to understand how these materials behave under catalytic conditions. As with the earlier chapter involving zeolite powders and alumina bound catalytst bodies, MTO will be used to assess the performance of the porogenic samples in terms of product selectivity and deactivation. Using the technique developed by Whiting et al. the extrudates are loaded into the reactor, then removed after a specific reaction time, bi-sectioned and imaged using CFM, making it possible to obtain a direct visual representation of the poly-aromatic species that are formed.[66] Similar to the technique used for the probe measurements; two lasers (488 and 642 nm) are used simultaneously to excite more or less conjugated molecules, where the longer absorption wavelengths correspond to larger species. These fluorescent images are grouped in green (small

or less conjugated) and red (large or more conjugated) fluorescent colours.

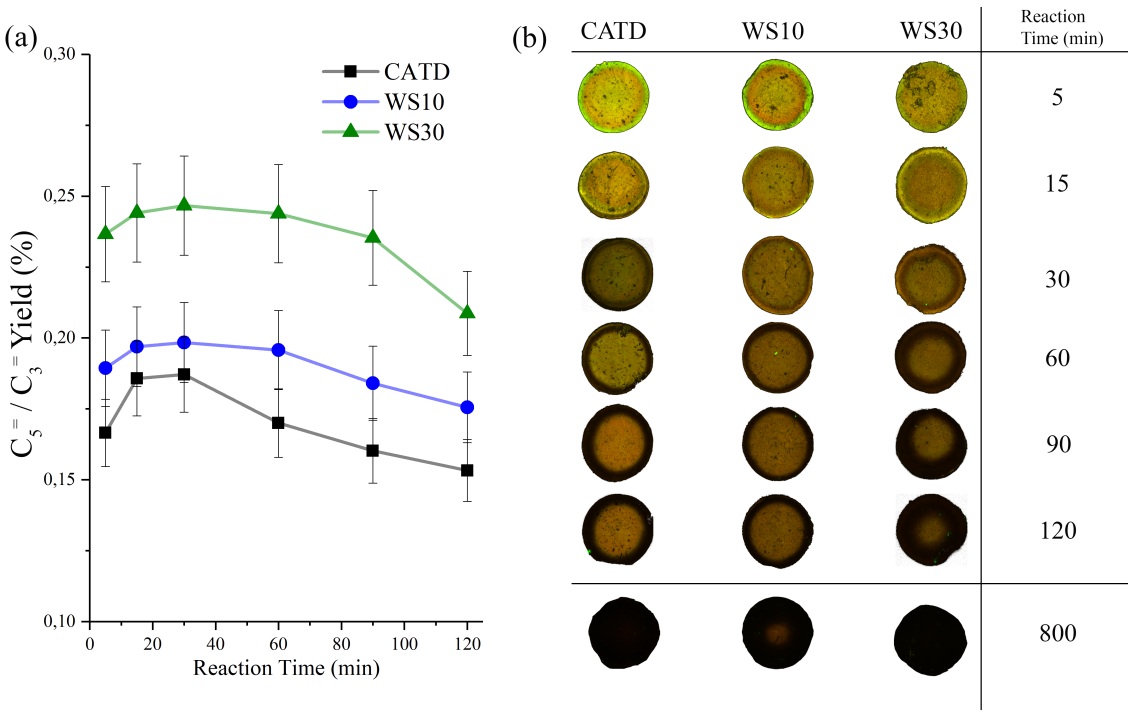

Figure 4.10: (a) C_5:C_3 olefin ratio from MTO measurements at different points in time and (b) bi-sectioned CFM images of spent catalyst. Extrudates were taken out of the reactor at various lengths of time, bi-sectioned and the cross section imaged using CFM with laser wavelength 509-749 nm. Different colours correspond to various poly-aromatic species in the extrudate with smaller molecules showing green/yellow fluorescence (naphthalene, phenanthrene etc.) while brown/red fluorescence corresponds to larger more conjugated species (coronene etc.). WS30 appears to deactivate faster (formation of non-fluorescent coke ring) but still retains a high C_5:C_3 olefin ratio. Despite significant coke formation large products are still able to leave the extrudate.

Figure 4.10(b) shows CFM images of the spent extrudates, taken out at different reaction times, while Figure 4.10a shows the ratio of C_5:C_3 olefins yield over the same lengths of time. UV-Vis micro-spectroscopy was used to measure the absorption spectra at the near-edge and centre of extrudate cross-sections (Appendix Figure 8) in order to validate the type of fluorescent aromatic species being formed, since the colours seen here correspond to several different types of molecules. In terms of catalytic performance it is important to look at the relationship between the fluorescent images, their specific boundary effects and the formation of specific products

from the reaction. Overall we can see that the core, which, according to the probe experiments shows a lesser degree of porosity is forming larger molecules which then become trapped in the centre, remaining largely unchanged while the near edge slowly deactivates. Furthermore, the larger molecules being formed throughout the catalyst mean that products such as C_5 olefins should find it more difficult to exit.

At 5 minutes reaction time a green fluorescent ring is seen in all samples, signifying this region contains mainly naphthalene type molecules, in contrast to the centre (yellow fluorescence) which most likely comprises of a mix of naphthalene, phenanthrene and pyrene type species. After 15 minutes reaction time the green colour is less striking but a ring of smaller naphthalene type molecules still remain. This stage of the reaction (15-30 minutes) corresponds to the maximum C_5:C_3 olefins yields seen in all samples, meaning at this point, a higher proportion of larger olefin products are able to form.

Deactivation begins after 60 minutes reaction time with the formation of non-fluorescent coke species in the near edge region of all the extrudates. The formation of this coke region along the perimeter begins to inhibit the movement of molecules into and out of the catalyst. This is reflected in the catalytic data (Figure 4.9) where a decrease in the trends of all products can be seen at this stage of the reaction. Comparing the fluorescent images of the CATD and WS30 samples at 60-90 minutes reaction time; clear differences in the polyaromatic species present can be observed (Figure 4.11). The near edge region of CATD becomes darker as any smaller molecules present (naphthalene, pyrene etc.) oligomerise into more conjugated coke species (Coronene etc.). A clear molecular transport boundary can be seen, where the formation of coke molecules in the near edge region prevent the movement of smaller species into this region. Therefore they in-turn, oligomerise in the centre, denoted by the striking colour change from green to orange. In contrast, WS30 forms a much larger coke region at this stage in the reaction but does not show any significant colour change in the catalyst centre. It can be assumed therefore, that due to the higher degree of porosity, smaller polyaromatic molecules are more mobile and are able to move throughout the extrudate, despite the presence of a

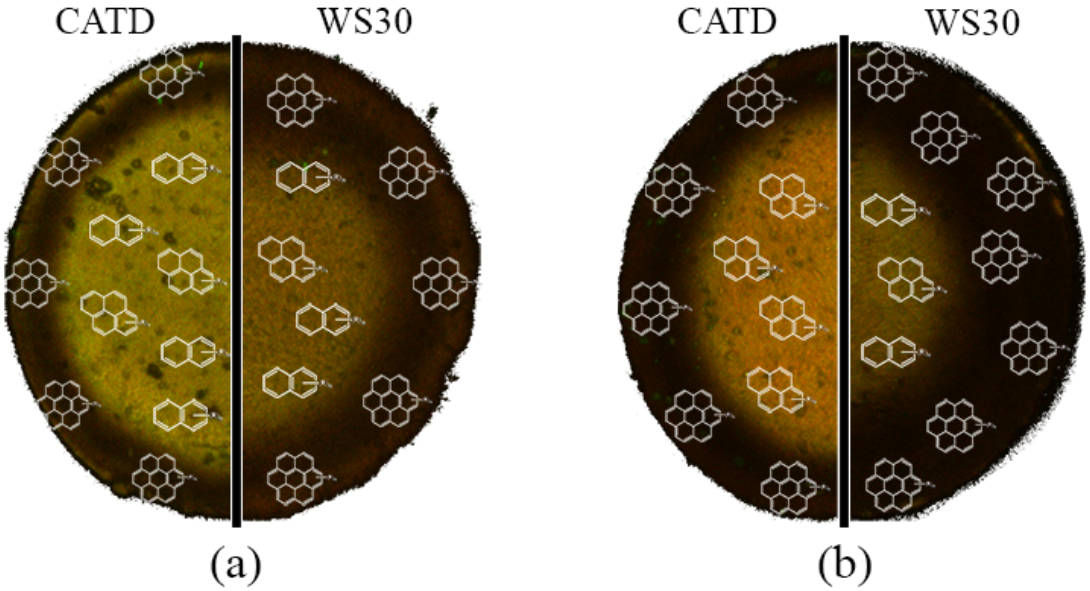

Figure 4.11: Half-half images of CATD and WS30 taken at (a) 60 minutes and (b) 90 minutes reaction time. Different colours in the centre and near-edge regions signify the formation of a molecular transport boundary. Smaller molecules in the centre of CATD are unable to diffuse into the near-edge region and oligomerise into larger species (colour change from green to orange). WS30 has better accessibility and therefore despite the presence of a visible molecular transport boundary, molecules in the centre are still able to diffuse throughout the extrudate.

visible molecular transport boundary. Looking at the C_5:C_3 graph, WS30 still shows a relatively higher yield, indicating larger products are still able to effectively form and leave the extrudate under these conditions. All samples show an increase in the 'coking front' which moves towards the centre at higher reaction times, with the effect being more pronounced in WS30 due to less size restrictions on the formation of coke molecules.

It is apparent that the more porous samples allow the exiting of larger C_5 products overall, despite the obvious deactivation taking place on the perimeter. This is most obvious in WS30, where despite the formation of a large "coke front", larger products still exit the catalyst body. As was observed in the MTO activity graphs (Figure 4.9), this sample produced a higher yield of all products overall, but the conversion dropped to the same levels as the other samples over time, which is

echoed by the visual representation of the coke formation in the spent extrudates. CATD shows a much lower ratio of heavy:light olefins, where the absence of large pores in significant numbers means the C_5 products become trapped. WS10 displays a similar trend of deactivation to CATD while producing a higher overall C_5:C_3 ratio. Amazingly, the centre of this sample still appears to fluoresce after several hours in the reactor, although being catalytically inactive. These visual representations show that a critical macro-pore volume exists, above which further increase in porosity no longer helps with the reduction of coke.[40]

Prior studies conducted on the use of hierarchical zeolite extrudates showed an increase in selectivity towards the larger of the light olefins (propylene > butene > ethene) as well as being more resistant to coking due to larger external surface area.[63] These results show that the use of pore-forming agents indeed continues this trend with the larger C_5 products. Additionally, while the bi-sectioned images of the most porous WS30 sample showed more coke formation compared to the others, the catalytic data indicates that is does not hinder the activity in the initial reaction period. Comparing the images taken from the probe experiments (Figure 4.8) and those seen in the bi-sectioned spent catalysts a relation between the accessibility of the probe and the size of the molecular transport boundary can be seen. This is not a 1:1 correlation as the interaction and diffusion of the probes are slightly different to that of catalytic molecules. Nevertheless, compared to bulk techniques, fluorescent probe experiments have shown to be an excellent method to correlate accessibility with the movement of aromatic species within the catalyst in the reactor.

Operando UV-Vis Spectroscopy

In addition to the cross sectional images taken using the CFM, *Operando* UV-Vis spectroscopy was also used to monitor the formation of poly-aromatic coke species, albeit in a quantitative manner. UV-Vis spectra of the porogen-based samples and the corresponding coke species can be seen in Figure 4.12. All samples show absorbances in the higher wavelength regions (>600 nm), indicating the formation

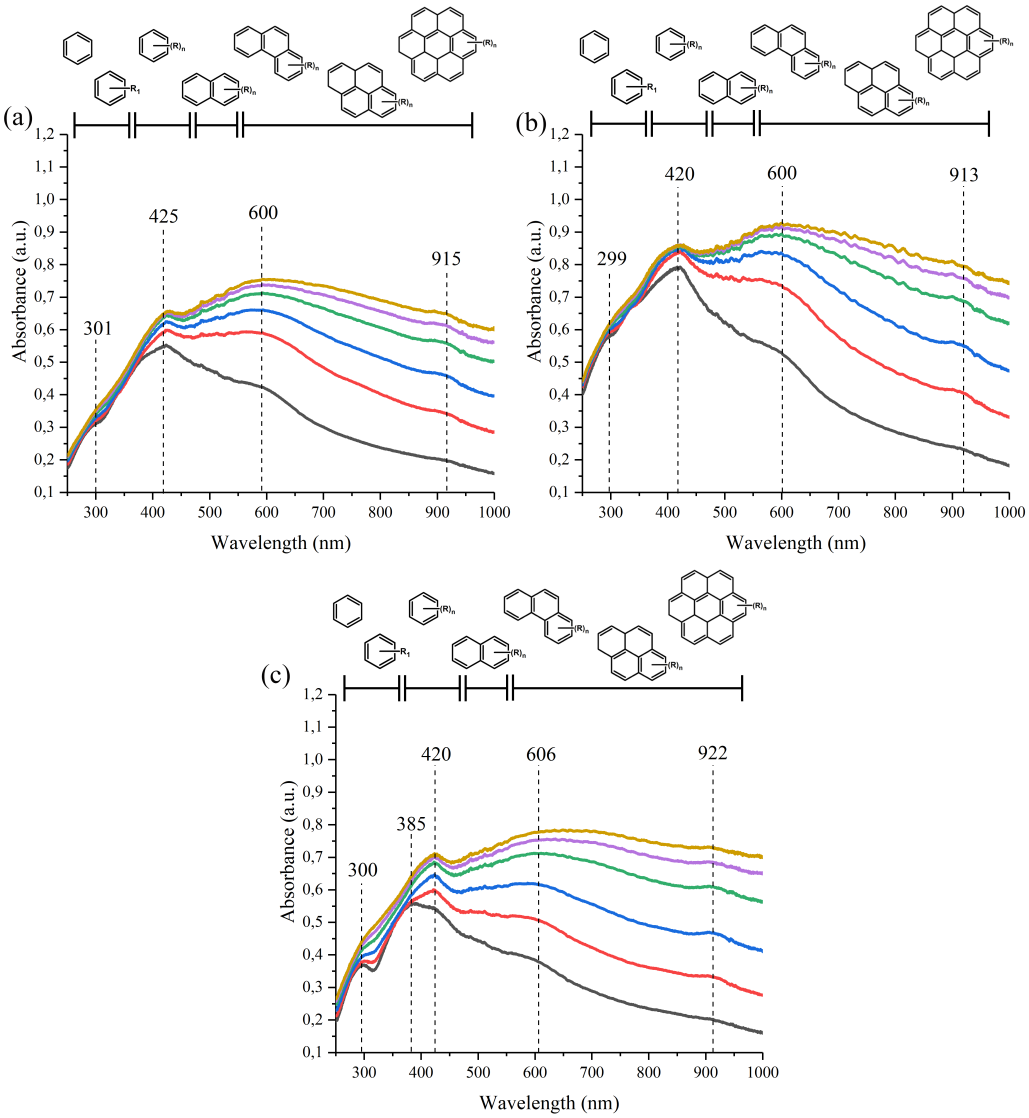

Figure 4.12: UV-Vis for MTO samples (a) CATD, (b) WS10 and (c) WS30. Spectral positions of poly-aromatic species was based on Konnov *et al.*[95] Spectra are plotted for 10, 50, 100, 150, 200 and 250 minutes reaction time in ascending order. All samples show absorbances in the higher wavelength regions (>600 nm), indicating the formation of larger, more conjugated species (pyrene, coronene etc.). Acidic properties should, in theory be the same, therefore absorbances are at similar positions but vary in terms of intensity. Comparing the CATD and WS30 samples it appears porogen induced macro-pores do not lead to a significant change in coke formation towards the surface/near-edge region of the extrudate.

of larger, more conjugated species (pyrene, coronene etc.). Smaller molecules such as methlyated benzenes (420-425 nm), formed towards the interior of the zeolite show similar absorbances in all samples. Unlike in the earlier chapter on steaming, where the changes in acidity resulted in the formation of different initial coke molecules, the porogen-based samples show the same absorbances, with varied intensities, since the acidic properties, should in theory be the same. Interestingly, WS10 shows a higher absorbance overall compared to the other two samples. This is contrary to what was seen in the cross-sectional images, which indicated WS30 produced the highest degree of coke formation. However, these UV-Vis spectra only account for the species visible at the catalyst surface. Taking into account the molecular transport boundaries discussed in the previous section, it is likely that coke molecules are trapped in the near edge region of WS10, unlike WS30 where the higher degree of porosity means some of these species can diffuse towards the centre. Comparing the CATD and WS30 samples however, it appears the creation of porogen induced macro-pores does not lead to a significant change in coke formation towards the surface/near-edge region of the extrudate.

In Summary, the use of a porogen to impart macro-porosity showed a much higher degree of accessibility, compared to conventional extrudates, using fluorescent probe molecules. However, the interaction of the porogen cavity with the binder meant that the degree of porosity seen was less than expected. Bi-sectioned extrudate cross-sections imaged with CFM showed the presence of molecular transport boundaries where different fluorescent species are concentrated. As a result, the change in porosity could be correlated to changes in the movement of these species and thus differences in said transport boundaries. The catalytic activity indicated that the 30 wt% porogen sample showed a much higher yield of all products, due to the greater accessibility as well as resistance to pore blocking during coke formation. As an initial study into the effects of porogens, the techniques used thus far have yielded significant results that can be adapted and/or expanded on for further studies and applications.

5 Conclusion and Outlook

5.1 Conclusion

In conclusion, the differences in acidic properties between zeolite powders and extrudates was investigated using a variety of chemical (Pyridine/CO IR etc.) and physical (Ar-physisorption) characterisation techniques, then tested catalytically in the MTO process. XRD results showed no degradation of the zeolite framework occurred due to hydrothermal treatment at 500°C for 7 h, compared to 700°C where a certain loss of crystallinity was observed. The dealumination process results in the creation of meso-pores, which was observed in the physisorption results. Pore size distributions indicated the higher Al content zeolite (38-500-steamed) showed pronounced meso-pore formation, with this effect difficult to observe in the extrudate samples, due to the meso-porous nature of the binder. Characterisation of the acidic properties using a combination of NH_3-TPD and CO/pyridine IR indicated a low silica/alumina ratio zeolite undergoes severe dealumination under hydrothermal treatment conditions, losing 98% of its Brønsted acid sites after 7 h of steaming. Extrudate samples appeared more robust, with a retention of acid sites after steaming compared to the powder samples. TM70-steamed showed the lowest decrease in BAS after steaming, with 32% of the parent acid sites being retained.

A kinetic study done using pyridine IR revealed that zeolites in the presence of an alumina binder (in the extrudate) were more resistant to dealumination through hydrothermal treatment. A large decrease in Lewis acid site concentration was seen after 15 minutes steaming time, and was attributed the migration of aluminium back

into the zeolite framework via extra-porous aluminium species arising from mostly the alumina binder. This "re-alumination" effect was deemed to be the most likely reason for the enhanced stability of BAS in the zeolite extrudate. However, without knowing the exact nature of the extra-porous species and which Al_{EF} are dominant in "re-alumination" this effect could not be confirmed without further studies, using techniques to differentiate between these various species.

The enhanced stability of the BAS did however, result in a higher selectivity towards propylene and lower coke formation in the MTO process for the steamed extrudate, compared to the (steamed) powder. Resistance to de-alumination coupled with a low BAS density and higher accessibility to active sites was shown to be the reason for this result. As dealumination through steaming can also occur in the methanol reactor, these findings are significant for further use of extrudates for industrial reactor conditions. Mild steaming conditions (500°C) can be used to effectively tune a zeolite extrudate to produce a higher yield of propylene or indeed modify such pre-treatment techniques to account for any steaming that may occur in the reactor. The extrudate binder has been shown to interact with the zeolite, influencing the catalytic reaction. Therefore, these binder effects can be advantageous for industrial purposes, with the (alumina) binder regenerating the acid sites that may be lost due to de-alumination in the reactor. On the other hand, if no re-insertion of atoms into the zeolite framework is desired, the choice of binder will need to be carefully considered.

In the second chapter, further macro-porosity was introduced into zeolite extrudates through the use of a porogen/pore forming agent. Characterisation using fluorescent nano-probes coupled to CFM indicated that a 30 wt% porogen based extrudate showed a significantly higher degree of accessibility throughout the catalyst body, with the 5 nm probe able to completely diffuse into the centre and the 20/100 nm probes penetration noticeably further compared to the parent, non-porogen based extrudate. Hg-porosimetry data showed a large distribution of pores in the 200-400 nm range, however when compared to the probe experiments it became evident that this 'bulk' porosity measurement was only applicable to the near edge region.

Clearly, the diffusion of the probes is a more realistic measure of the porosity, as opposed to bulk techniques which do not inform us on accessibility.

Using a similar technique, spent extrudates were removed from the MTO reactor at different times and imaged using CFM to identify specific regions related to the presence of various aromatic species. A molecular transport boundary was identified in all samples, where smaller species (naphtalene etc.) were mobile in the near edge region compared to the centre where larger species such as phenanthrene and pyrenes could be found. Unlike in the parent extrudate, a higher degree of accessibility meant poly-aromatic molecules in the 30 wt% porogen-based sample were able to diffuse between the regions defined by the molecular transport boundary. However, coke formation in this sample occurred earlier in the reaction and to a greater extent. Correlating these results to those seen in the MTO product distributions, WS30 showed a higher C_5:C_3 olefin yield ratio, even when deactivation started to occur. Therefore a balance between increased accessibility and coke formation exists, although the porogen-based sample maintained a higher yield of all MTO products. A relation between accessibility of the probes and molecular transport boundaries in the spent extrudates was found, emphasising that probe experiments coupled to CFM is an effective method to correlate accessibility in characterisation to catalytic results. It is therefore possible to predict the molecular transport of a catalyst before being placed in the reactor. The ease of measurement could make this technique ideal for industrial applications utilising extrudate catalysts and even applied to any other type of porous materials.

5.2 Outlook

In addition to the results obtained here there are several further studies that could be conducted in order to re-inforce and/or expand on the results of this study. Firstly, ^{27}Al and ^{29}Si Nuclear Magnetic Resonance (NMR) can be utilised in order to shed light on the exact species that are produced in the hydrothermal treatment process

and the extent to which they increase/decrease. Furthermore, NMR can be used in order to distinguish between zeolite framework Al/Si groups, Al arising from the binder and extra-framework species, owing to the different chemical shifts.[34] Armed with this knowledge, the mechanism(s) that facilitate the stabilisation of acid sites can be more easily visualised. Finally, the modification of the zeolite with different framework species was not attempted due to the complexities of the system. It has been shown that the use of framework boron increases the extent to which Al migrates into the zeolite (from the binder) under hydrothermal conditions, due mainly to the hydrolytic instability of framework B.[86] Using a high silica content zeolite such as ZSM-5 117 with B exchange, we could observe the formation of framework BAS and an increase in acid site density yielding interesting catalytic results.

Similarly, there are several avenues of expansion for the use of porogens. Rice and wheat starch were chosen for their large difference in particle size. As the rice starch porogen could not be successfully removed from the catalyst body it seems the use of larger porogens (> 15 μm) is more worth exploring further. This study showed the porogen mainly interacts with the binder, with a macro-porous cage interconnected with meso-pores. Reducing the binder content (70:30 zeolite/binder) could yield better connectivity in the macro-pore range, observable in the possibly better diffusion of the larger fluorescent probes. This would catalytically, result in better conversion, but could compromise the lifetime and mechanical stability. A final interesting aspect would be the use of a porogen of different morphology, such as carbon nano-fibres (14 x 600 μm), which would hypothetically create truly macro-porous hierarchical channels.[101] This different form of inter-connectivity could mean that mobile species, such as those seen in the bi-sectioned CFM images could diffuse between various areas of the catalyst more effectively, resulting in no molecular transport boundaries.

Acknowledgements

First and foremost, I would like to extent my gratitude towards my supervisors. My daily supervisor Nikos, for always being there to assist me with anything I needed help with and for general discussions related to the project. My first supervisor, Gareth, for his continued guidance throughout the project and for not only telling me when I performed well but also where I could improve. I would like to thank my second supervisor Pieter for allowing me to start another research project and for his feedback at any meetings we had. I would also like to thank my supervisors from my earlier project, Sander and Peter for their continued support even after I had switched topics.

Additionally, there are several people who trained me/helped with the use of various techniques that I needed for my project, in no particular order I would like to thank; Ioannis for his help with the steaming setup, Gareth for teaching me how to use the extruder, Sander, Lennart, Remco and Miguel for meausring physisorption on my behalf, Dennie for the XRD training and TGA measurements, Bea and Ramon for helping with TPD measurements, Paul for the training and helpful discussions related to CO/pyridine IR, Dongling for helping with UV-Vis and CFM measurements, Max for showing me how to properly use the CRAIC, Nikos for doing the SEM measurements and always correcting me when I got it wrong, and finally, everyone involved with the MTO setup for their helpful discussions/feedback.

Lastly, I would like to thank everyone at ICC for making me feel very welcome and enjoy the (more than) 2 years I spent there.

Bibliography

[1] British Petroleum; *BP Statistical Review of World Energy 2017*; Tech. Rep. 66; British Petroleum; 2017.

[2] Ennaert, T.; Van Aelst, J.; Dijkmans, J.; De Clercq, R.; Schutyser, W.; Dusselier, M.; Verboekend, D.; Sels, B. F. *Chem. Soc. Rev.* **2016**, *45*, 584–611.

[3] Wang, W.; Jiang, Y.; Hunger, M. *Catalysis Today* **2006**, *113*, 102–114.

[4] Chorkendorff, I.; Niemantsverdriet, J. W. *Concepts of Modern Catalysis and Kinetics*, 2nd ed.; Wiley-VCH Verlag GmbH & Co. KGaA, 2003.

[5] Chester, A. W.; Derouane, E. G. *Zeolite Characterization and Catalysis*; Springer Science & Business Media, 2009, 2009.

[6] Derouane, E. G.; Védrine, J. C.; Ramos Pinto, R.; Borges, P. M.; Costa, L.; Lemos, M. A.; Lemos, F.; Ramôa Ribeiro, F. *Catalysis Reviews - Science and Engineering* **2013**, *55*, 454–515.

[7] De, S.; Dutta, S.; Saha, B. *Catalysis Science and Technology* **2016**, *6*, 7364–7385.

[8] *International Zeolite Association*. `http://www.iza-online.org`.

[9] Baerlocher, C.; McCusker, L.; Olson, D. *ATLAS OF ZEOLITE FRAMEWORK TYPES sixth revised edition 2007*; Amsterdam: Elsevier, 2007.

[10] Kokotailo, G.; Lawton, S.; Olson, D.; Meier, W. *Nature* **1978**, *272*, 437–438.

[11] Corma, A.; Martinez, A. *Advanced Materials* **1995**, *7*, 137–144.

[12] Mores, D.; Kornatowski, J.; Olsbye, U.; Weckhuysen, B. M. *Chemistry - A European Journal* **2011**, *17*, 2874–2884.

[13] Mitchell, S.; Michels, N.-L.; Pérez-Ramírez, J. *Chemical Society Reviews* **2013**, *42*, 6094.

[14] Rahimi, N.; Karimzadeh, R. *Applied Catalysis A: General* **2011**, *398*, 1–17.

[15] Lu, J.; Zhao, Z.; Xu, C.; Duan, A.; Wang, X.; Zhang, P. *Journal of Porous Materials* **2008**, *15*, 213–220.

[16] Jung, J. S.; Kim, T. J.; Seo, G. *Korean Journal of Chemical Engineering* **2004**, *21*, 777–781.

[17] Mukarakate, C.; Watson, M. J.; ten Dam, J.; Baucherel, X.; Budhi, S.; Yung, M. M.; Ben, H.; Iisa, K.; Baldwin, R. M.; Nimlos, M. R. *Green Chem.* **2014**, *16*, 4891–4905.

[18] Moliner, M.; Roman-Leshkov, Y.; Davis, M. E. *Proceedings of the National Academy of Sciences* **2010**, *107*, 6164–6168.

[19] Fan, Y.; Bao, X.; Lin, X.; Shi, G.; Liu, H. *Journal of Physical Chemistry B* **2006**, *110*, 15411–15416.

[20] Yang, X.-Y.; Chen, L.-H.; Li, Y.; Rooke, J. C.; Sanchez, C.; Su, B.-L. *Chem. Soc. Rev.* **2017**, *46*, 481–558.

[21] Li, K.; Valla, J.; Garcia-Martinez, J. *ChemCatChem.* **2014**, *6*, 46–66.

[22] Schwieger, W.; Machoke, A. G.; Weissenberger, T.; Inayat, A.; Selvam, T.; Klumpp, M.; Inayat, A. *Chem. Soc. Rev.* **2016**, *45*, 3353–3376.

[23] Silaghi, M. C.; Chizallet, C.; Raybaud, P. *Microporous and Mesoporous Materials* **2014**, *191*, 82–96.

[24] Gayubo, A. G.; Aguayo, A. T.; Atutxa, A.; Prieto, R.; Bilbao, J. *Industrial and Engineering Chemistry Research* **2004**, *43*, 5042–5048.

[25] Maier, S. M.; Jentys, A.; Lercher, J. A. *Journal of Physical Chemistry C* **2011**, *115*, 8005–8013.

[26] Lutz, W.; Shutilov, R. A.; Gavrilov, V. Y. *Zeitschrift fur Anorganische und Allgemeine Chemie* **2014**, *640*, 577–581.

[27] Shihabi, D. S.; Garwood, W. E.; Chu, P.; Miale, J. N.; Lago, R. M.; Chu, C. T.; Chang, C. D. *Journal of Catalysis* **1985**, *93*, 471–474.

[28] Beers, A. E.; Van Bokhoven, J. A.; De Lathouder, K. M.; Kapteijn, F.; Moulijn, J. A. *Journal of Catalysis* **2003**, *218*, 239–248.

[29] Beyerlein, R. A.; Choi-feng, C.; Hall, J. B.; Huggins, B. J.; Ray, G. J. *Topics in Catalysis* **1997**, *4*, 27–42.

[30] Keil, F. J. *Microporous and Mesoporous Materials* **1999**, *29*, 49–66.

[31] Aramburo, L. R.; Karwacki, L.; Cubillas, P.; Asahina, S.; De Winter, D. A.; Drury, M. R.; Buurmans, I. L.; Stavitski, E.; Mores, D.; Daturi, M.; Bazin, P.; Dumas, P.; Thibault-Starzyk, F.; Post, J. A.; Anderson, M. W.; Terasaki, O.; Weckhuysen, B. M. *Chemistry - A European Journal* **2011**, *17*, 13773–13781.

[32] Van Donk, S.; Janssen, A. H.; Bitter, J. H.; De Jong, K. P. *Catalysis Reviews - Science and Engineering* **2003**, *45*, 297–319.

[33] Wouters, B. H.; Chen, T.; Grobet, P. J. *Journal of Physical Chemistry B* **2001**, *105*, 1135–1139.

[34] Ong, L. H.; Domok, M.; Olindo, R.; Van Veen, A. C.; Lercher, J. A. *Microporous and Mesoporous Materials* **2012**, *164*, 9–20.

[35] Aramburo, L. R.; Teketel, S.; Svelle, S.; Bare, S. R.; Arstad, B.; Zandbergen, H. W.; Olsbye, U.; De Groot, F. M. F.; Weckhuysen, B. M. *Journal of Catalysis* **2013**, *307*, 185–193.

[36] Milina, M.; Mitchell, S.; Crivelli, P.; Cooke, D.; Pérez-Ramírez, J. *Nature Communications* **2014**, *5*.

[37] Serrano, D. P.; Escola, J. M.; Pizarro, P. *Chem. Soc. Rev.* **2013**, *42*, 4004–4035.

[38] Losch, P.; Hoff, T.; Kolb, J.; Bernardon, C.; Tessonnier, J.-P.; Louis, B. *Catalysts* **2017**, *7*, 225.

[39] Gueudré, L.; Milina, M.; Mitchell, S.; Pérez-Ramírez, J. *Advanced Functional Materials* **2014**, *24*, 209–219.

[40] Milina, M.; Mitchell, S.; Cooke, D.; Crivelli, P.; Pérez-Ramírez, J. *Angewandte Chemie - International Edition* **2015**, *54*, 1591–1594.

[41] Serrano, D. P.; García, R. A.; Vicente, G.; Linares, M.; Procházková, D.; Čejka, J. *Journal of Catalysis* **2011**, *279*, 366–380.

[42] Puértolas, B.; Veses, A.; Callén, M. S.; Mitchell, S.; García, T.; Pérez-Ramírez, J. *ChemSusChem* **2015**, *8*, 3283–3293.

[43] Bingre, R.; Louis, B.; Nguyen, P. *Catalysts* **2018**, *8*, 163.

[44] Whiting, G. T.; Chowdhury, A. D.; Oord, R.; Paalanen, P.; Weckhuysen, B. M. *Faraday Discuss.* **2016**, *188*, 369–386.

[45] Hargreaves, J. S. J.; Munnoch, A. L. *Catal. Sci. Technol. Catal. Sci. Technol* **2013**, *3*, 1165–1171.

[46] Michels, N. L.; Mitchell, S.; Pérez-Ramírez, J. *ACS Catalysis* **2014**, *4*, 2409–2417.

[47] Zhang, S.; Gong, Y.; Zhang, L.; Liu, Y.; Dou, T.; Xu, J.; Deng, F. *Fuel Processing Technology* **2015**, *129*, 130–138.

[48] Uguina, M. A.; Sotelo, J. L.; Serrano, D. P. *Applied Catalysis* **1991**, *76*, 183–198.

[49] Michels, N. L.; Mitchell, S.; Pérez-Ramírez, J. *ACS Catalysis* **2014**, *4*, 2409–2417.

[50] Dele-Afolabi, T. T.; Hanim, M. A.; Norkhairunnisa, M.; Sobri, S.; Calin, R. *Ceramics International* **2017**, *43*, 1633–1649.

[51] Prabhakaran, K.; Melkeri, A.; Gokhale, N. M.; Sharma, S. C. *Ceramics International* **2007**, *33*, 77–81.

[52] Chevalier, E.; Chulia, D.; Pouget, C.; Viana, M. *Journal of Pharmaceutical Sciences* **2008**, *97*, 1135–1154.

[53] Devyatkov, S.; Kuzichkin, N. V.; Murzin, D. Y. *Chimica Oggi/Chemistry Today* **2015**, *33*, 57–64.

[54] Oygarden, A.; Pérez-Ramírez, J.; Waller, G.; Schoffel, K.; Brackenbury, D.; *Method for producing supported oxide catalysts*; 2004.

[55] Gu, L.; Ma, D.; Yao, S.; Liu, X.; Han, X.; Shen, W.; Bao, X. *Chemistry - A European Journal* **2009**, *15*, 13449–13455.

[56] Wu, X.; Abraha, M. G.; Anthony, R. G. *Applied Catalysis A: General* **2004**, *260*, 63–69.

[57] Olsbye, U.; Svelle, S.; Bjrgen, M.; Beato, P.; Janssens, T. V.; Joensen, F.; Bordiga, S.; Lillerud, K. P. *Angewandte Chemie - International Edition* **2012**, *51*, 5810–5831.

[58] Goetze, J.; Weckhuysen, B. M. *Catalysis Science and Technology* **2018**, *8*, 1632–1644.

[59] Lesthaeghe, D.; Van Speybroeck, V.; Marin, G. B.; Waroquier, M. *Industrial and Engineering Chemistry Research* **2007**, *46*, 8832–8838.

[60] Dahl, I. M.; Kolboe, S. *Catalysis Letters* **1993**, *20*, 329–336.

[61] Chowdhury, A. D.; Paioni, A. L.; Houben, K.; Whiting, G. T.; Baldus, M.; Weckhuysen, B. M. *Angewandte Chemie - International Edition* **2018**, *57*, 8095–8099.

[62] Svelle, S.; Joensen, F.; Nerlov, J.; Olsbye, U.; Lillerud, K. P.; Kolboe, S.; Bjørgen, M. *Journal of the American Chemical Society* **2006**, *128*, 14770–14771.

[63] Mitchell, S.; Michels, N. L.; Kunze, K.; Pérez-Ramírez, J. *Nature Chemistry* **2012**, *4*, 825–831.

[64] Liang, T.; Chen, J.; Qin, Z.; Li, J.; Wang, P.; Wang, S.; Wang, G.; Dong, M.; Fan, W.; Wang, J. *ACS Catalysis* **2016**, *6*, 7311–7325.

[65] Emeis, C. A.; *Determination of integrated molar extinction coefficients for infrared absorption bands of pyridine adsorbed on solid acid catalysts*; 1993.

[66] Whiting, G. T.; Nikolopoulos, N.; Nikolopoulos, I.; Chowdhury, A. D.; Weckhuysen, B. M. *Nature Chemistry* **2019**, *11*, 23–31.

[67] Abell, A.; Willis, K.; Lange, D. *Journal of Colloid and Interface Science* **1999**, *211*, 39–44.

[68] Mueller, M. *Spie Press Book* **1996**, *2*, 1–8.

[69] Borodina, E.; Meirer, F.; Lezcano-González, I.; Mokhtar, M.; Asiri, A. M.; Al-Thabaiti, S. A.; Basahel, S. N.; Ruiz-Martinez, J.; Weckhuysen, B. M. *ACS Catalysis* **2015**, *5*, 992–1003.

[70] Aramburo, L. R.; Ruiz-Martínez, J.; Sommer, L.; Arstad, B.; Buitrago-Sierra, R.; Sepúlveda-Escribano, A.; Zandbergen, H. W.; Olsbye, U.; deGroot, F. M.; Weckhuysen, B. M. *ChemCatChem* **2013**, *5*, 1386–1394.

[71] Koningsveld, H. v.; Jansen, J. C.; Bekkum, H. v. *Zeolites* **1990**, *10*, 235–242.

[72] Sotomayor, F. J.; Cychosz, K. A.; Thommes, M. *Accounts of Materials and Surface Research* **2018**, *3*, 34–50.

[73] Sing, K. S. W. *Pure and Applied Chemistry* **1985**, *57*.

[74] Aramburo, L. R.; Wirick, S.; Miedema, P. S.; Buurmans, I. L. C.; de Groot, F. M. F.; Weckhuysen, B. M. *Physical Chemistry Chemical Physics* **2012**, *14*, 6967.

[75] Grejtak, F.; Horvath, I.; Krajcovic, J.; Kubranova, M. *Ceramics International* **1993**, *152*, 149–152.

[76] Van Mao, R. L.; Al-Yassir, N.; Lu, L.; Vu, N. T.; Fortier, A. *Catalysis Letters* **2006**, *112*, 13–18.

[77] Szanyi, J.; Paffett, M. T. *Microporous Materials* **1996**, *7*, 201–218.

[78] Benaliouche, F.; Boucheffa, Y.; Ayrault, P.; Mignard, S.; Magnoux, P. *Microporous and Mesoporous Materials* **2008**, *111*, 80–88.

[79] Topsøe, N. Y.; Pedersen, K.; Derouane, E. G. *Journal of Catalysis* **1981**, *70*, 41–52.

[80] Velthoen, M. E.; Nab, S.; Weckhuysen, B. M. *Physical Chemistry Chemical Physics* **2018**, *20*, 21647–21659.

[81] Wan, J.; Wei, Y.; Liu, Z.; Li, B.; Qi, Y.; Li, M.; Xie, P.; Meng, S.; He, Y.; Chang, F. *Catalysis Letters* **2008**, *124*, 150–156.

[82] Vimont, A.; Thibault-Starzyk, F.; Daturi, M. *Chemical Society Reviews* **2010**, *39*, 4928–4950.

[83] Isernia, L. F. *Materials Research* **2013**, *16*, 792–802.

[84] Yu, Z.; Li, S.; Wang, Q.; Zheng, A.; Jun, X.; Chen, L.; Deng, F. *Journal of Physical Chemistry C* **2011**, *115*, 22320–22327.

[85] Xue, N.; Vjunov, A.; Schallmoser, S.; Fulton, J. L.; Sanchez-Sanchez, M.; Hu, J. Z.; Mei, D.; Lercher, J. A. *Journal of Catalysis* **2018**, *365*, 359–366.

[86] Chang, C. D.; Hellring, S. D.; Miale, J. N.; Schmitt, K. D.; Brigandi, P. W.; Wu, E. L. *J. Chem. Soc. Faraday Trans.* **1985**, *81*, 2215–2224.

[87] Deka, R. C. *Indian Journal of Chemical Technology* **1998**, *5*, 109–123.

[88] Whiting, G. T.; Meirer, F.; Valencia, D.; Mertens, M. M.; Bons, A.-J.; Weiss, B. M.; Stevens, P. A.; de Smit, E.; Weckhuysen, B. M. *Phys. Chem. Chem. Phys.* **2014**, *16*, 21531–21542.

[89] Whiting, G. T.; Chowdhury, A. D.; Oord, R.; Paalanen, P.; Weckhuysen, B. M. *Faraday Discuss.* **2016**, *188*, 369–386.

[90] Valencia, D.; Whiting, G. T.; Bulo, R. E.; Weckhuysen, B. M. *Physical Chemistry Chemical Physics* **2016**, *18*, 2080–2086.

[91] Mei, C.; Wen, P.; Liu, Z.; Liu, H.; Wang, Y.; Yang, W.; Xie, Z.; Hua, W.; Gao, Z. *Journal of Catalysis* **2008**, *258*, 243–249.

[92] Sun, X.; Mueller, S.; Liu, Y.; Shi, H.; Haller, G. L.; Sanchez-Sanchez, M.; Van Veen, A. C.; Lercher, J. A. *Journal of Catalysis* **2014**, *317*, 185–197.

[93] Müller, S.; Liu, Y.; Kirchberger, F. M.; Tonigold, M.; Sanchez-Sanchez, M.; Lercher, J. A. *Journal of the American Chemical Society* **2016**, *138*, 15994–16003.

[94] Guisnet, M.; Costa, L.; Ribeiro, F. R. *Journal of Molecular Catalysis A: Chemical* **2009**, *305*, 69–83.

[95] Konnov, S. V.; Pavlov, V. S.; Kots, P. A.; Zaytsev, V. B.; Ivanova, I. I. *Catalysis Science and Technology* **2018**, *8*, 1564–1577.

[96] Schwieger, W.; Machoke, A. G.; Weissenberger, T.; Inayat, A.; Selvam, T.; Klumpp, M.; Inayat, A. *Chemistry Society Reviews* **2016**, *45*, 3353–3376.

[97] Groen, J. C.; Brouwer, S.; Peffer, L. A.; Pérez-Ramírez, J. *Particle and Particle Systems Characterization* **2006**, *23*, 101–106.

[98] Kenvin, J.; Jagiello, J.; Mitchell, S.; Pérez-Ramírez, J. *Langmuir* **2015**, *31*, 1242–1247.

[99] Hossen, M. S.; Sotome, I.; Takenaka, M.; Isobe, S.; Nakajima, M.; Okadome, H. *Japan Journal of Food Engineering* **2011**, *12*, 29–35.

[100] Alazzawi, M. K.; Murali, S.; Haber, R. A. *Materials Sciences and Applications* **2017**, *08*, 933–947.

[101] Isobe, T.; Tomita, T.; Kameshima, Y.; Nakajima, A.; Okada, K. *Journal of the European Ceramic Society* **2006**, *26*, 957–960.

[102] Schmidt, J. E.; Poplawsky, J. D.; Mazumder, B.; Attila, ; Fu, D.; de Winter, D. A.; Meirer, F.; Bare, S. R.; Weckhuysen, B. M. *Angewandte Chemie - International Edition* **2016**, *55*, 11173–11177.

Appendix

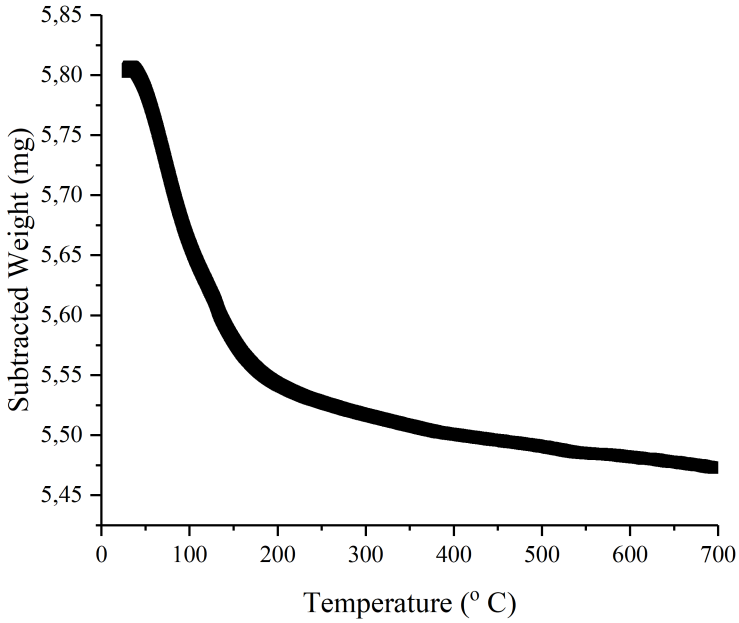

Figure 1: TGA results for WS30 showing the weight loss over a increase in temperature at 2.5°C/min. This was used as a benchmark to determine the conditions for the calcination process of all porogen samples.

Physical properties	CATAPAL D	PURAL TM70	PURAL TH100
Particle size (μm)	40	35	35
BET surface area (m^2/g)	220	200	150
Pore volume (ml/g)	0.55	0.75	1.10
Crystalline size (nm)	7	8	15

Table 1: Technical Data of binder only, courtesy of SASOL Performance Chemicals

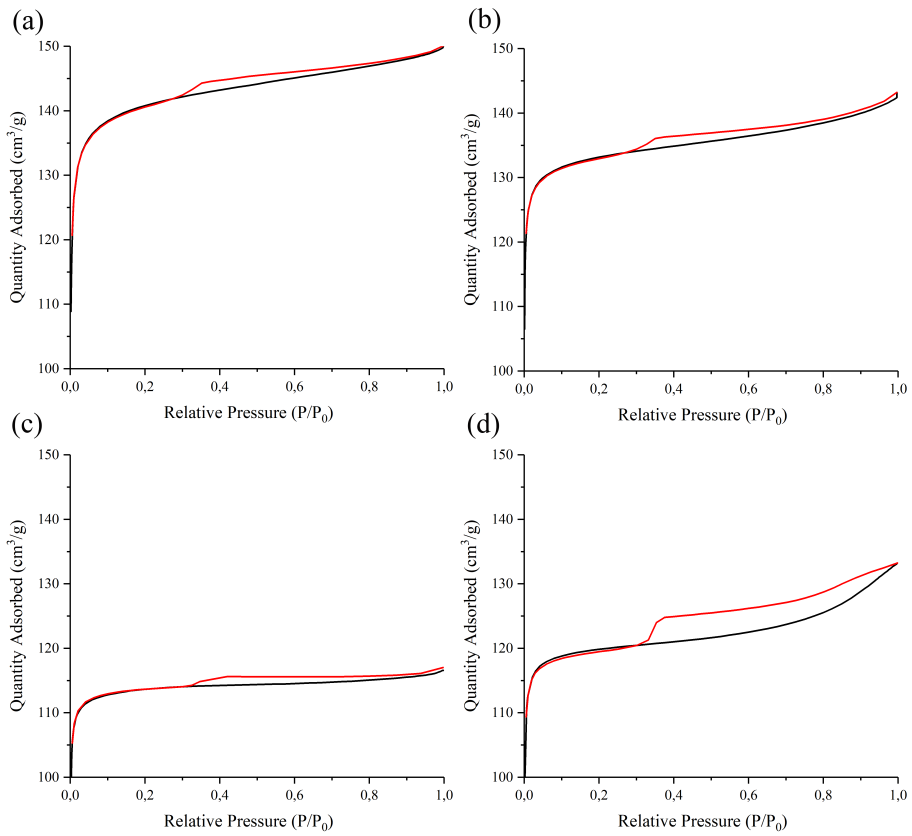

Figure 2: Argon adsorption and desorption isotherms of all ZSM5 samples, where the black and red lines correspond to adsorption and desorption isotherms respectively. Isotherms are classified as Type I, while the hysteresis loop is Type H4.[73]

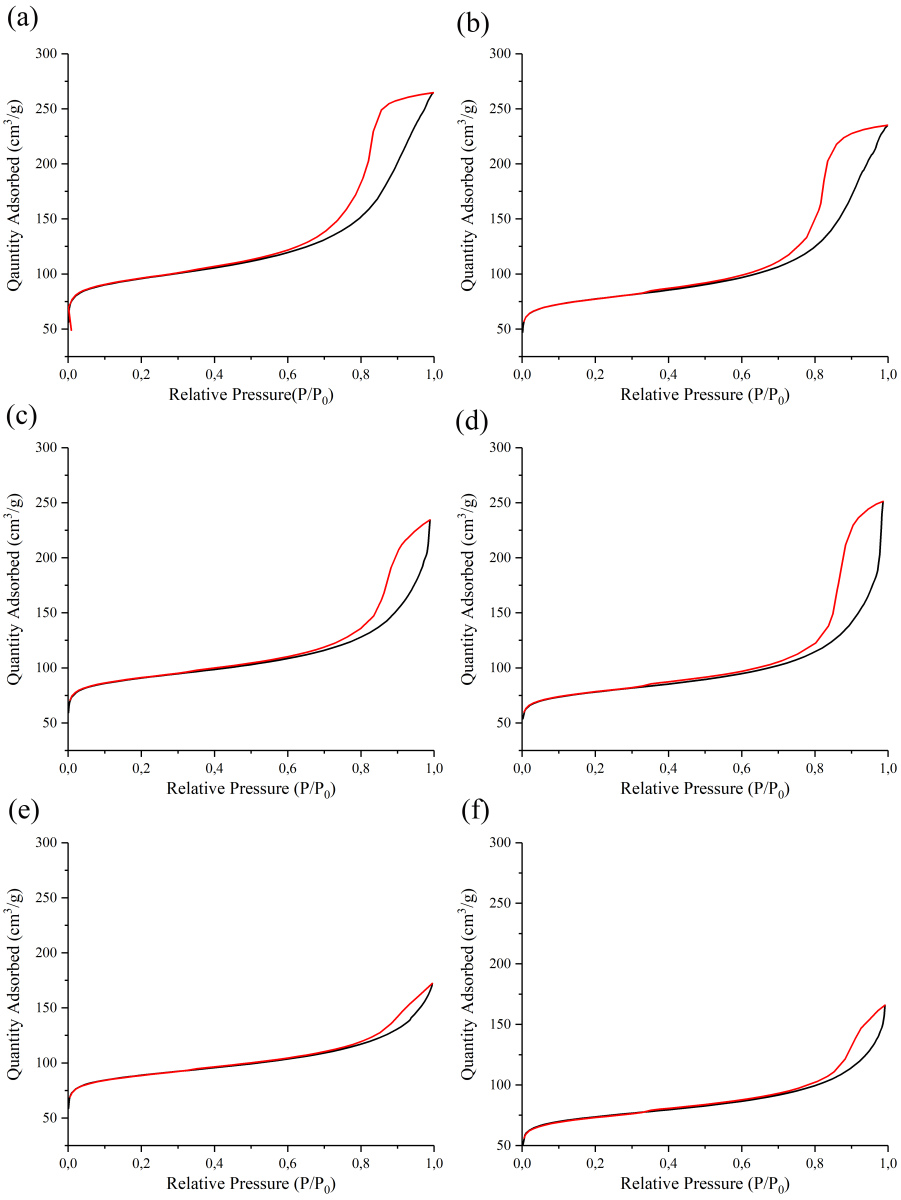

Figure 3: Physisorption isotherms for extrudate samples.Isotherms of a-b can be classified as Type IV,characteristic of meso-porous adsorbants, while the hysteresis is most similar to Type H2. Samples c-f are not easily discernible; the isotherms are between a Type II (non-porous) and Type IV (meso-porous) while the hysteresis is between Type H1 and H2.

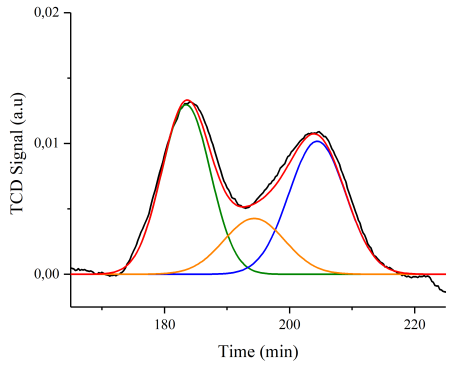

(a) ZSM5-117-500

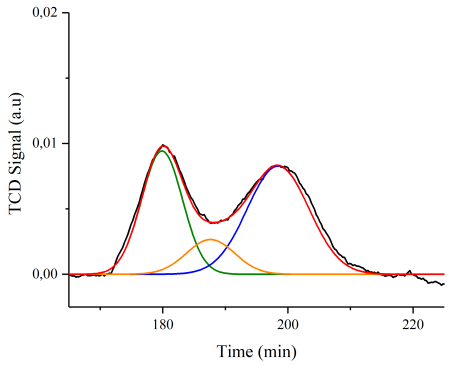

(b) ZSM5-117-500-st

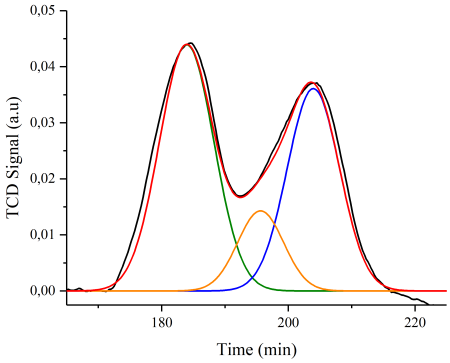

(c) ZSM5-38-500

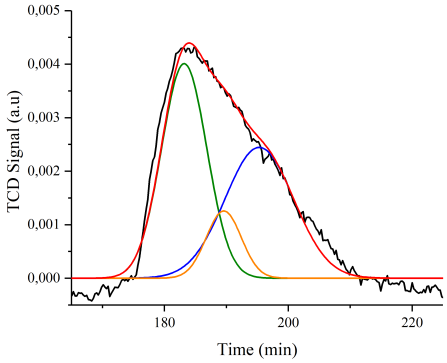

(d) ZSM5-38-500-st

Figure 4: Deconvoluted TPD peaks for powder samples.

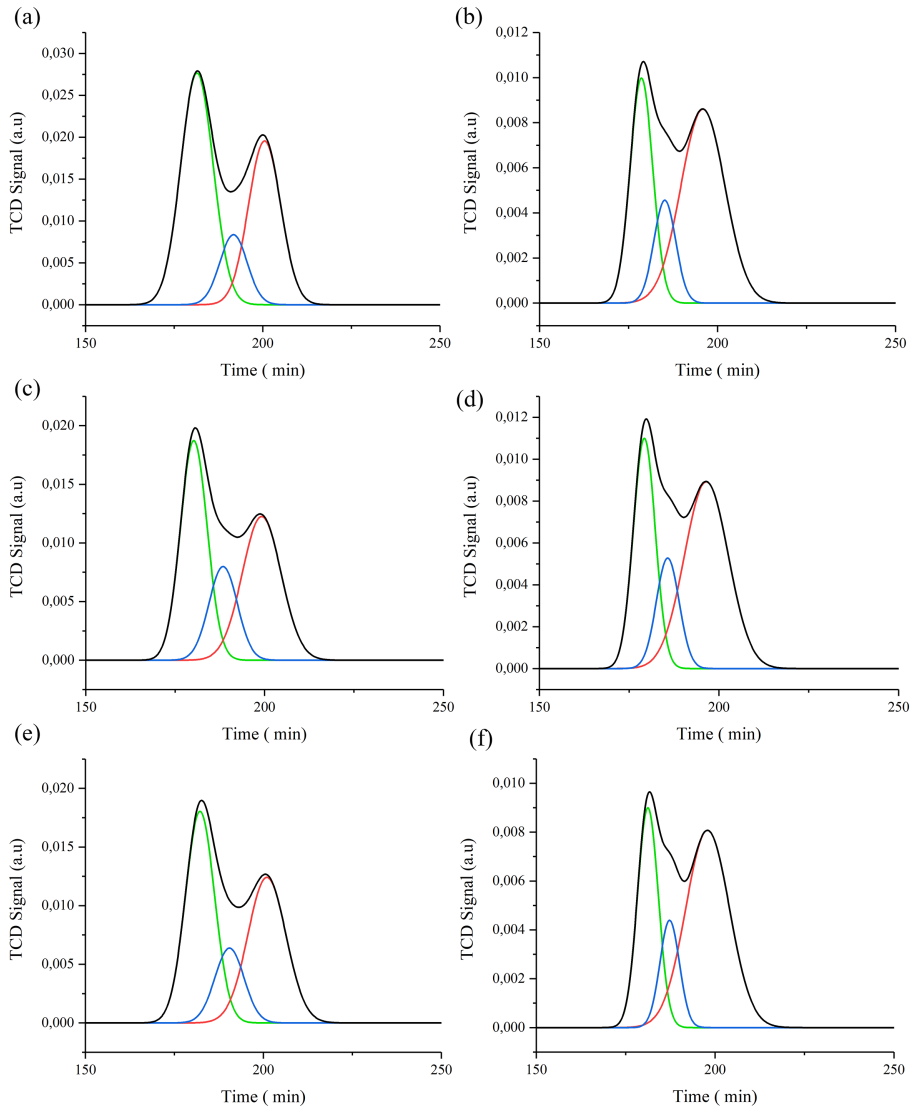

Figure 5: Deconvoluted TPD peaks for extrudate samples (a) CATD-parent, (b) CATD-steamed, (c) TM70-parent, (d) TM70-steamed, (e) TH100-parent and (f) TH100-steamed

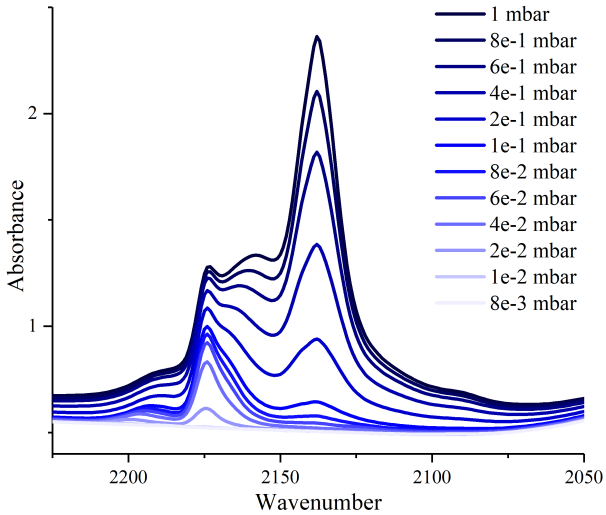

Figure 6: Change in CO adsorption over different pressures with the "flooding" technique.

Sample	BET Surface area (m^2/g)	Total pore volume (cm^3/g)	Micro-pore volume (cm^3/g)
117-500 parent	502.0 ± 0.4	0.19 ± 1%	0.16 ± 0.5%
117-500 steamed	481.7 ± 0.3	0.18 ± 1%	0.16 ± 0.4%
38-500 parent	380.3 ± 2.8	0.15 ± 1%	0.14 ± 0.2%
38-500 steamed	177.4 ± 5.0	0.17 ± 1%	0.06 ± 0.3%
CATD-parent	315.4 ± 0.4	0.39 ± 1%	0.07 ± 0.8%
CATD-steamed	251.4 ± 0.9	0.30 ± 1%	0.06 ± 0.8%
CATD-binder	182.3 ± 13.8	0.38 ± 1%	0.00 ± 0
TM70-parent	301.5 ± 0.3	0.30 ± 1%	0.07 ± 0.8%
TM70-steamed	256.4 ± 1.2	0.32 ± 1%	0.06 ± 0.8%
TM70-binder	164.4 ± 11.4	0.37 ± 1%	0.00 ± 0
TH100-parent	296.6 ± 0.2	0.22 ± 1%	0.08 ± 0.8%
TH100-steamed	243.6 ± 1.5	0.21 ± 1%	0.06 ± 0.8%
TH100-binder	154.8 ± 10.8	0.30 ± 1%	0.00 ± 0

Table 2: Physisorption data

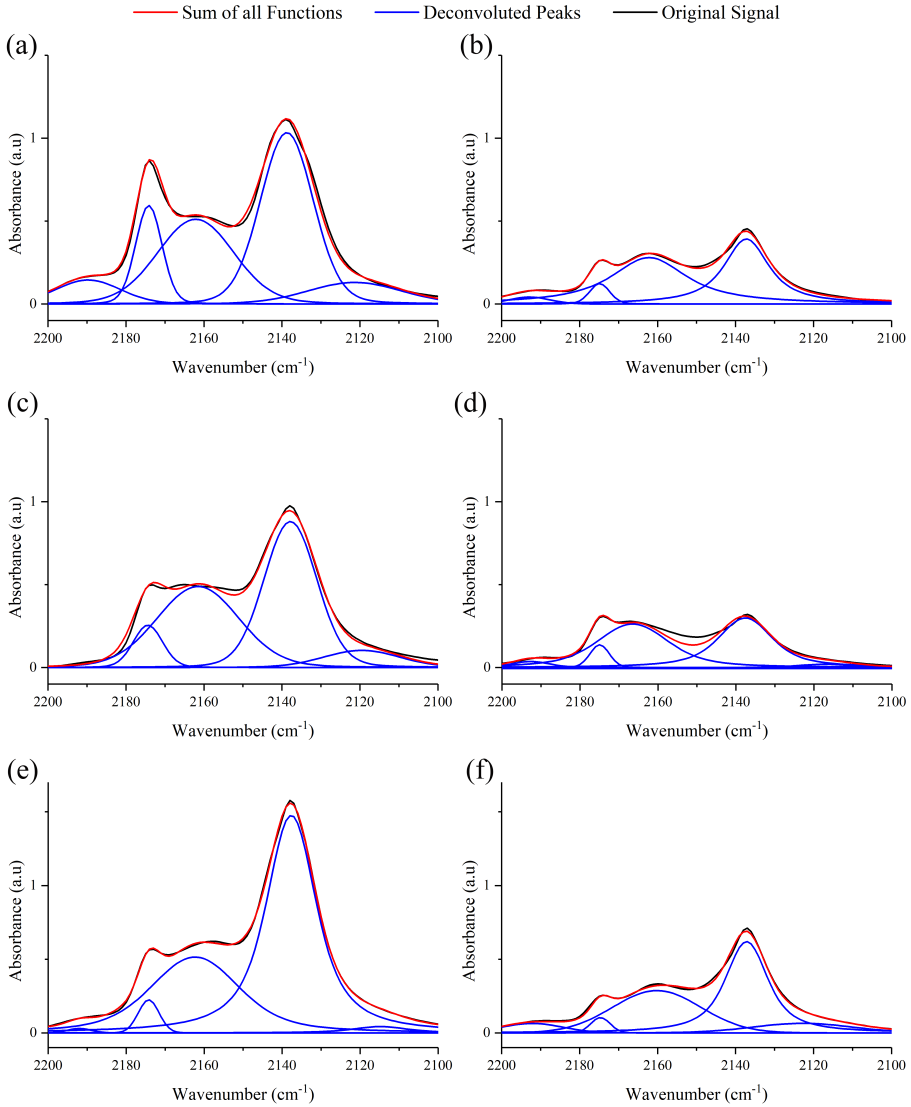

Figure 7: Deconvoluted CO IR spectra for (a) CATD-parent, (b) CATD-steamed, (c) TM70-parent, (d) TM70-steamed, (e) TH100-parent and (f) TH100-steamed

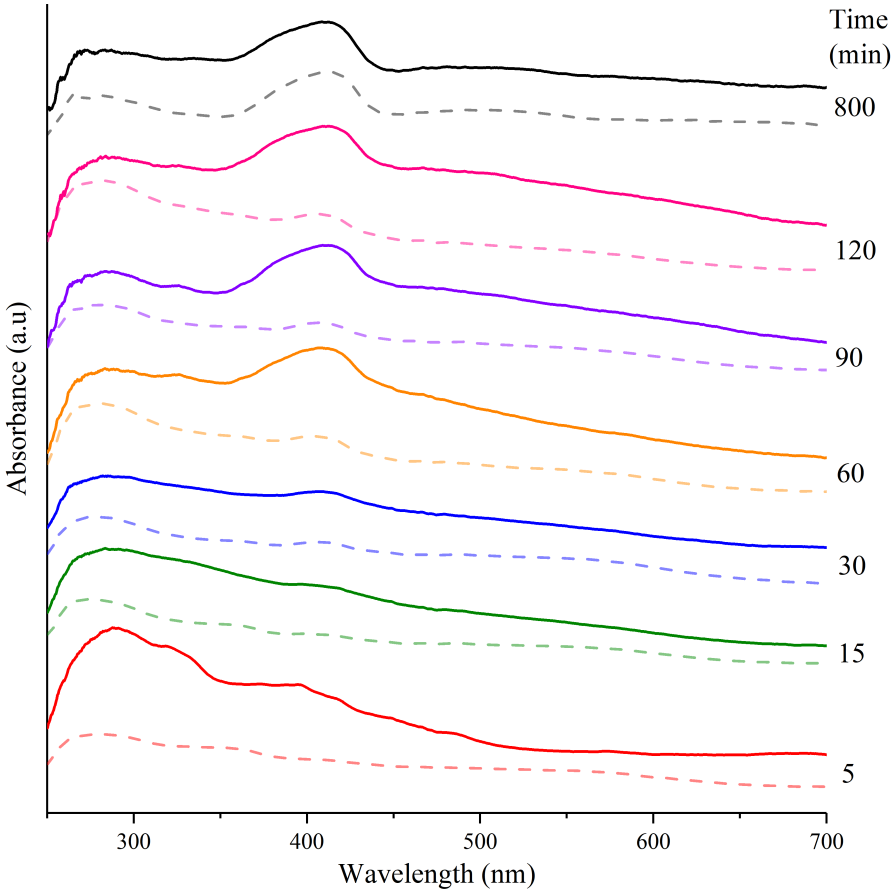

Figure 8: UV-Vis absorption spectra of spent CATD samples after being removed from the reactor at different times, bisectioned and imaged at the edge (solid line) and centre (dotted line) of the extrudate.

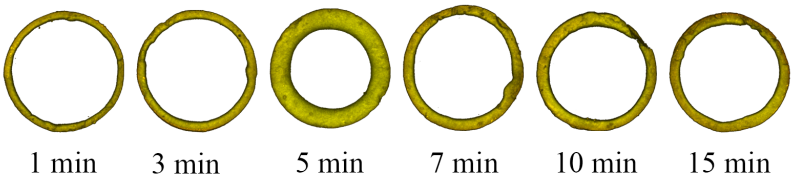

Figure 9: Visual representation of penetration depth for Porogen RS30 (Rice Starch 30wt%) using 5 nm probe. Incomplete combustion of the porogen is the most likely reason for the low penetration.

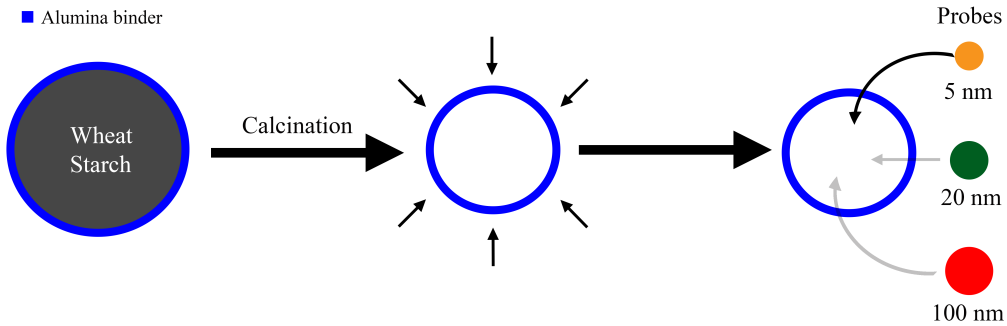

Figure 10: Scheme of the behaviour of the porogen. Alumina binder encases the porogen upon during the extrusion process, upon calcination the porogen is removed leaving behind an alumina shell, that then allows the penetration of the smaller 5 nm probe, but limits that of the 20 and 100 nm probes.

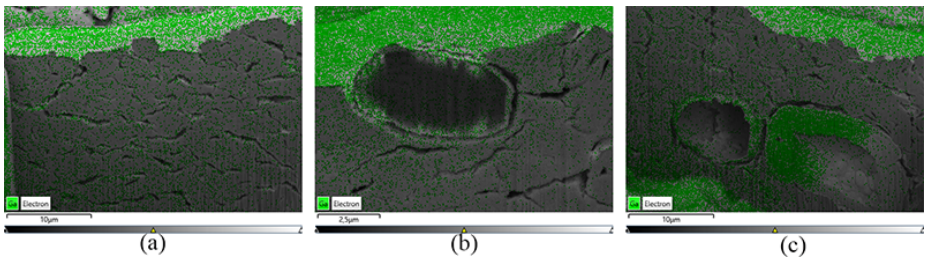

Figure 11: SEM-EDX measurements showing the distribution of Ga for (a) CATD calcined, (b) WS30 un-calcined and (c) WS30 calcined. A gallium ion beam was used in the milling/cleaning process and is present all throughout the samples, accounting for the blocking of certain pores in the calcined images.

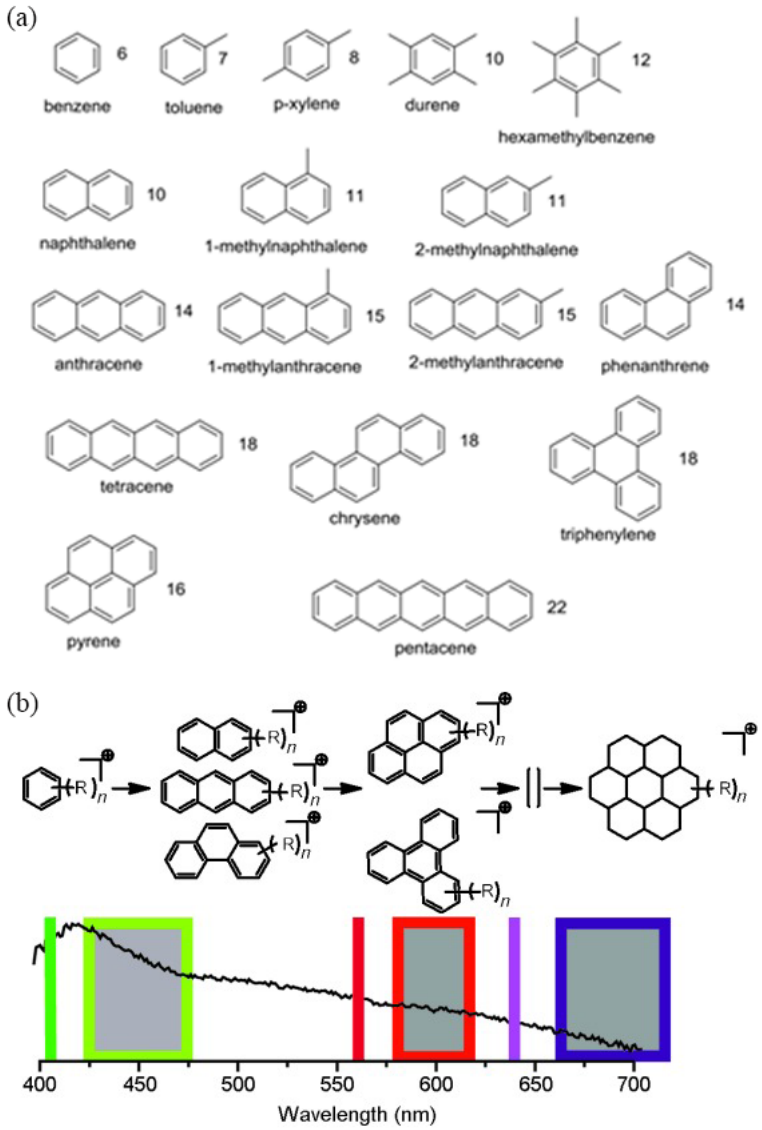

Figure 12: (a) Trapped coke species formed during MTO, with number of carbon atoms per molecule. Reproduced from Schmidt *et al.*[102] and (b) Coke formation taking place in MTO reactor as detected by laser wavelengths 405, 561 and 637 nm using CFM. Reproduced from Mores *et al.*[12]

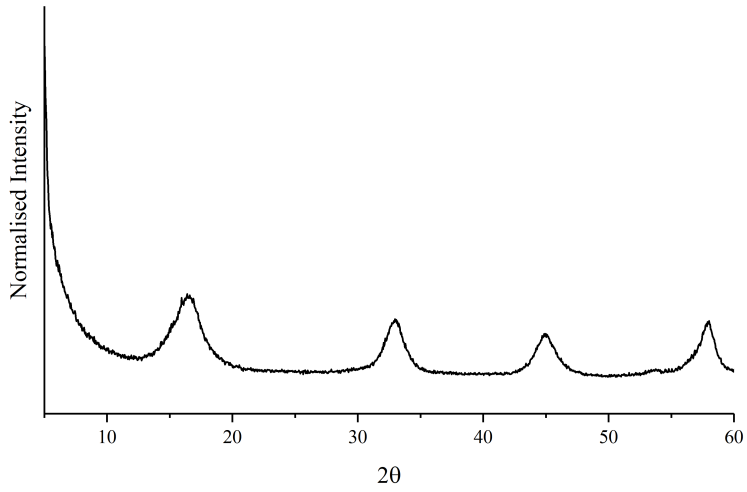

Figure 13: XRD pattern for CATAPAL D alumina binder showing the largely amorphous nature of the binder.

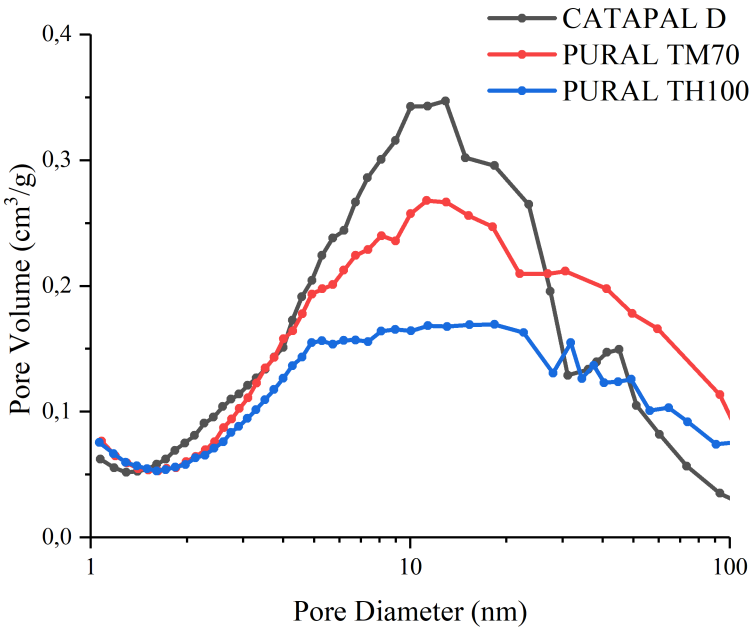

Figure 14: Pore size distributions using Ar physisorption of the different alumina binders. All binders show a high degree of meso-porosity, although due to the inability of physisorption to effectively probe the macro-pore scale, the results >50 nm are not entirely accurate.

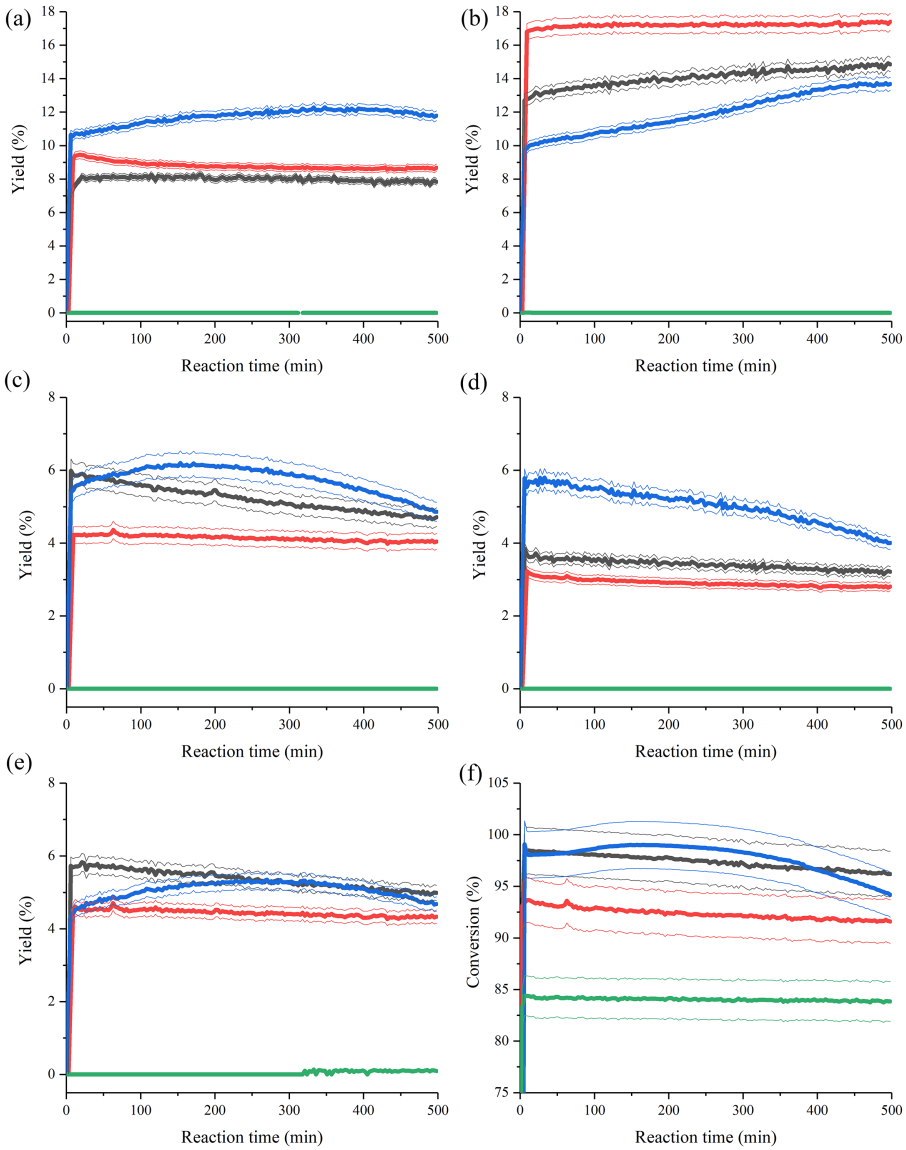

	Ethylene	Propylene	Iso-butylene	C5 paraffins	C5 olefins	Conversion
% error	2,5	2,9	5,4	4,3	4,2	2,3

Figure 15: Powder zeolite MTO graphs with error for (a) Ethylene, (b) Propylene, (c) Iso-butylene, (d) C_5 paraffins, (e) C_5 olefins and (f) Conversion. Error calculated from repeating a single measurement 4 times, deriving the standard deviation and converting to percentage error for all products.

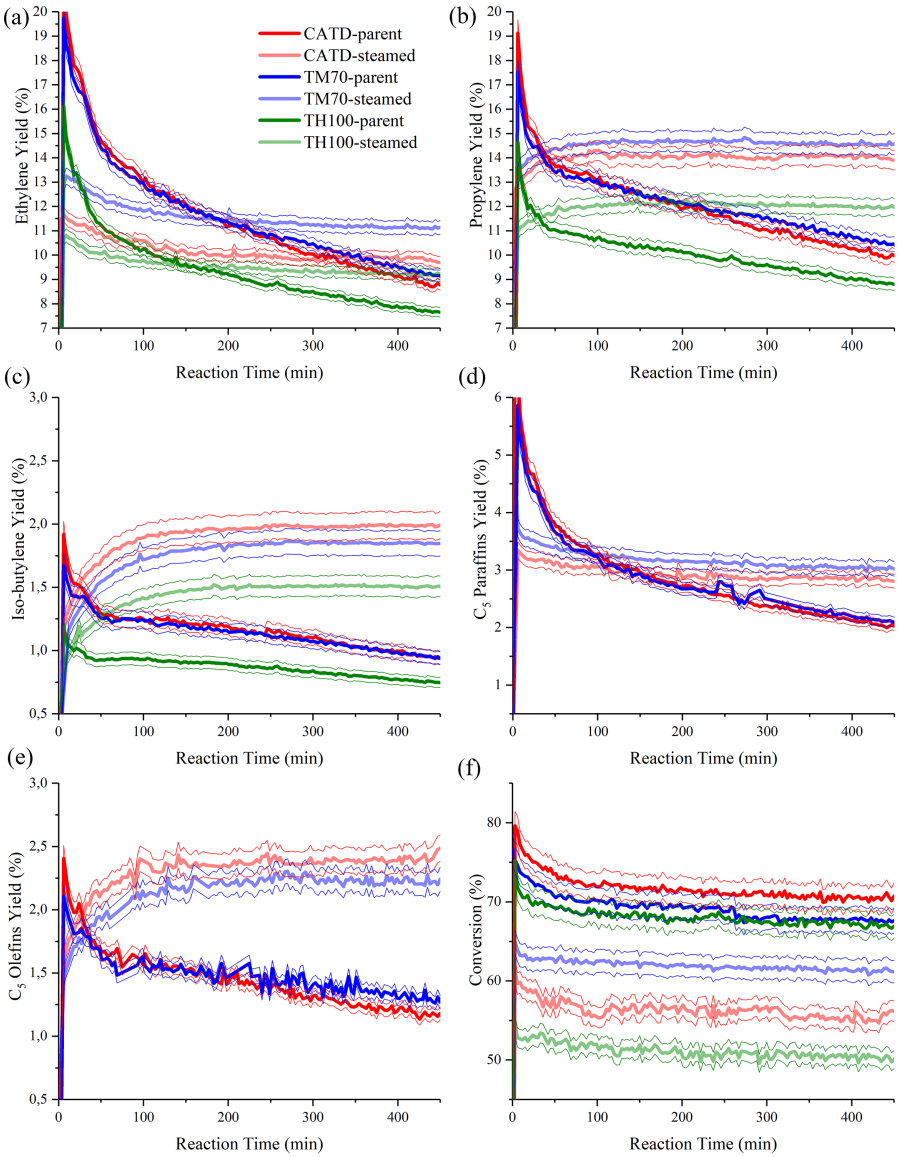

	Ethylene	Propylene	Iso-butylene	C5 paraffins	C5 olefins	Conversion
% error	2,5	2,9	5,4	4,3	4,2	2,3

Figure 16: Extrudate MTO graphs with error for (a) Ethylene, (b) Propylene, (c) Iso-butylene, (d) C_5 paraffins, (e) C_5 olefins and (f) Conversion. Error calculated from repeating a single measurement 4 times, deriving the standard deviation and converting to percentage error for all products.

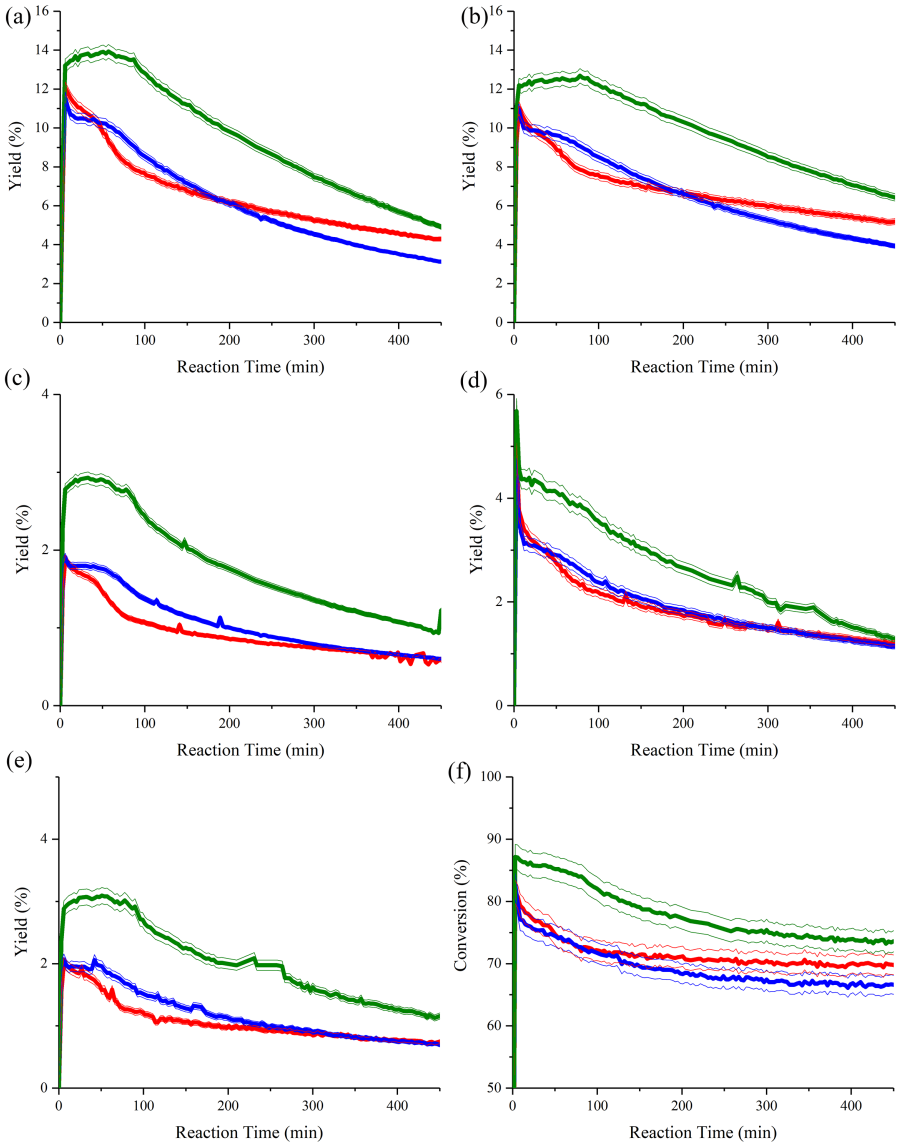

	Ethylene	Propylene	Iso-butylene	C5 paraffins	C5 olefins	Conversion
% error	2,5	2,9	5,4	4,3	4,2	2,3

Figure 17: Porogen MTO graphs with error for (a) Ethylene, (b) Propylene, (c) Iso-butylene, (d) C_5 paraffins, (e) C_5 olefins and (f) Conversion. Error calculated from repeating a single measurement 4 times, deriving the standard deviation and converting to percentage error for all products.